5 PERIODIC BOUNDARY CONDITIONS

5.1 Introductory remarks

Geometrically periodic configurations arise in many industrial applications and may thenceforward lead fluid flows to some repetitive behaviour. This periodic nature is the basis for several systems, including those operating under a cyclic way. For instance, periodic flows occur in heat exchangers, evaporators, condenser tubes and electronics cooling, at which either arrays of fins or plates are periodically arranged, thus creating sorts of patterns that influence the flow and other properties of the system.

PBC have been an appreciated tool by researchers in attempting to obtain computational efficiency when either fully-developed or periodic regimes are taken into account. Also, PBC are typically intended to isolate bulk phenomena, when one considers that the boundaries of the real physical system have minor effects. Flows of granular material [**?**], fluid-particle flows [**?**], molecular dynamics [**?**], heat and mass transfer problems [**?**], and the dynamics of gas-liquid flows in long oil pipelines [**?**] are some examples of fields where this strategy was used. Some of the references aforementioned use “simulation box”, “unit cell”, or “tiling” as referring to PBC simulations, since the overall flow dynamics is confined into a piece of the domain. Intuitively, the simplest way to idealize the periodicity is to set the same values of an arbitrary quantity on the extremities of the cell.

In regard to a topological point of view, a two-dimensional strip, for instance, can generate a cylinder just as a cylinder can generate a torus by “gluing" their extremities each other. Such topological relations as well as the “tiling” process are depicted in Figure 29 to single out the periodic passage of generic streamlines of a representative in-loop flow. Alike procedure to generate prismatic geometries is done by extrusion of elementary shapes, through which periodic boundaries are identified by geometrical relations, such as reflections or translations. When carrying these operations to the FE context presented here, a few requirements must be fulfilled to avoid degradations and discontinuity of the solution over the elements whose DOFs are under imposition of PBC. In this chapter, the whole strategy to apply PBC on the ALE/FEM context studied is presented in details from the mesh pre-processing stage. Comments on the mathematical formulation through FEM as well as the computational implementation come next.

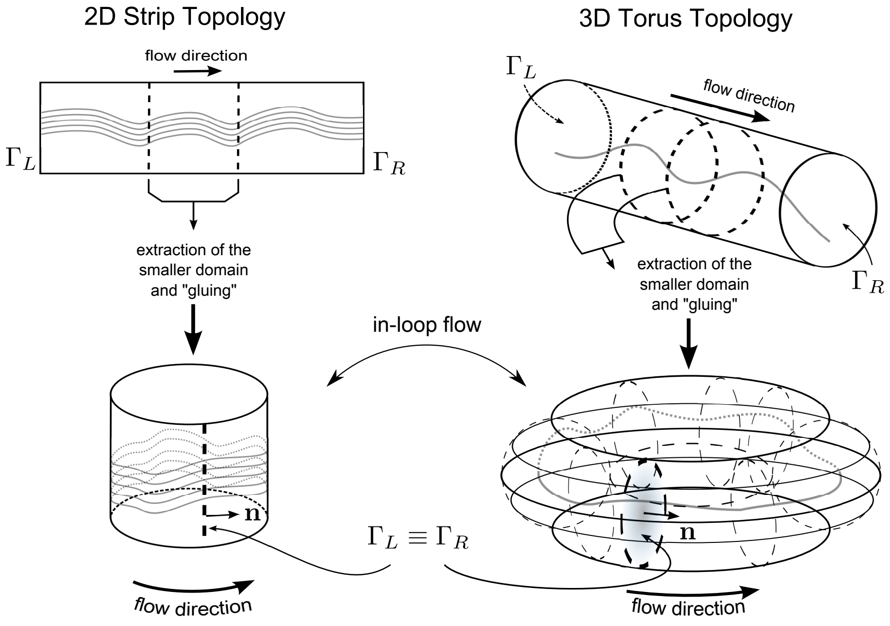

Figure 29: Sketch of the topological mappings, “tiling” process, and in-loop flow settings for generic geometries: 2D strip at left and 3D torus at right.

5.2 **Design of periodic meshes and their pre-processing**

It is assumed here that the PBC implementation depends on meshes that ensure a one-to-one spatial correspondence between each pair of nodes belonging to each periodic boundary chosen *a priori*. The strategy to build periodic meshes - thus termed because of their geometrical construction - is based on both topological and geometrical ideas as before mentioned. In this thesis, the surface mesh $\mathscr{T}_{h_\Gamma}^{\Gamma}$ is generated through user-defined scripts inserted into the GMSH software during the pre-processing stage. Sequentially, the volume mesh $\mathscr{T}_h^{\Omega}$ is created during the code runtime.

Following [**?**], we will refer to the DOFs of a periodic mesh as: *master*, *slave*, or *internal* according to their spatial location. It is worth to comment that in this context, DOFs and nodes are terminologies used almost interchangeably since the main ideas behind the periodic correspondence are of geometrical nature. The master DOFs will be those placed over the boundary chosen to be at the upstream side of the flow, whereas the slave ones will be their downstream counterparts. All the remnant DOFs, i.e. those that are out of the periodic boundaries will be, hence, internal, even if they belong to nonperiodic boundaries. At first, the master and slave nodes have different spatial coordinates over the mesh as regards the period length, but, practically, their independence is changed by an overloading process by which the slave DOFs render “dummy nodes”, thereby matching exactly the sites of the master

DOFs. This numerical artifice eliminates the slave DOFs fictitiously to favour the periodic simulation. Figure 30 (see a two-dimensional version in [**?**]) sketches the three-dimensional geometrical rudiments to establish the PBC in the FEM. For this specific example, let Γ_L, Γ_R be the master and slave periodic boundaries, respectively, and consider $\mathbf{x}_L = (x_L, y_L, z_L) \in \Gamma_L$, $\mathbf{x}_R = (x_R, y_R, z_R) \in \Gamma_R$ to be the master and slave nodes holding the DOFs of interest. For ι nodes of discretization, the sequences

$$(\mathbf{x}_L;\iota) := \{\mathbf{x}_{L,1}, \mathbf{x}_{L,2}, \ldots, \mathbf{x}_{L,\iota}\}$$
$$(\mathbf{x}_R;\iota) := \{\mathbf{x}_{R,1}, \mathbf{x}_{R,2}, \ldots, \mathbf{x}_{R,\iota}\}$$

define the geometrical periodicity of the mesh if

$$\mathbf{x}_R = \mathbf{x}_L + L_P \mathbf{e}_P \tag{5.1}$$

for each pair of nodes.

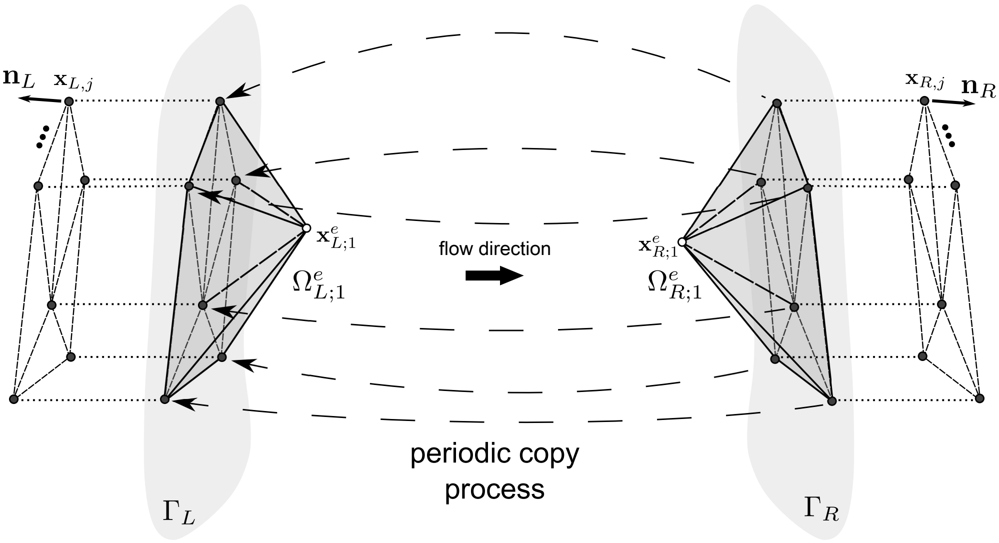

Figure 30: Geometrical sketch of the PBC implementation for a 3D periodic finite element mesh.

In consequence of the geometrical identification, we achieve conformity between the elements sharing the periodic boundaries. For a better view of this, let $\Omega^e_{L,1}$ and $\Omega^e_{R,1}$ be the 1-ring neighbours of Γ_L and Γ_R, respectively, where the definition of "k-rings" here is adapted from that used by [**?**] to establish the pairing between the two families of periodic elements. In this case, the entity shared with each periodic element is the boundary surface itself. In other words,

$$\Omega^e_{d,1} := \{\cup_{e=1}^{E}\Omega^e_d;\ F^e_d \cap \Gamma_d \neq \emptyset\}, \quad d = L, R. \tag{5.2}$$

Moreover, some elements can also share only nodes rather than an entire edge or face, thus allowing that some F^e_d is understood as a point only. In this manner, the DOFs that connect edges and faces over the boundaries are prepared to undergo the "gluing" operation by which the contributions of the slave DOFs are cumulative over the master nodes. That is to say, the boundary faces of the elements of $\Omega^e_{L,1}$ are connected (in a continuous sense) to the internal elements at right the equations relative to the nodes of Γ_R are disregarded in the matrices assembled via the standard FE process, which is discussed in the coming sections. In Figure 30, $\mathbf{x}_{L,j}, \mathbf{x}_{R,j}$ represent the master and slave nodes, respectively, that seal a periodic pair, whereas $\mathbf{x}^e_{L,j}, \mathbf{x}^e_{R,j}$ are two nodes underpinning the 1-ring element blocks depicted therein. Such nodes can be more informally recognized as "hooks" of the "umbrella" shape that is formed by these tetrahedra and are excluded from the computational periodicity. Even tough, they might be so geometrically since the meshes are always generated with volume restriction, thus enforcing, in this case, quasi-symmetric elements due to the quality tetrahedralization. The unstructured periodic meshes scripts take the built-in command `Periodic Surface` of the GMSH software into account to generate, thereafter, an automatized mechanism that transcribes the surface mesh placed over the master boundary onto the slave boundary. For a sample script about how to generate surface periodic meshes inside a two-phase context (this is the case of Figure 18), see Appendix C.

5.3 **Periodic decomposition via the transformed variable approach**

The imposition of PBC via the transformed variable approach used here follows the physical model introduced by [**?**] through which the variables of the flow are converted into a cyclic state. According to such a model, the main motivation to be conserved is that of dealing with fully developed flows without having to face computations involving effects of entrance region. Although the simulations presented in this thesis encompass mainly hydrodynamic effects, other physical effects, such as thermal, concentration and electromagnetic fields can be suitably treated through this approach if PBC were equally required (see Subsection 6.1.2).

Since this transformation decouples the flow of the entrance region, some kind of forcing term should be included in the model to compensate the fictitious in-loop domain enforced by the periodicity. As suggested by [**?**], velocity and pressure should be treated differently in the fully developed regime. While the velocity field obeys a relation of kind

$$\mathbf{v}|_{\Gamma_L} = \mathbf{v}|_{\Gamma_R} \tag{5.3}$$

at the extremities of the periodic cell, the pressure drop is periodic along the cell length, instead of the pressure field itself. For this reason, the approximation

$$\frac{\partial p}{\partial(\mathbf{x}\cdot\mathbf{e}_P)} \approx \frac{\Delta p}{L_P} = \frac{p|_{\Gamma_R} - p|_{\Gamma_L}}{L_P} = \beta \tag{5.4}$$

used for a fluid flowing along the direction $\mathbf{e}_P$ inside a cell of period L_P, describes the periodic pressure drop by means of a constant gradient. In this manner, β can be interpreted as a mass flow producer and taken to characterize a decomposition of the pressure field p of the momentum equation as

$$p = -\beta(\mathbf{x}\cdot\mathbf{e}_P) + \tilde{p}, \tag{5.5}$$

where $\tilde{p}$ is related to the local motions of the flow, so that holds

$$\tilde{p}|_{\Gamma_L} = \tilde{p}|_{\Gamma_R}. \tag{5.6}$$

As suggested by [**?**], [**?**], $\tilde{p}$ is said to be a *reduced pressure*. With this formulation, the prescription of a pressure gradient is expected, as opposed to a mass flow, or inflow condition. Despite of this interpretation valid for channel flows, for instance, the physical sense of β can take on other facets.

On the other hand, we should bear in mind that Equation (5.5) evokes the hypothesis on unidirectional fully-developed flow and might be the simplest way to settle a forcing term for the periodic problem given the linear pressure drop. Furthermore, β as above is a dimensional value. To be introduced in the dimensionless momentum equation, some suitable form should be found (cf. [**?**], [**?**]). Depending on the physical situation to be simulated, β may work as a body force acting on the fluid flow. This is the case, for instance, in a Poiseuille starting flow (cf. Sec. 4 of [**?**]). For now, by choosing reference quantities for the Equation (5.5), we will assume that one of its possible representative dimensionless forms is

$$\frac{p}{\rho_{ref}U_{ref}^2} = -\frac{\beta L_{ref}}{\rho_{ref}U_{ref}^2}\frac{(\mathbf{x}\cdot\mathbf{e}_P)}{L_{ref}} + \frac{\tilde{p}}{\rho_{ref}U_{ref}^2} \Rightarrow p^* = -\beta^*(\mathbf{x}^*\cdot\mathbf{e}_P^*) + \tilde{p}^*, \tag{5.7}$$

whose asterisk can be dropped out to have consistency with Equations (3.40) and (3.42). Therewith, the dimensionless pressure gradient term is given by

$$\beta^* = \frac{\beta L_{ref}}{\rho_{ref}U_{ref}^2} = \left(\frac{\beta}{\rho_{ref}U_{ref}^2}\right)L_{ref}. \tag{5.8}$$

Since the term inside parentheses is the Euler number, we will associate β^* with this dimensionless group by defining

$$\beta^* := Eu_{\beta^*}, \tag{5.9}$$

and calling Eu_{β^*} an Euler number associated to the pressure gradient.

After dropping out the asterisk and inserting Equation (5.7) into Equation (3.43a), the momentum equation takes on the form

$$\begin{aligned} \mathsf{B}_{1,P}(\mathbf{v},\tilde{p},\mathbf{f};\hat{\mathbf{v}},\rho,\mu,\mathbf{g}) &:= \rho\left(\frac{\partial\mathbf{v}}{\partial t} + (\mathbf{v}-\hat{\mathbf{v}})\cdot\nabla\mathbf{v}\right) - Eu_\beta\mathbf{e}_1 + \nabla\tilde{p} \\ -\frac{1}{Re}\nabla\cdot\left[\mu\left(\nabla\mathbf{v}+\nabla\mathbf{v}^T\right)\right] - \frac{1}{Fr^2}\rho\mathbf{g} - \frac{1}{We}\mathbf{f} &= \mathbf{0} \end{aligned} \tag{5.10}$$

being now $\tilde{p}$ the unknown to be determined.

The periodic boundary conditions resulting therefrom are

$$\mathbf{v}|_{\Gamma_L} = \mathbf{v}|_{\Gamma_R} \tag{5.11}$$

$$\mathbf{n}_L\cdot\nabla\mathbf{v}|_{\Gamma_L} = -\mathbf{n}_R\cdot\nabla\mathbf{v}|_{\Gamma_R} \tag{5.12}$$

$$\tilde{p}|_{\Gamma_L} = \tilde{p}|_{\Gamma_R} \tag{5.13}$$

$$\mathbf{n}_L\cdot\nabla\tilde{p}|_{\Gamma_L} = -\mathbf{n}_R\cdot\nabla\tilde{p}|_{\Gamma_R}. \tag{5.14}$$

These relations express the need for continuity over the periodic boundaries and assure that the primitive variables are identical both in the inlet and outlet, thus closing the connection loop, i.e. the fluid should leave the domain just as it comes in. In the FEM context, the Neumann conditions play a relevant role during the assembling process of the elemental matrices modified for PBC which is explained in the next section. Comini *et al.* [**?**] underlined that the normal derivative can be prescribed as zero or nonzero, depending if orthogonal or skew incoming flow is desired, but the second case is not examined here.

5.4 **FE/PBC implementation**

Different methodologies are available to impose PBC through a FE approach both in periodic and non-periodic meshes [**?**], [**?**], [**?**], [**?**], [**?**], [**?**]. Generally, they encompass the enforcement of nodal connectivity through auxiliary lists during the assembling process of the FE global system matrices as well as operations to suppress or sum rows and columns in the global matrices. In this thesis, we have opted by the second strategy, which will be detailed through the next sections.

5.4.1 Variational formulation in periodic domains

Analogous ideas to those presented in Section 4.3 are reused here to set forth a periodic variational formulation for the governing equations. We start by putting together the forms defined in Equations (5.10), (3.43b) and (3.43c) in the system

$$\begin{cases} \mathsf{B}_{1,P}(\mathbf{v}, \tilde{p}, \mathbf{f}; \hat{\mathbf{v}}, \rho, \mu, \mathbf{g}) = 0 \\ \mathsf{B}_2(\mathbf{v}) = 0 \\ \mathsf{B}_3(\Psi) = 0. \end{cases} \tag{5.15}$$

Next, define the following weight function spaces:

$$\mathscr{V}_P := \{\mathbf{w} \in \mathscr{H}^1_P(\Omega);\ \nabla \cdot \mathbf{v} = 0, \mathbf{v}(\mathbf{x}) = \mathbf{v}(\mathbf{x} + L_P \mathbf{e}_P), \mathbf{x} \in \Gamma_L\}$$

$$\mathscr{Q}_P := \{q \in \mathscr{L}^2_P(\Omega);\ q(\mathbf{x}) = q(\mathbf{x} + L_P \mathbf{e}_P), \mathbf{x} \in \Gamma_L\}$$

$$\mathscr{R}_P := \{r \in \mathscr{L}^2_P(\Omega);\ r(\mathbf{x}) = r(\mathbf{x} + L_P \mathbf{e}_P), \mathbf{x} \in \Gamma_L\}.$$

These spaces gather periodic functions used to comply with a variationally consistent formulation of FE with PBC (cf. [**?**], [**?**]). Thenceforward, except for the addition of periodic weight functions $(\mathbf{v}_P, q_P, r_P) \in (\mathscr{V}_P, \mathscr{Q}_P, \mathscr{R}_P)$ in the weak form equations (cf. Equations (4.29), (4.8a) and (4.8b), the system Equation (5.15) is identical to the original forms. Therefore,

$$\begin{cases} \mathsf{B}_{1,P}(\mathbf{v}_P, \tilde{p}, \mathbf{f}; \hat{\mathbf{v}}, \rho, \mu, \mathbf{g}) = 0 \\ \mathsf{B}_{2,P}(\mathbf{v}_P) = 0 \\ \mathsf{B}_{3,P}(\Psi_P) = 0 \end{cases} \tag{5.16}$$

is the homologous periodic version of Equation (5.15) in the sense of Galerkin. The mesh velocity field $\hat{\mathbf{v}}$ is not considered periodic since the methodology employed here prevents the motion of $\mathscr{T}^{\Gamma^2}$. Consequently, nodes lying on the periodic boundaries are stationary concerning the field $\hat{\mathbf{v}}$.

That said, when assigning bilinear forms similar to the standard formulation, the terms expanded from the weighting of Equation (5.16)

$$\begin{cases} \int_\Omega \mathsf{B}_{1,P}(\mathbf{v}_P, \tilde{p}, \mathbf{f}; \hat{\mathbf{v}}, \rho, \mu, \mathbf{g}) \cdot \mathbf{w}_P \, d\Omega = 0 \\ \int_\Omega \mathsf{B}_{2,P}(\mathbf{v}_P) \cdot q_P \, d\Omega = 0 \\ \int_\Omega \mathsf{B}_{3,P}(\Psi_P) \cdot r_P \, d\Omega = 0 \end{cases} \tag{5.17}$$

give rise to the respective discrete equations for the quantities involved:

$$m_{\rho,P}(\rho; \mathbf{v}_{h,P}^{n+1}, \mathbf{w}_{h,P}) + \frac{\Delta t}{Re^{1/2}} k_P(\mu; \nabla \mathbf{v}_{h,P}^{n+1}, \nabla \mathbf{w}_h) + \\ + \Delta t g_P(\tilde{p}_h^{n+1}, \nabla \cdot \mathbf{w}_{h,P}) = \Delta t \mathbf{r}_{h,P}^n \tag{5.18a}$$

$$d_P(\mathbf{v}_{h,P}^{n+1}, \nabla \cdot q_{h,P}) = 0 \tag{5.18b}$$

with $\mathbf{r}_{h,P}^n = m_{\rho,P}(\rho; \mathbf{v}_{h,d,P}^n, \mathbf{w}_{h,P}) + m_{\rho,P}(\rho; \mathbf{g}_h^n, \mathbf{w}_{h,P}) +$
$+ \lambda E u_\beta m_P(\varphi_{h,P}^n \mathbf{e}_P, \mathbf{w}_{h,P}) + \frac{1}{We}(\mathbf{f}_{\sigma}{}_h^n, \mathbf{w}_{h,P})$

with $\psi_{h,P}^n \mathbf{e}_P, \mathbf{v}_h, \mathbf{w}_h \in \mathscr{V}_P^h \subset \mathscr{V}_P$ and $\tilde{p}_h, q_{h,P} \in \mathscr{Q}_P^h \subset \mathscr{Q}_P$ for the momentum; and

$$m_{\Psi,P}\left(\Psi_{h,P}^{n+1}, r_{h,P}\right) + \frac{\Delta t}{ReSc} k_{\Psi,P}(\varrho; \nabla \Psi_{h,P}^{n+1}, \nabla r_{h,P}) = \Delta t m_{\Psi,P}(\Psi_{h,d,P}^n, r_{h,P}). \tag{5.19}$$

with $\Psi_{h,P}, r_{h,P}, \in \mathscr{R}_P^h \subset \mathscr{R}_P$ for the scalar field.

All the bilinear forms P-subscripted above can be compared to their counterparts, viz. Equations (4.31), (4.16a) and (4.16b). Different than the others, the term $\lambda E u_\beta m_P(\varphi_{h,P}^n \mathbf{e}_P, \mathbf{w}_{h,P})$ have null contributions in the coordinates transverse to the streamwise periodic flow. In other words, $\varphi_{h,P}^n \mathbf{e}_P$ are the shape functions relative to the periodic direction $\mathbf{e}_P$ chosen that determines

$$(\varphi^n_{h,P}\mathbf{e}_P, \mathbf{w}_{h,P}) = \delta_{iP}(\varphi^n_{h,P}\mathbf{e}_P, \mathbf{w}_{h,P}), \quad 1 \leq i, P \leq 3, \tag{5.20}$$

for the Kronecker's delta δ_{iP}, i.e. the pressure gradient λEu_β acts only when $i = P$.

In turn, Equations (5.19), (5.18a) and (5.18b) generate the following set of matrix equations:

$$\begin{aligned} \mathbf{M}_{\rho,P}\mathbf{v}_P^{n+1} + \frac{\Delta t}{Re}\mathbf{K}_P\mathbf{v}_P^{n+1} & \\ +\Delta t\mathbf{G}_P\tilde{\mathbf{p}}^{n+1} &= \Delta t\left[\mathbf{M}_{\rho,P}\mathbf{v}^n_{d,P} + \mathbf{M}_P\mathbf{b}^n + \frac{1}{Fr^2}\mathbf{M}_{\rho,P}\mathbf{g}^n + \frac{1}{We}\mathbf{M}_P\mathbf{f}^n\right] \end{aligned} \tag{5.21a}$$

$$\mathbf{D}_P\mathbf{v}_P^{n+1} = \mathbf{0} \tag{5.21b}$$

$$\mathbf{M}_{\Psi,P}\mathbf{\Psi}_P^{n+1} + \frac{\Delta t}{ReSc}\mathbf{K}_{\Psi,P}\mathbf{\Psi}_P^{n+1} = \Delta t\mathbf{M}_{\Psi,P}\mathbf{\Psi}^n_{d,P}, \tag{5.21c}$$

with $\mathbf{b}^n = \lambda Eu_\beta\mathbf{e}_P$.

Following by analogy to Equation (4.35), eqs. (5.21a - 5.21c) can be written as

$$\begin{cases} \mathbf{B}_P\mathbf{v}_P^{n+1} + \Delta t\mathbf{G}_P\tilde{\mathbf{p}}^{n+1} = \mathbf{b}_{1,P} \\ \mathbf{D}_P\mathbf{v}_P^{n+1} = \mathbf{b}_{2,P} \\ \mathbf{B}_{\Psi,P}\mathbf{\Psi}_P^{n+1} = \mathbf{b}_{3,P}, \end{cases} \tag{5.22}$$

for each r.h.s. vector given by $\mathbf{b}_{i,P}$, $i = 1, 2, 3$.

Although it is possible to develop a formal essay of the periodic variational formulation – as expressed by Equation (5.22) –, the PBC can be enforced in a more pragmatic manner by spanning directly the nonperiodic operators in the matrices already assembled during the original formulation. The incorporation of the DOFs belonging to the periodic nodes is reached through a pseudounion of the shape functions of the 1-ring neighbour elements of Γ_L, Γ_R, which is given by changing the interelement connections in the global matrices. Explanation in details about this procedure is given in [**?**].

5.4.2 Computational implementation

Approaches to implement PBC may fall into a strategy of full reordering of the matrix system by reassembling process. On the other hand, this step may also involve laborious modifications in a large computational code, since all the matrices and vectors would have to be rearranged. Instead performing reassembling operations, it is advisable to pave the entire PBC problem yet during the assembling stage. Segal *et al.* [**?**] suggest that the global system is previously mounted under PBC restrictions. Nonino and Comini [**?**] also have worked with similar strategies. This track ends on a system like Equation (5.22). Alternatively, to circumvent this painstaking task of reassembling, we have chosen to take a shortcut to eliminate the DOFs corresponding to the slave periodic boundary. The proposed algorithm runs through the original matrix system by localizing the indices of the connection elements and modifies the elementary submatrices directly, thus avoiding additional memory allocation. A slightly different strategy based on the manipulation of lists is explained, for instance, in [**?**].

During the elimination process, consider (i,j) an arbitrary pair of indices identifying the nodes over the periodic boundaries Γ_L and Γ_R, respectively; ibL a particular index for each node over Γ_L and ibR a particular index for each node over Γ_R. Let us consider, for $m = 0,1,2$,

$$\mathscr{A}(i,j;m)[\cdot] = \begin{array}{cc} \begin{array}{ccccccccc} & ibL & & ibR & & ibL_N & & ibR_N & \end{array} & \\ \begin{bmatrix} \ddots & | & \vdots & | & \vdots & | & \vdots & | & \vdots \\ — & b_{(i+mv,i+mv)} & — & 0 & — & \star & — & 0 & — \\ \vdots & | & \ddots & | & \vdots & | & \vdots & | & \vdots \\ — & 0 & — & b_{(j+mv,j+mv)} & — & 0 & — & \bullet & — \\ \vdots & | & \vdots & | & \ddots & | & \vdots & | & \vdots \\ — & \star & — & 0 & — & \triangle & — & 0 & — \\ \vdots & | & \vdots & | & \vdots & | & \ddots & | & \vdots \\ — & 0 & — & \bullet & — & 0 & — & \diamond & — \\ \vdots & | & \vdots & | & \vdots & | & \vdots & | & \ddots \end{bmatrix} & \begin{array}{c} \\ ibL \\ \\ ibR \\ \\ ibL_N \\ \\ ibR_N \\ \\ \end{array} \end{array} \tag{5.23}$$

a symmetric submatrix-model for the original formulation containing the Neumann interelement contributions according to the FE discretization for the pair (ibL, ibR). Above,

ibL_N, ibR_N mark rows (columns) relative to an arbitrary node which is connected to the periodic pair and the symbols at the crossed entries represent nonzero contributions. Hence, this matrix is a substratum of what each global matrix contains on the rows (columns) for the respective dimension. That is, if $m = 0$, the matrix is relative to a one-dimensional discretization; if $m = 1$, two blocks like the one above should be modified; if $m = 2$, the discretization is three-dimensional.

For each pair (i, j), with $i = ibL, ibR,\ \ j = ibL, ibR;\ \ i, j = 1, \ldots, \iota$, found after algorithmic search, $\mathscr{A}[\cdot]$ will be modified directly inside the matrices $\mathbf{B}$, $\mathbf{D}$, $\mathbf{G}$, $\tilde{\mathbf{E}}$ from eqs. (4.25 - 4.27), and $\mathbf{B}_\Psi$ from Equation (4.33) respecting their dimensions to obtain the periodic counterparts $\mathbf{B}_P$, $\mathbf{D}_P$, $\mathbf{G}_P$, $\tilde{\mathbf{E}}_P$, and $\mathbf{B}_{\Psi,P}$. Note that $\tilde{\mathbf{E}}_P$ results of the LU-factorization for the periodic problem by analogy. Besides, since $\mathbf{D}$ and $\mathbf{G}$ are nonsquare matrices, $\mathscr{A}[\cdot]$ must be adapted to be dimensionally consistent. For three-dimensional problems, it turns out that

$$\dim(\mathbf{B}) = \dim(\mathbf{B}_P) = 3\iota_v \times 3\iota_v \tag{5.24a}$$

$$\dim(\mathbf{D}) = \dim(\mathbf{D}_P) = \iota_s \times 3\iota_v \tag{5.24b}$$

$$\dim(\mathbf{G}) = \dim(\mathbf{G}_P) = 3\iota_v \times \iota_s \tag{5.24c}$$

$$\dim(\tilde{\mathbf{E}}) = \dim(\tilde{\mathbf{E}}_P) = \iota_s \times \iota_s \tag{5.24d}$$

$$\dim(\mathbf{B}_\Psi) = \dim(\mathbf{B}_{\Psi,P}) = \iota_s \times \iota_s, \tag{5.24e}$$

so that $v = \iota_v$ controls the number of DOFs of the velocity field by component, while $v = \iota_s$ controls the number of DOFs of the pressure and scalar fields.

Thenceforth, the original matrices acquire their periodic version by

i) summing the row of $\mathscr{A}[\cdot]$ relative to the periodic node ibL to the respective row relative to the periodic node ibR,

ii) summing the column of $\mathscr{A}[\cdot]$ relative to the periodic node ibL to the respective column relative to the periodic node ibR,

iii) zeroing the row ibL,

iv) zeroing the column ibR and, finally

v) adding “1” at the diagonal entries (ibL, ibL) to avoid indetermination.

This process results in

$$\mathscr{A}_P(i,j;m)[\cdot] = \begin{array}{cc} \begin{array}{ccccccccc} & ibL & & ibR & & ibL_N & & ibR_N & \end{array} & \\ \left[\begin{array}{ccccccccc} \ddots & \vert & \vdots & \vert & \vdots & \vert & \vdots & \vert & \vdots \\ \text{—} & 1 & \text{—} & 0 & \text{—} & 0 & \text{—} & 0 & \text{—} \\ \vdots & \vert & \ddots & \vert & \vdots & \vert & \vdots & \vert & \vdots \\ \text{—} & 0 & \text{—} & \Sigma_P(i,j;m) & \text{—} & \star & \text{—} & \bullet & \text{—} \\ \vdots & \vert & \vdots & \vert & \ddots & \vert & \vdots & \vert & \vdots \\ \text{—} & 0 & \text{—} & \star & \text{—} & \triangle & \text{—} & 0 & \text{—} \\ \vdots & \vert & \vdots & \vert & \vdots & \vert & \ddots & \vert & \vdots \\ \text{—} & 0 & \text{—} & \bullet & \text{—} & 0 & \text{—} & \diamond & \text{—} \\ \vdots & \vert & \vdots & \vert & \vdots & \vert & \vdots & \vert & \ddots \end{array}\right] & \begin{array}{c} \\ ibL \\ \\ ibR \\ \\ ibL_N \\ \\ ibR_N \\ \\ \end{array} \end{array} \tag{5.25}$$

with

$$\Sigma_P(i,j;m) = b_{(i+mv,i+mv)} + b_{(j+mv,j+mv)}, \quad i,j = ibL, ibR; \;\; m = 0,1,2. \tag{5.26}$$

Accordingly, let

$$\mathscr{U}(i,j;m)[\cdot] = \left[\begin{array}{c} \vdots \\ c_{(i+mv)} \\ \vert \\ c_{(j+mv)} \\ \vdots \\ \square \\ \vert \\ * \\ \vdots \end{array}\right] \begin{array}{c} \\ ibL \\ \\ ibR \\ \\ ibL_N \\ \\ ibR_N \\ \\ \end{array} \qquad m = 0,1,2, \tag{5.27}$$

be a model for the elementary vectors of contribution. $\mathscr{U}[\cdot]$ will be modified directly inside the vectors $\tilde{\mathbf{b}}_1$, $\tilde{\mathbf{b}}_2$ from Equations (4.25) and (4.26), and $\mathbf{b}_\Psi = \mathbf{r}^n_\Psi + \mathbf{bc}_\Psi$ from Equation (4.33) respecting their dimensions to obtain the periodic counterparts $\mathbf{b}_{1,P}$, $\mathbf{b}_{2,P}$, and $\mathbf{b}_{3,P}$ as referred in Equation (5.22) resulting in

$$\mathcal{U}(i,j;m)[\cdot] = \left[\begin{array}{c} \vdots \\ 0 \\ | \\ \Sigma_P(i,j;m) \\ \vdots \\ \square \\ | \\ * \\ \vdots \end{array}\right]\begin{array}{l} \\ ibL \\ \\ ibR \\ \\ ibL_N \\ \\ ibR_N \\ \\ \end{array} \qquad m = 0,1,2, \tag{5.28}$$

with, this time,

$$\Sigma_P(i,j;m) = c_{(i+mv)} + c_{(j+mv)}, \quad i,j = ibL, ibR; \;\; m = 0,1,2, \tag{5.29}$$

and the zeroed component ibL as opposed to the model-matrix $\mathcal{U}[\cdot]$.

The general algorithm of elimination of DOFs for the matrices and vectors of Equation (4.36) according to the previous models reads, for each time step t, as:

```
for $t : (0, T]$ do
    for $i : [1, \iota]$ do
        for $m : \{0, 1, 2\}$ do
            $ibL = \mathbf{i}_L(i)$ ;                    /* $\mathbf{i}_L$:  vector of indices ibL */
            $ibR = \mathbf{i}_R(i)$ ;                    /* $\mathbf{i}_R$:  vector of indices ibR */
            $\mathscr{A}^t(ibL, \cdot) \leftarrow \mathscr{A}^t(ibL, \cdot) + \mathscr{A}^t(ibR, \cdot)$ ;           /* summing rows */
            $\mathscr{A}^t(\cdot, ibL) \leftarrow \mathscr{A}^t(\cdot, ibL) + \mathscr{A}^t(\cdot, ibR)$ ;        /* summing columns */
            $\mathscr{A}^t(ibR, \cdot) = 0$ ;                          /* zeroing row ibR */
            $\mathscr{A}^t(\cdot, ibR) = 0$ ;                       /* zeroing column ibR */
            if $\mathscr{A}[\cdot] \doteq \mathbf{B}, \tilde{\mathbf{E}}, \mathbf{B}_\Psi$ then
                $\mathscr{A}^t(ibL + mv, ibL + mv) = 1$ ;         /* filling diagonals */
            end
            if $\mathscr{U}[\cdot] \doteq \tilde{\mathbf{b}}_1, \tilde{\mathbf{b}}_2, \mathbf{b}_\Psi, (\mathbf{v}, \tilde{\mathbf{p}}, \boldsymbol{\Psi})$ then
                $\mathscr{U}^t(ibR + mv) = \mathscr{U}^t(ibL + mv)$ ;  /* imposing periodicity */
            end
            $t \leftarrow t + \Delta t$
        end
    end
end
```

Observe, however, that $(\mathbf{v}, \tilde{\mathbf{p}}, \boldsymbol{\Psi})$ must turn into $(\mathbf{v}_P, \tilde{\mathbf{p}}, \boldsymbol{\Psi}_P)$ each time step to update the periodic solution of Equation (5.22). This is achieved applying the copying process provided by $\mathscr{U}$ over these vectors. Besides, for three-dimensional problems, it turns out that

$$\dim(\tilde{\mathbf{b}}_1) = \dim(\mathbf{b}_{1,P}) = 3\iota_v \times 1 \tag{5.30a}$$

$$\dim(\tilde{\mathbf{b}}_2) = \dim(\mathbf{b}_{2,P}) = \iota_s \times 1 \tag{5.30b}$$

$$\mathbf{b}_\Psi = \dim(\mathbf{b}_{3,P}) = \iota_s \times 1 \tag{5.30c}$$

$$\dim(\mathbf{v}) = \dim(\mathbf{v}_P) = 3\iota_v \times 1 \tag{5.30d}$$

$$\dim(\mathbf{p}) = \dim(\tilde{\mathbf{p}}) = \iota_s \times 1 \tag{5.30e}$$

$$\dim(\boldsymbol{\Psi}) = \dim(\boldsymbol{\Psi}_P) = \iota_s \times 1 \tag{5.30f}$$

$$\tag{5.30g}$$

so that, as aforementioned, $v = \iota_v$ controls the number of DOFs of the velocity field by component, while $v = \iota_s$ controls the number of DOFs of the pressure, periodic pressure and scalar fields.

The overloaded equations due to the periodic modification can be better viewed if we write the symbolic equation of the arguments $(\mathbf{B}_P, \mathbf{v}_P, \mathbf{b}_{1,P})$

$$\mathscr{A}_P(ibL, ibR; 0)\,[\mathbf{B}_P]\,\mathscr{U}_P(ibL, ibR; 0)\,[\mathbf{v}_P] = \mathscr{U}_P(ibL, ibR; 0)\,[\mathbf{b}_{1,P}], \tag{5.31}$$

the equations for the periodic pair (ibL, ibR) relative to the $x-$component of the velocity field can be extracted:

$$ibL\colon\ [1] \times [0] = [0] \tag{5.32}$$

$$ibR\colon\ [\mathbf{B}_{(ibL,ibL);P,x} + \mathbf{B}_{(ibR,ibR);P,x}] \times [\mathbf{v}_{ibL;P,x} + \mathbf{v}_{ibR;P,x}] + [\star_x] \times [\Box_x] + [\bullet_x] \times [*_x] \tag{5.33}$$

$$\tag{5.34}$$

showing, *de facto*, the gist of the elimination process. The first equation is left out from the computational effort; the second equation, hence, is overloaded, being interpreted as the sum of two parcels: *overload* + *extra contribution*. Furthermore, in terms of matrices, the previous arguments are embedded into a much bigger system formed by the parts

$$\mathbf{B}_P = \begin{bmatrix} \mathbf{B}_{P,x} & & \\ & \mathbf{B}_{P,y} & \\ & & \mathbf{B}_{P,z} \end{bmatrix}; \quad \mathbf{v}_P = \begin{bmatrix} \mathbf{v}_{P,x} \\ \mathbf{v}_{P,y} \\ \mathbf{v}_{P,z} \end{bmatrix}; \quad \mathbf{b}_{1,P} = \begin{bmatrix} \mathbf{b}_{1,P,x} \\ \mathbf{b}_{1,P,y} \\ \mathbf{b}_{1,P,z} \end{bmatrix} \tag{5.35}$$

The same ideas apply to the other matrices, submatrices, vectors and subvectors making up the system in Equation (5.22).

5.4.3 Repair of the backward-in-time Semi-Lagrangian search

When the approximation of the advective term through the SL method is applied to the nodes near and over the master boundary, the backward-in-time search of the departure points of the particle trajectories may "leak" outward the periodic cell for a higher CFL number. Although the usual manner to correct this deviation is to push them back to the boundary in order to be interpolated, this event has to be repaired by compensating the distance among two correspondent periodic nodes when PBC are implemented.

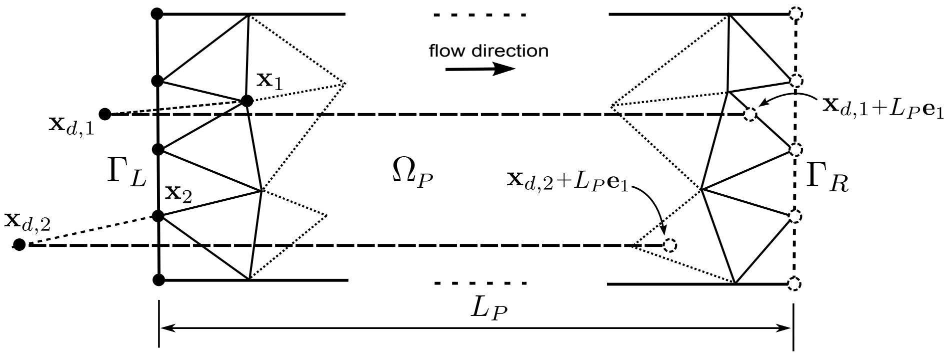

Figure 31: Displacement of the “leaked” departure points to correct the Semi-Lagrangian backward-in-time search in a periodic domain.

Considering that we only deal with parallel boundaries here, this computation is done simply by adding once the length of the domain to the points whose streamwise coordinate value falls outside the domain limits. Through this mechanism, the escaped points along the time are rebounded to the opposite side, thus entering back into the domain. Potential flaws of interlement discontinuities are removed with such repair so that the correctness of the advective interpolation as well as the cyclic behaviour of the simulation are ensured. A two-dimensional schematic representation of this repair is depicted in Figure 31 for $\mathbf{e}_P = \mathbf{e}_1$. The condition for the departure points is given by the code snippet below concerning the streamwise $x-$direction. Points $\mathbf{x}_j$ are advected backward-in-time to the departure points $\mathbf{x}_{j,d}$, which are displaced toward the flow direction to the points $\mathbf{x}_{j,d} + L_P\mathbf{e}_1$.

```
for $\mathbf{x}_j \in \mathscr{T}_h$ do
    Finds $\mathbf{x}_{j,d}$
    if $\mathbf{x}_{j,d} \cdot \mathbf{e}_1 < \min\{\mathbf{x}_{j,d} \cdot \mathbf{e}_1\}$ then
        $\mathbf{x}_{j,d} \cdot \mathbf{e}_1 \leftarrow \mathbf{x}_{j,d} \cdot \mathbf{e}_1 + L_P$
    end
end
```

6 CODE VALIDATION

6.1 Taylor vortex in highly viscous fluid

6.1.1 Spatial validation of PBC

A single-phase flow manufactured test to verify the spatial DOFs copying process over the periodic boundaries is presented in this section. The domain is a simple cuboid of dimensions $1.5L_{ref} \times L_{ref} \times 0.2L_{ref}$, where L_{ref} is the width as depicted in Figure 32. A Taylor vortex, which is an analytical solution of the Navier-Stokes equations [?], is placed over the domain as initial condition to evaluate the numerical error produced by addition of the PBC in the computational code. The vortex's velocity profile is written in dimensionless cylindrical coordinates as

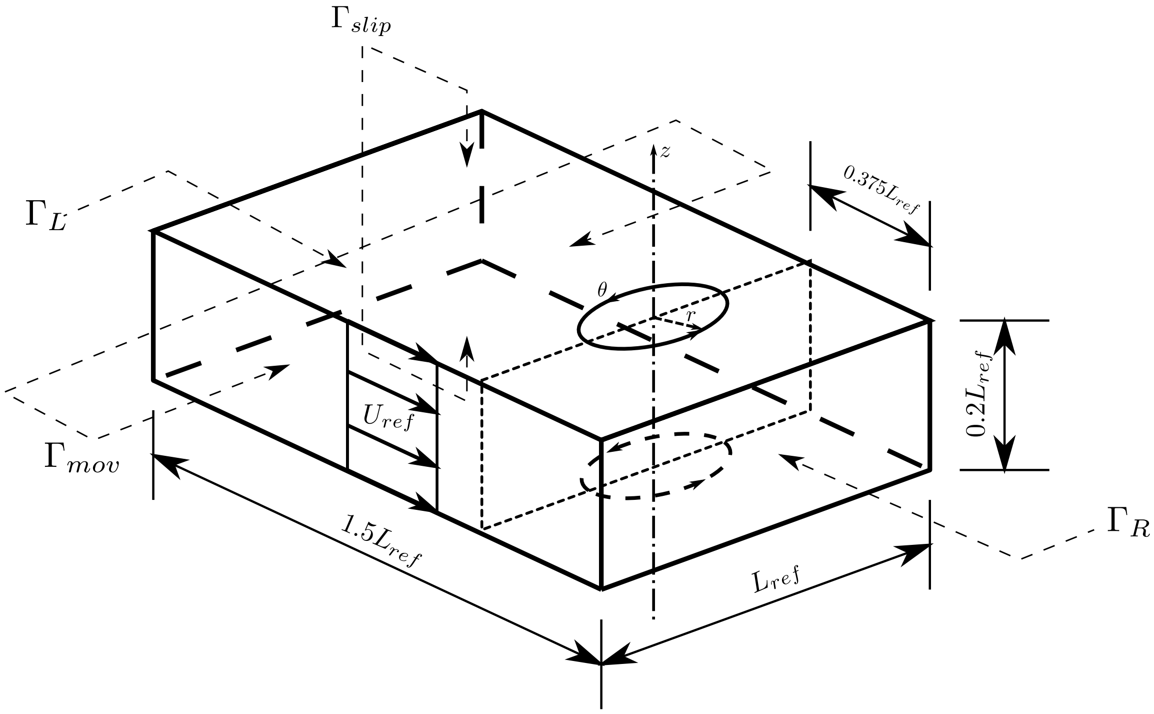

Figure 32: Periodic domain of simulation for a Taylor vortex carried away in a high viscous fluid flow.

$$v_r(t) = 0 \tag{6.1a}$$

$$v_\theta(t) = \varpi r \exp\left(-\frac{r^2}{4r_c Re^{-1}} t\right) \tag{6.1b}$$

$$v_z(t) = 0 \tag{6.1c}$$

Parameter	Value
r_c	$L_{ref}/30$
U_{ref}	1
ϖ	1
Re	35
Sc	650
Δt	0.1

Table 2: Physical parameters of the Taylor vortex flow.

and transformed to cartesian coordinates as

$$v_x(t) = U_{ref} - v_\theta(t)\sin(\theta) \tag{6.2a}$$

$$v_y(t) = v_\theta(t)\cos(\theta) \tag{6.2b}$$

$$v_z(t) = 0 \tag{6.2c}$$

to work as input data. Above, ϖ is the circulation, r_c is the vortex's core radius in the v_θ-profile, and U_{ref} is an increment of tangential velocity added to push the vortex downstream. Once the transient parcel of the tangential velocity decays rapidly with time, the time step Δt as well as the fluid flow properties were selected to produce a qualitative analysis of the vortex's hydrodynamics during this short period of unsteadiness as listed in Table 2.

Besides the enforcement of the PBC for velocity and pressure already expounded in Equations (5.11 - 5.14) over Γ_L and Γ_R , the additional boundary conditions for this test are slip (Γ_{slip}) for the top and bottom surfaces and of moving walls (Γ_{mov}) for the lateral surfaces as follows:

$$\mathbf{v}\cdot\mathbf{t} = U_{ref};\ \ \mathbf{v}\cdot\mathbf{b} = \mathbf{v}\cdot\mathbf{n} = 0, \quad \text{at} \quad \Gamma_{mov} \tag{6.3a}$$

$$\mathbf{v}\cdot\mathbf{n} = 0, \quad \text{at} \quad \Gamma_{slip} \tag{6.3b}$$

Observe that **n** points outward the domain's walls and **b** is the binormal vector per wall. To anticipate the periodic passage of the vortex through the walls Γ_L and Γ_R, its center is shifted from the domain's center toward this side.

The relative error of velocity measured in the $\mathscr{L}^2$-norm for this test is plotted in Figure

33 and computed as

$$\mathbf{e}_{rel} = \left\{ \int_{\Omega} \frac{(\mathbf{v}-\mathbf{v}_h)^2}{\mathbf{v}_h^2} \right\}^{\frac{1}{2}} \tag{6.4}$$

The error curve limited by $\mathscr{O}(10^{-3})$ decreases monotonically until getting a minimum. Due to the fast vortex's dissipation observed, the analysis was performed in the range $0 \leq t < 2.8$.

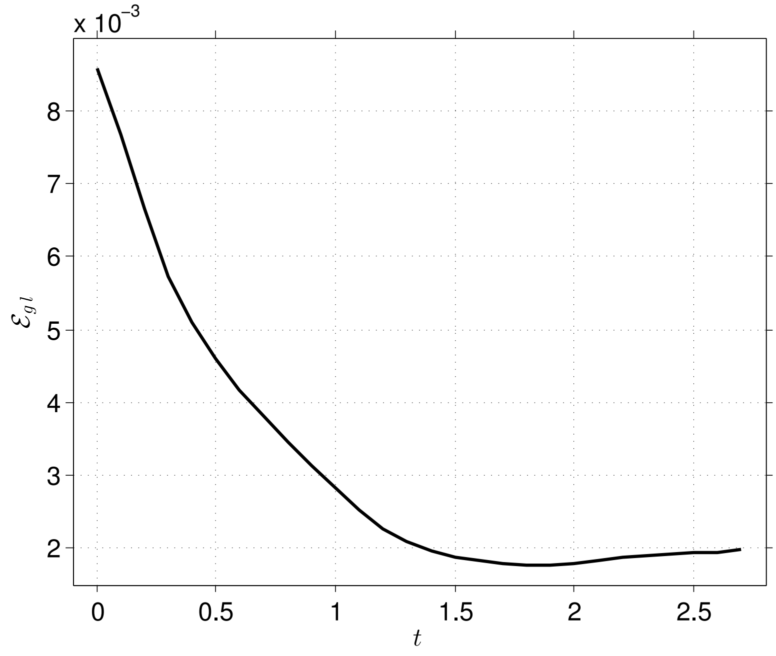

Figure 33: Relative error in $\mathscr{L}^2$-norm of the velocity profile for the Taylor vortex flow.

6.1.2 Scalar transport with PBC

In addition to the hypothetical viscous fluid being simulated, the Gaussian profile of a scalar quantity described in Equation (6.5) was also distributed initially throughout the domain to verify the compatibility of PBC for cases of a passive scalar transportation with $Sc \approx 650.0$. Such conditions can, for instance, describe the spreading of contaminants through sludge flows - provided that the hypothesis of Newtonian fluid is valid -, dissolved salts in industrial mixing as well as represent the advection of low diffusivity chemical agents interspersed in highly viscous liquids.

$$\phi(\mathbf{x}) = a \exp\left[-\frac{(\mathbf{x}\cdot\mathbf{e}_2 - \mathbf{x}_m)^2}{2b^2} \right] \cos(\mathbf{x}\cdot\mathbf{e}_1), \quad b = \frac{1}{2\pi} \tag{6.5}$$

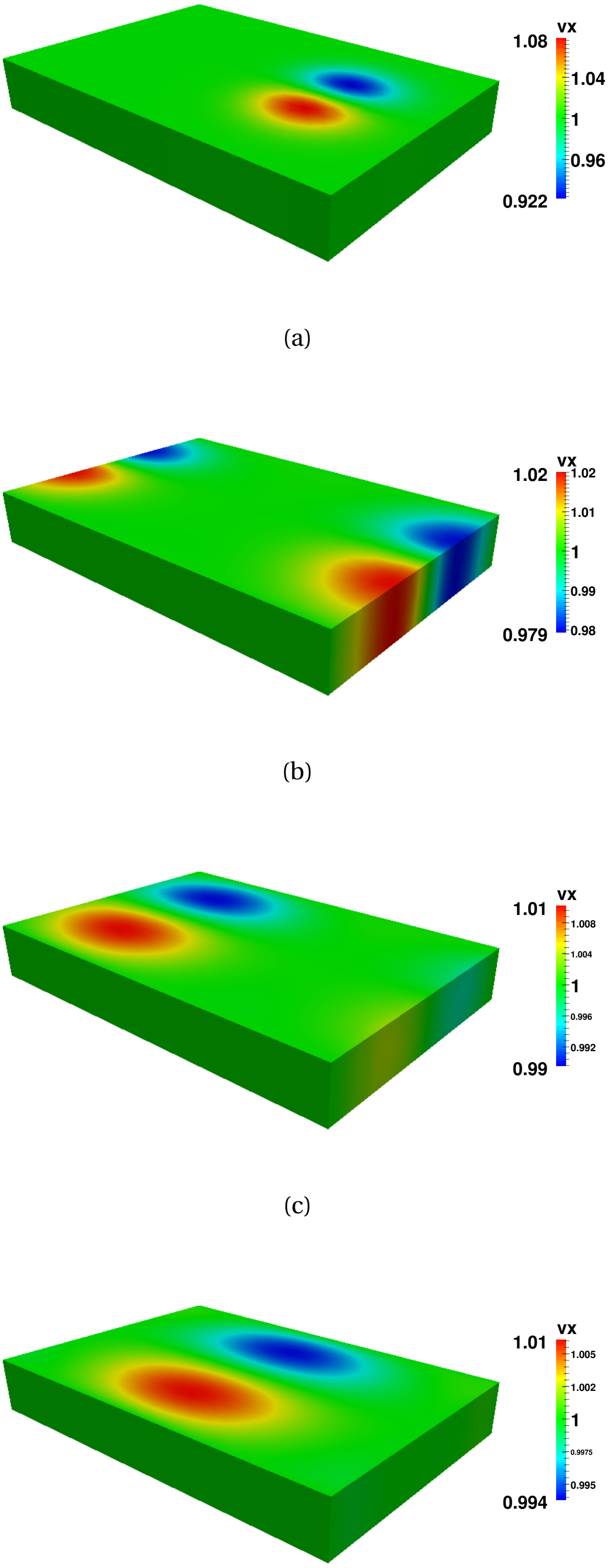

(a)

(b)

(c)

(d)

Figure 34: Taylor vortex's velocity profile v_x : (a) $t = 0.0$; (b) $t \approx 0.4$; (c) $t \approx 0.8$; (d) $t \approx 1.2$.

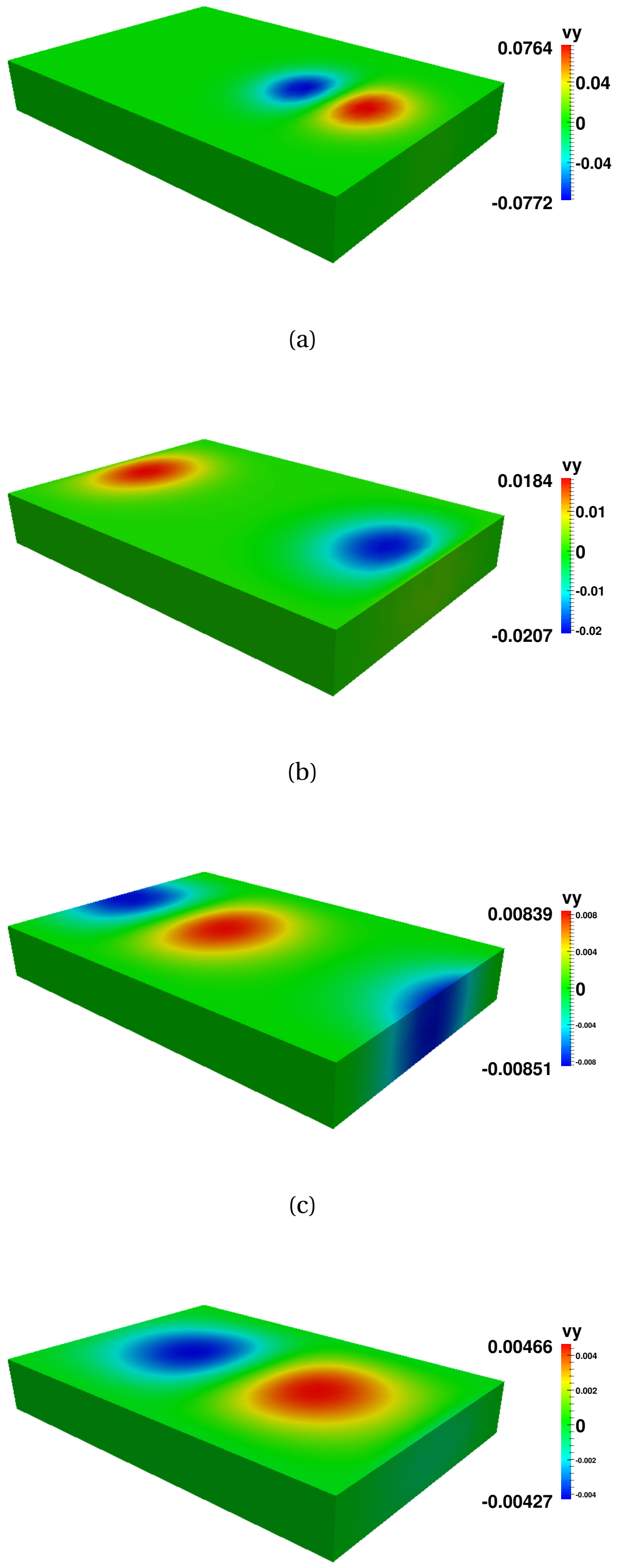

(a)

(b)

(c)

(d)

Figure 35: Taylor vortex's velocity profile v_y: (a) $t = 0.0$; (b) $t \approx 0.4$; (c) $t \approx 0.8$; (d) $t \approx 1.2$.

where $\mathbf{x}_m$ is a point on the central plane parallel to the flow and the peak $a = 0.8$. Consequently, the periodic boundary condition

$$\phi|_{\Gamma_L} = \phi|_{\Gamma_R} \tag{6.6}$$

must accompany the Equations (6.3a) and (6.3b). Some pictures of the vortex's streamwise

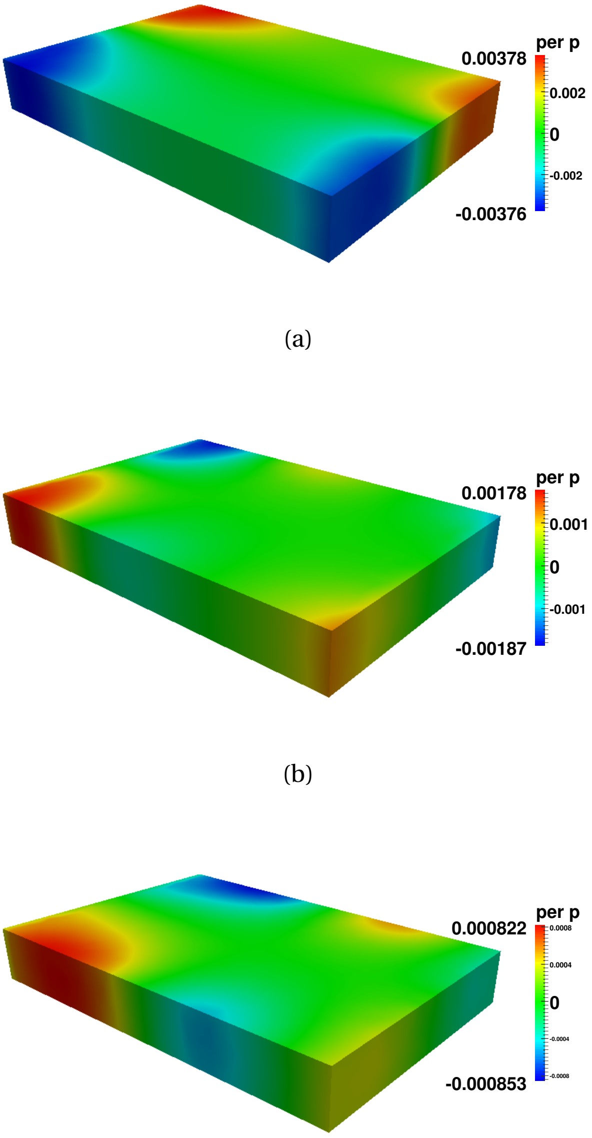

(a)

(b)

(c)

Figure 36: Taylor vortex's periodic pressure profile $\tilde{p}$: (a) $t \approx 0.4$; (b) $t \approx 0.8$; (c) $t \approx 1.2$.

and transverse velocity profiles, periodic pressure field, and scalar field are depicted in Figure 34 and Figure 37 for three time instants, besides the initial condition. As seen, the continuity of the profiles, before, during, and after crossing the periodic walls show the validity of the

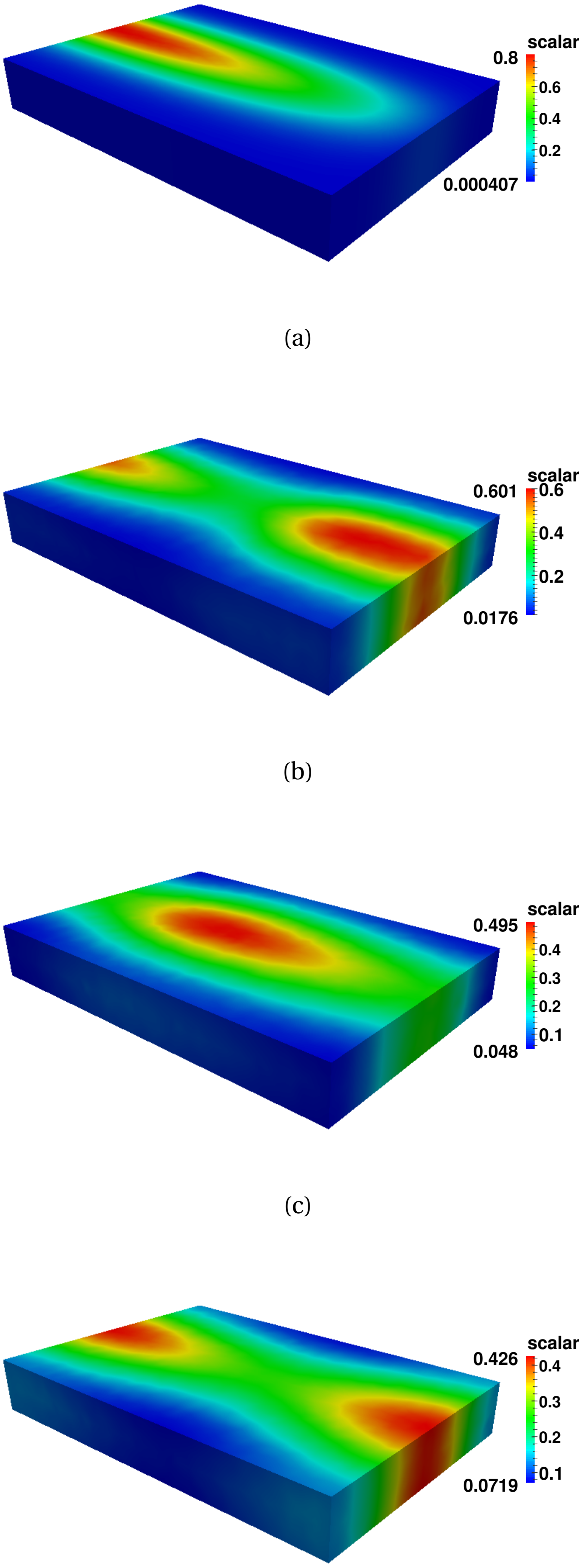

(a)

(b)

(c)

(d)

Figure 37: Scalar ϕ being carried by the fluid flow: (a) $t = 0.0$; (b) $t \approx 1.1$; (c) $t \approx 2.0$; (d) $t \approx 2.9$.

copying process embedded in the algorithm. In Figure 36, since the periodic pressure field is zero at the initial instant, the picture was suppressed of the roster. On the other hand, as depicted in Figure 37, the prolonged diffusion of the scalar field allows its observation a little further beyond from the state saturated achieved more rapidly by the velocity.

6.2 **Air bubble plume rising in quiescent water**

6.2.1 Periodic array of in-line rising bubbles

Let $\Omega \subset \mathbb{R}^3$ be the domain depicted in Figure 38 and Γ its boundary defined as $\Omega = \Omega^1 \cup \Omega^2$ and $\Gamma = \Gamma^1 \cup \Gamma^2$, with $\Gamma^2 = \Gamma^\infty \cup \Gamma^P$, where the subscripts 1,2 indicate, respectively, the dispersed phase and continuous phase of the flow, Γ^∞ the Dirichlet portion of Γ^2, and Γ^P its supplementary periodic portion. Here, Γ^∞ is placed far from the bubble plume to account for the bulk liquid region where the local interactions are mitigated. This boundary receives a moving wall condition to ensure the well-known MFR technique (cf. Section 7.2, while the PBC are assigned to $\Gamma^P = \Gamma^T \cup \Gamma^B$. The surfaces Γ^T and Γ^B satisfy $\Gamma^T \equiv \mathbf{x} + L\mathbf{e}, \forall \mathbf{x} \in \Gamma^B$ for a unit vector $\mathbf{e}$ as depicted by the element patches in light gray, i.e. the upper boundary Γ^T is topologically equivalent to Γ^B by a displacement L. The extended plume model consists of an arrangement containing spherical bubbles of diameter D_b equally spaced from above and below (relative to the poles) by a gap length $s = D_b$ and immersed into a cylinder of diameter $D \gg D_b$, whereas the periodic cell considers a slice of this configuration. To take into account the effect of the periodic boundaries on the bubble wake region as well as minimize the effects of the lateral wall, we set $L = s + D_b$ and $D = 10D_b$ for the cell's period and diameter, respectively.

6.2.2 Mathematical model

A detailed test for the case of an air bubble rising in an aqueous sugar solution considering PBC and the upward force caused by the pressure gradient Eu_β (cf. Section 5.3) was used to check the mathematical model and compared to recently published results [**?**]. For the bubble plume, the equations valid for both phases separately, are written in the differential

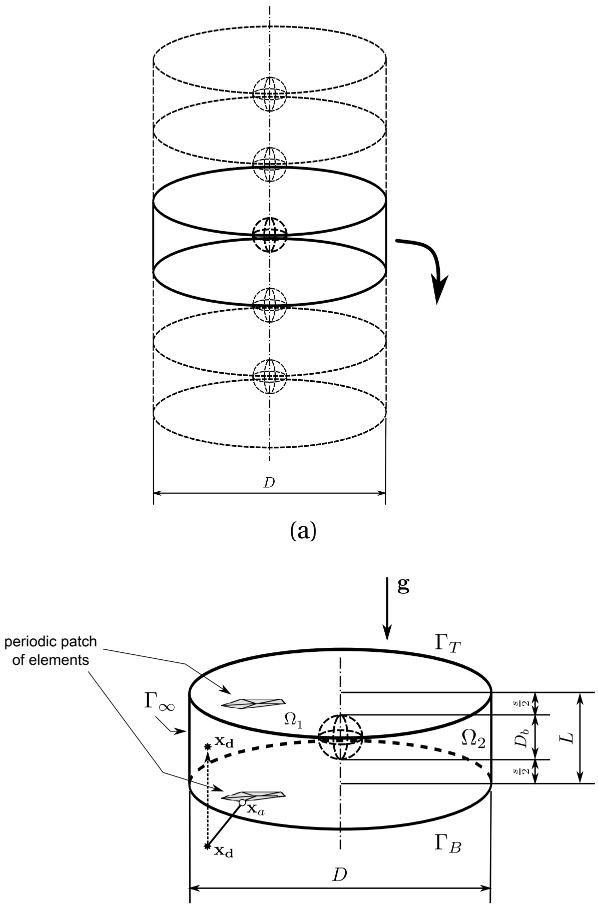

(b)

Figure 38: Arrangement of the unconfined in-line bubble plume: (a) extended plume model; (b) detail of the periodic cell.

form as

$$\rho\left(\frac{\partial \mathbf{u}}{\partial t} + (\mathbf{u}-\hat{\mathbf{u}})\cdot\nabla\mathbf{u}\right) = \lambda Eu_\beta \mathbf{e} - \nabla\tilde{p} + \frac{1}{Ar^{1/2}}\nabla\cdot\left[\mu\left(\nabla\mathbf{u}+\nabla\mathbf{u}^T\right)\right] + \rho\mathbf{g} + \frac{1}{Eo}\mathbf{f} \tag{6.7a}$$

$$\nabla\cdot\mathbf{u} = 0, \qquad \text{in} \quad \Omega\times t, \tag{6.7b}$$

with the dimensionless parameters Ar and Eo, viz. the Archimedes and Eötvös numbers, respectively, defined by means of

$$Ar = \frac{g_{ref} D_{ref}^3 \rho_{ref}}{\mu_{ref}^2} \qquad Eo = \frac{\rho_{ref} g_{ref} D_{ref}^2}{\sigma_{ref}}, \tag{6.8}$$

take the place of the Re and We number in Equation (3.40). In this case, $D_{ref} = D_b, \rho_{ref} = \rho^2, \mu_{ref} = \mu^2$. Moreover, for this analysis, a convenient way to obtain the dimensionless pressure gradient it is to divide Equation (5.5) by $\rho_{ref} g_{ref} D_{ref}$ and scale the reference velocity by $\sqrt{g_{ref} D_{ref}}$. Thenceforth,

$$p^* = -\left(\frac{\beta_{ref}}{\rho^2 g_{ref}}\right)\left(\frac{L_P}{D_b}\right)(\mathbf{x}^* \cdot \mathbf{e}^*) + \tilde{p}^* \tag{6.9}$$

gives the dimensionless form (the asterisk was dropped out)

$$p = -\lambda Eu_\beta(\mathbf{x} \cdot \mathbf{e}) + \tilde{p}, \tag{6.10}$$

with

$$Eu_\beta = \frac{\beta_0}{\rho^2 g_{ref}}, \lambda = \frac{L_P}{D_b}. \tag{6.11}$$

Since ρ_{ref} is taken to be the liquid density ρ^2 , Eu_β can be interpreted this time as the ratio of the upward body force to the gravitational force, which acts to balance the liquid mass contained in the periodic cell. Consequently, at steady state, $Eu_\beta \approx \mathcal{O}(\rho^2 \mathbf{g} \cdot \mathbf{e}) \approx 1$.

6.2.3 Mesh generation and adaptive refinement

For this study, the periodic mesh was constructed to enable the refinement control at specified regions of the domain and improve the analysis of the flow, since local interactions occurring near the bubble plume can be captured. Adaptive refinement strategies for the array of Figure 38 were developed to operate on the bubble's surface as well as over the fluid portion

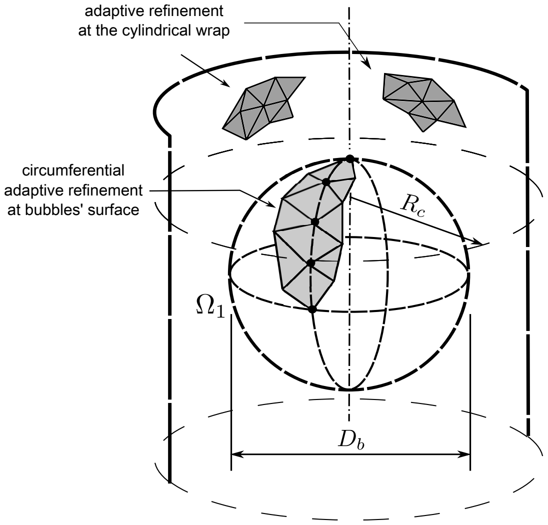

Figure 39: Augmented view of mesh displaying adaptive refinement strategies: circumferential, at the bubble's surface; azimuthal, at the cylindrical wrap region of radius R_c surrounding it.

wrapped by a cylindrical "envelope" of radius R_c surrounding the bubble, as illustrated in Figure 39. Such strategies afford not only the generation of finer surface meshes that distribute nodes circumferentially on the spherical shells, but also the achievement of smaller elements in the neighbourhood of the plume that produce good aspect ratios.

A view in perspective as well as a top-view of the unstructured mesh used for the bubble plume simulation are displayed, respectively, in Figure 40 and Figure 41 at a particular time instant so as to highlight the higher density of points around the center produced by the adaptive refinement.

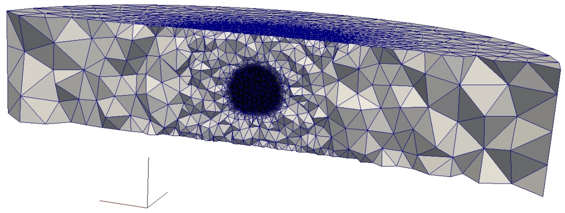

Figure 40: Computational mesh highlighting the bubble region: cut plane parallel to the axis of rising of the plume.

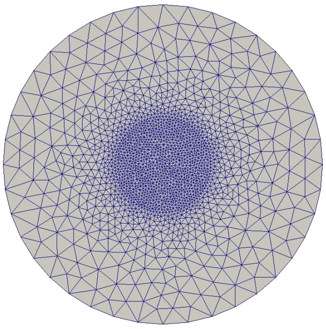

Figure 41: Computational mesh highlighting the adaptive refinement provided by the cylindrical wrap: top-view.

6.2.4 Validation tests

Figure 42 is a plot of the bubble's center of mass velocity $u_{bc}(t)$ versus time for three different simulations regarding physics and boundary conditions described as follows: test R1 - rising bubble with no-slip wall conditions everywhere under gravity only (closed boundaries); test R2 - rising bubble with lateral no-slip wall conditions, open boundary conditions at the top/bottom walls under gravity and upward body force; test R3 - rising bubble with lateral moving wall conditions, PBC at the top/bottom walls under gravity and upward body force. Test R1 is discussed in [**?**] for a parallelepipedal domain and good accordance is attained

Data					
μ^1, μ^2	ρ^1, ρ^2	σ	D_b	Ar	Eo
1.78e-5, 0.54	1.22, 1350	7.8e-2	2.61e-2	1092	116

Table 3: Physical property values for the numerical simulations: tests R1-R3.

here for a long cylindrical mesh; test R2 was performed to evaluate the balance between the gravity and pressure gradient forces inside the artificial array; test R3, in turn, was carried out to validate the complete PBC formulation coupled with the balance of forces. All of the three tests were carried out over the same computational mesh, whose radius/height are, respectively, $4D_b/10D_b$, and the physical property values for them are listed in SI units in Table 3. The time step computation depends on the mesh parameters as well as the other variables related to the ALE model, being updated each iteration (cf. Sec. 5.1 of [**?**]). For the current tests, an average time step $\Delta t \approx 0.003$ was determined.

As seen from the u_{bc} profiles in Figure 42, the tests are in mutual agreement, except for a slight profile discordance over the plateau of terminal velocity for the cases R2 and R3. To measure these deviations in relation to R1, the mean percentage difference within the time of simulation $[0, t_{max}]$ given by

$$\begin{aligned} \mathscr{E}_{Rj,R1} &= \frac{100\%}{t_{max}}\left(\frac{v_{bc,j}(t) - v_{bc,1}(t)}{v_{bc,1}(t)}\right), \quad j = 2,3, \text{with} \\ v_{bc,i}(t) &= \int_0^{t_{max}} u_{bc,i}(t)\,dt, \quad i = 1,2,3, \end{aligned} \tag{6.12}$$

was computed to be $\mathscr{E}_{R2,R1} = 3.97\%$ and $\mathscr{E}_{R3,R1} = 3.51\%$, thus reporting acceptable difference ranges for both the cases, being the smallest one reported for the PBC/MFR formulation proposed.

The deviations of R2 and R3 in relation to R1 is due to differences in the problem setups, including effects coming from the boundary conditions and the splitting process used to calculate the velocity field - as explained in Subsection 3.2.1. The tests were sensitive to the time step size chosen, since the addition of the pressure gradient Eu_λ introduced a numerical error of $\mathscr{O}(\Delta t)$ caused by the imbalance between gravity forces and pressure forces produced by the splitting process.

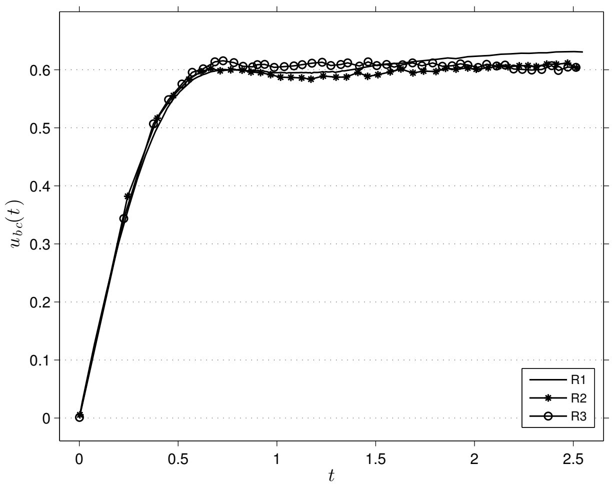

Figure 42: Dimensionless rising velocities $u_{bc}(t)$ for three different configurations of an air bubble rising immersed into a aqueous sugar solution.

6.2.5 Rising velocity, aspect ratios, trajectories and spectra

Bubble deformation and oscillation are intimately linked to flow properties, such as surface tension, bubble size, and inertia effects. The next subsections describe rising velocities, bubble shape and oscillation analyses for two cases of bubble plumes inside the periodic domain of Figure 38 ($L = 2D_b$), whose physical property and parameter values are listed in Table 4. For clarity, the cases are labeled as B1 and B2 and their underlying difference

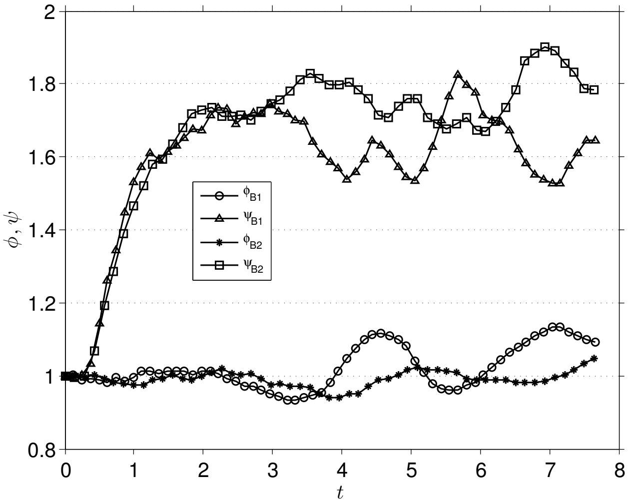

Figure 43: Elongation (ϕ) and flatness (ψ) ratios of the rising bubbles.

is related to the bubble diameter in the periodic cell, namely, 4.0 mm and 5.2 mm, respectively.

Curves of the two bubble shape factors were calculated and plotted in Figure 43, viz.

Table 4: Physical property values for the numerical simulations: cases B1 and B2, respectively. (from [**?**])

Case	μ^1, μ^2	ρ^1, ρ^2	σ	D_b	$Ar^{1/2}$	Eo
B1	18.2e-6, 958.08e-6	1.205, 998	0.0728	4e-3	824.96	2.15
B2	idem	idem	idem	5.2e-3	1222.8	3.63

the elongation and flatness ratios defined, respectively, as:

$$\phi = \frac{b}{c}; \quad \psi = \frac{c}{a}, \tag{6.13}$$

where a, b, c are the maximum length of the bubble's principal axes in the streamwise (chosen to be the x axis) and transverse directions (y and z axes). As seen, the initial condition (that is to say $\phi = \psi = 1$) of both the cases vouch for the perfectly spheroidal shape of the bubbles. With the time and the ascent motion of the bubbles, the flattening process dominates over the elongation up to $t \approx 2.5$, thus portraying an oblate shape with a dimple underneath the bubble comparable to experimental observations [**?**]. From this threshold, shape irregularities become more visible as oscillations are felt by the bubbles, without following, however, a defined periodicity. In turn, the shape variations occur freely as far as the end of the simulations, with the elongation profiles less protruded.

Path instabilities, zigzag and spiral motions for gas bubbles rising both in clean water and other liquids are effects recognized in literature and the mechanisms responsible for their appearing have been debated through different points of view (cf. [**?**], [**?**], [**?**], [**?**], [**?**]). It is known, however, that the bubble's mobility is deeply affected when impurities are dispersed in the flow. To compare with these results, qualitative behaviours were observed for the cases B1 and B2 in the periodic domain regarding the bubbles' trajectories and its projections as depicted in Figure 44. While in the first test the bubble underwent an off-center wobbling motion marked by acute spots, the second test presented, furthermore, a twist motion around the directrix line erected from the point $(y_t, z_t) = (0.09, -0.045)$, approximately between $t = 2$ and $t = 4$, before its full unfolding. Given the milimetric difference of diameters for the two cases, these curves suggest that the effect of the bubbles' wake brought onto themselves - in the sense of a plume made up by equally spaced bubbles - amounts to a path instability which depends on the bubble size and, therefore, on the Eötvös number, in accordance with arguments expressed in the previous citations. Besides, the trajectories tend to develop a

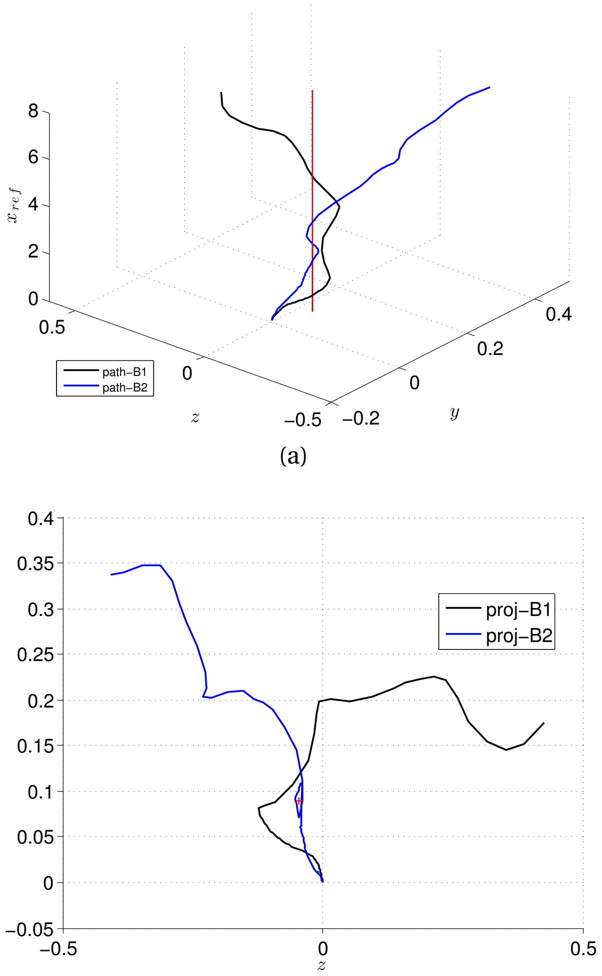

(a)

(b)

Figure 44: Bubbles' spatial motion relative to the reference frame moving upwards along with the center of mass (x_{ref} coordinate): (a) path and directrix line of the twist emerged in case B2 (in red); (b) projection of the paths over the $yz-$ and the directrix's base point $(y_t, z_t) = (0.09, -0.045)$ (in red).

seemingly chaotic path.

In attempting to quantify the harmonic modes involved in the oscillatory motion of the bubbles, a spectral analysis based on the fast Fourier transform (FFT) of the signals $\phi_j(t), \psi_j(t), j = 1, 2$, was performed. The spectral analysis considered only data on the range given by $t_S = [2.5, t_{max}]$, thus disregarding the initial evolution stage. FFT-based spectra of magnitude of disturbance energy computed through the expression

$$|FFT_{Bj}[F(t)]| = FFT[F(t)]\overline{FFT[F(t)]};$$
$$F(t) = \phi_j(t), \psi_j(t), \quad j = 1, 2, \tag{6.14}$$

with the overbar meaning complex conjugate, for the ten first harmonic modes, $1.0 \leq \frac{f t_S}{2\pi} \leq 10.0$, are depicted for the cases B1 and B2 in Figure 45. The analysis took into account a considerably large quantity of sampling data over the reduced temporal interval t_S, but it showed that the energies of higher magnitude are noticeable only at the low frequencies of the spectra.

This FFT-based analysis shows that both the cases have their energy peak concentrated in the second harmonic. This value is close to the frequencies associated to the (2,0) and the (2,2) modes reported in [**?**]. For the case B1 the energy peak associated to the flatness profile is only slightly more intense that the elongation's, while for the case B2 the elongation energy is much larger than the flatness energy. Furthermore, the energy of the case B1 is very concentrated on $\frac{f t_S}{2\pi} = 2.0$, whereas that of the case B2 is spread over the frequencies in the range $1.0 \leq \frac{f t_S}{2\pi} \leq 3.0$. On the other hand, a slight alternance of intensities between even and odd harmonics can be observed along the range, though the case B1 has a higher overall energy than the case B2. Considering that the spectra are nondimensional, the increased spreading in the frequencies in case B2 is indicative of a more complex behaviour.

Filtered rising velocity profiles for the cases B1and B2 are depicted in Figure 46. The need of filtering is firstly justified by the jump of density at the air-water interface, which implies small pressure variations inside the bubble, thus generating higher velocity therein; secondly, to remeshing operations inherent to the numerical method, such as insertion and deletion of nodes, that cause instantaneous variations in the center of mass's position. Consequently, a special treatment of box filtering is required to smooth the influence of short-time spurious oscillations experienced by the bubble while ascending. As seen, the fluctuations of velocity are intensified from $t \approx 2.5$, in accordance with the analysis previously reported.

6.2.6 Wake effects and near-field velocity

Analyses of the flow in the bubble's surroundings are limited here to a near-field distance, defined to be the periodic cell region below of $2D_b$ from the nondisplaced bubble's center of mass, and are conducted for each test in this subsection. Due to the complex imaging of the three-dimensional hydrodynamic field evolving around the bubble, two stacks of pictures gathering the velocity field as well as the bubble shape information at four time instants, namely $\{3.00, 4.50, 5.50, 6.50\}$, are arranged from Figure 47 to Figure 50 relative to

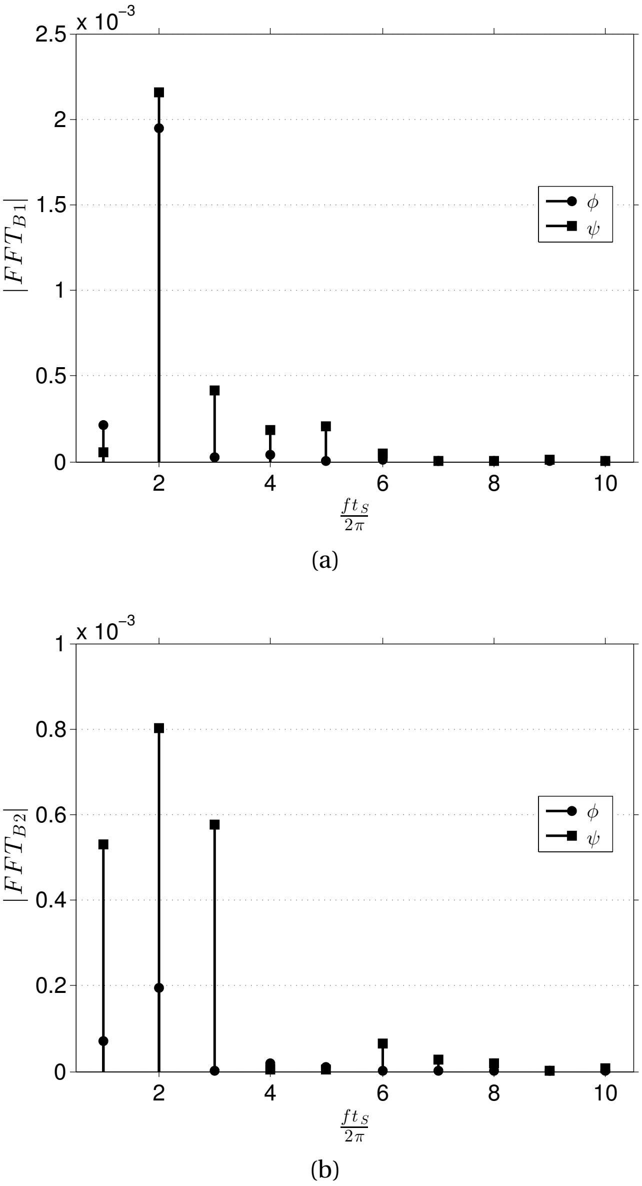

(a)

(b)

Figure 45: FFT-based spectrum of disturbance energy for the ten first harmonic modes relative to the signals representative of the aspect ratios profiles $\phi_j(t), \psi_j(t), j = 1,2$ evaluated in the interval $t_S = [2.5, t_{max}]$: (a) case B1; (b) case B2.

an axis whose center is fixed in the initial position of the bubble's center of mass. In the background, the magnitude of the velocity field is plotted over the transverse planes yx and zx; in the foreground, the bubble shape highlighting the zero-thickness finite element surface meshing is overlaid.

The downward flow reflects the imposition of the MFR technique by which the degrees of freedom of the streamwise velocity are subtracted by the center of mass velocity $-U_{bc}$ which is updated each time step. By comparing the flow evolution vis-a-vis for each pair B1-B2 of projection planes, some inferences about the overall flow can be drawn from the

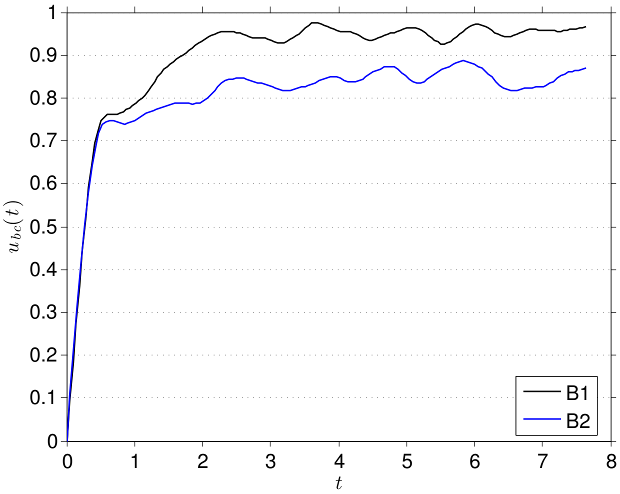

Figure 46: Dimensionless rising velocities $u_{bc}(t)$ over the bubble's reference frame for the cases B1 and B2.

simulation snapshots. Firstly, the oblate shape persists for a considerable time along the path and it is a common trait in both the cases; so is the wobbling motion, which is boosted up by higher velocity gradients in the bubble's skirt region around $t = 5.50$. Off-center motion is seen by contrasting the bubble shape at $t = 3.00$, a few instants after the oscillation outset, against $t = 6.50$; for instance, when the drift from the reference center is played by the bubbles. Consecutive inclinations of the bubbles concerning the azimuthal angle formed between their central axis and the streamwise axis are also exhibited on both projection planes concomitantly, thereby confirming the presence of wobbles in the spatial trajectories observed as much in the previous subsection as in the cited references. It is seen, moreover, that the dimple evolution underneath the bubble of the case B1 differs from that arising in B2, which is more restrained during this stage - however unclear from the pictures. Despite of that, the dimple existence can be verified from the smooth reentrant portions of counterflow underneath the bubbles and around their fringes.

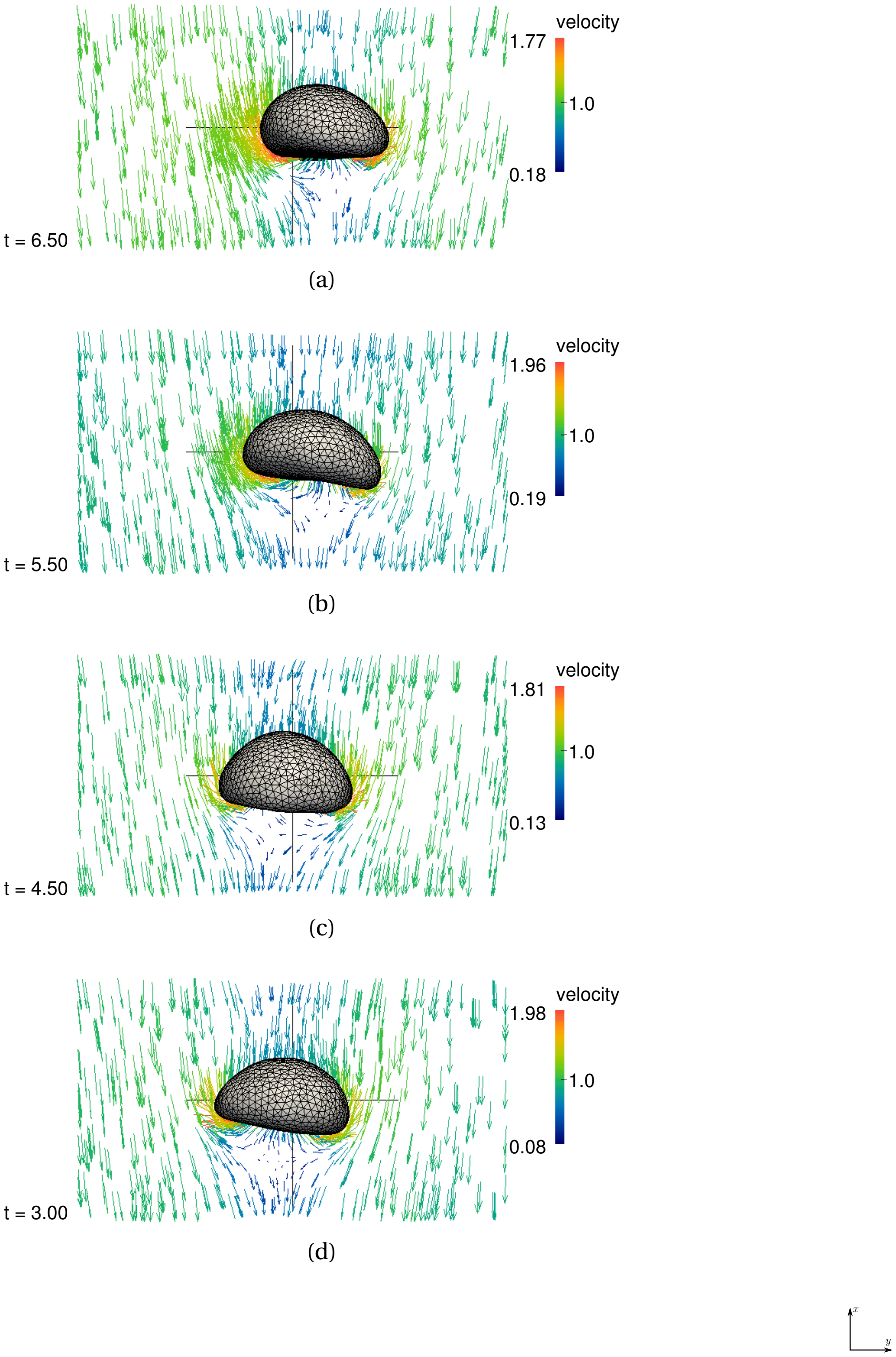

(a)

(b)

(c)

(d)

Figure 47: Velocity field and bubble shape for the case B1: plane yx; (a) $t = 3.00$, (b) $t = 4.50$, (c) $t = 5.50$, (d) $t = 6.50$.

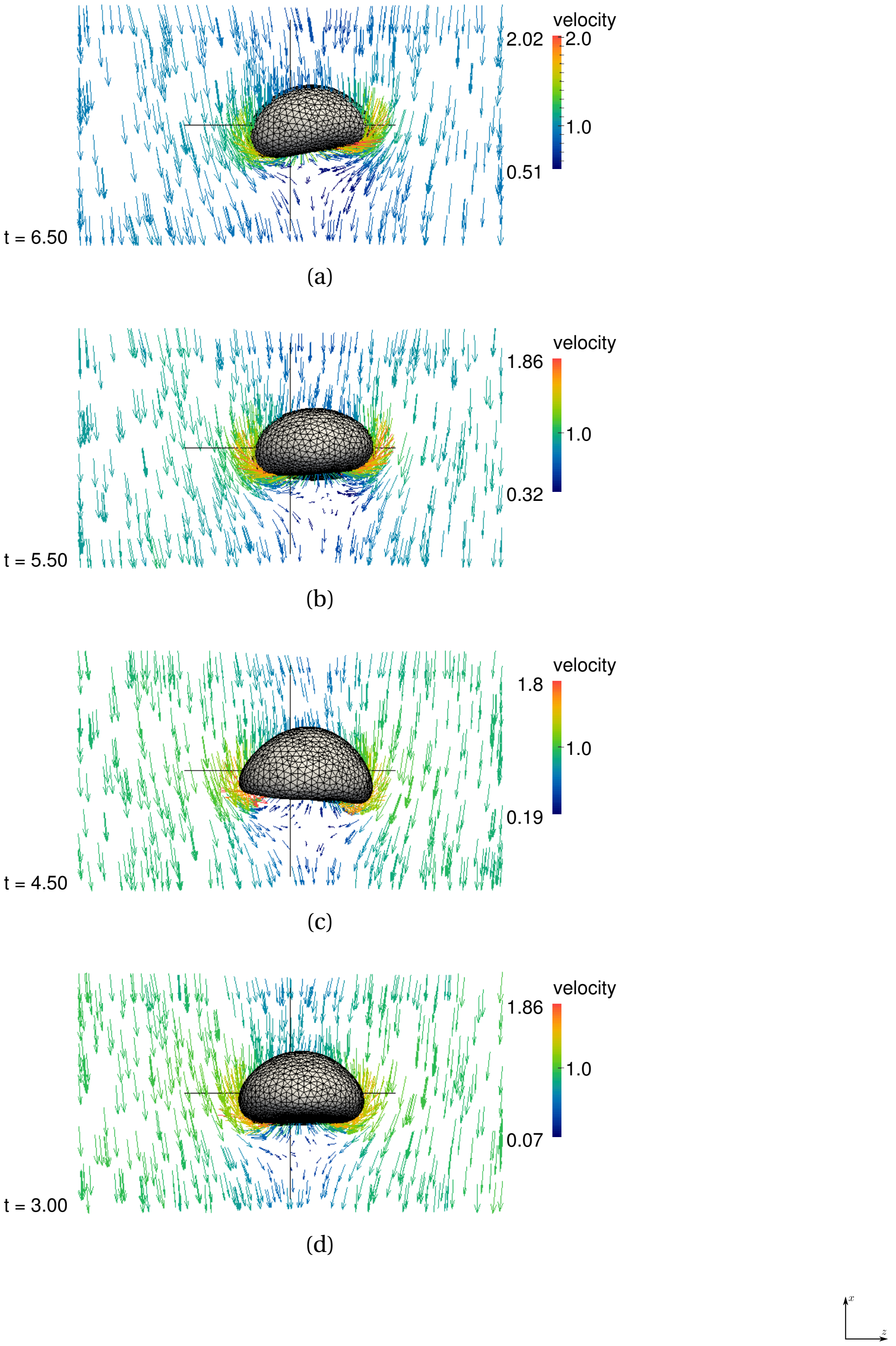

(a)

(b)

(c)

(d)

Figure 48: Velocity field and bubble shape for the case B1: plane zx; (a) $t = 3.00$, (b) $t = 4.50$, (c) $t = 5.50$, (d) $t = 6.50$.

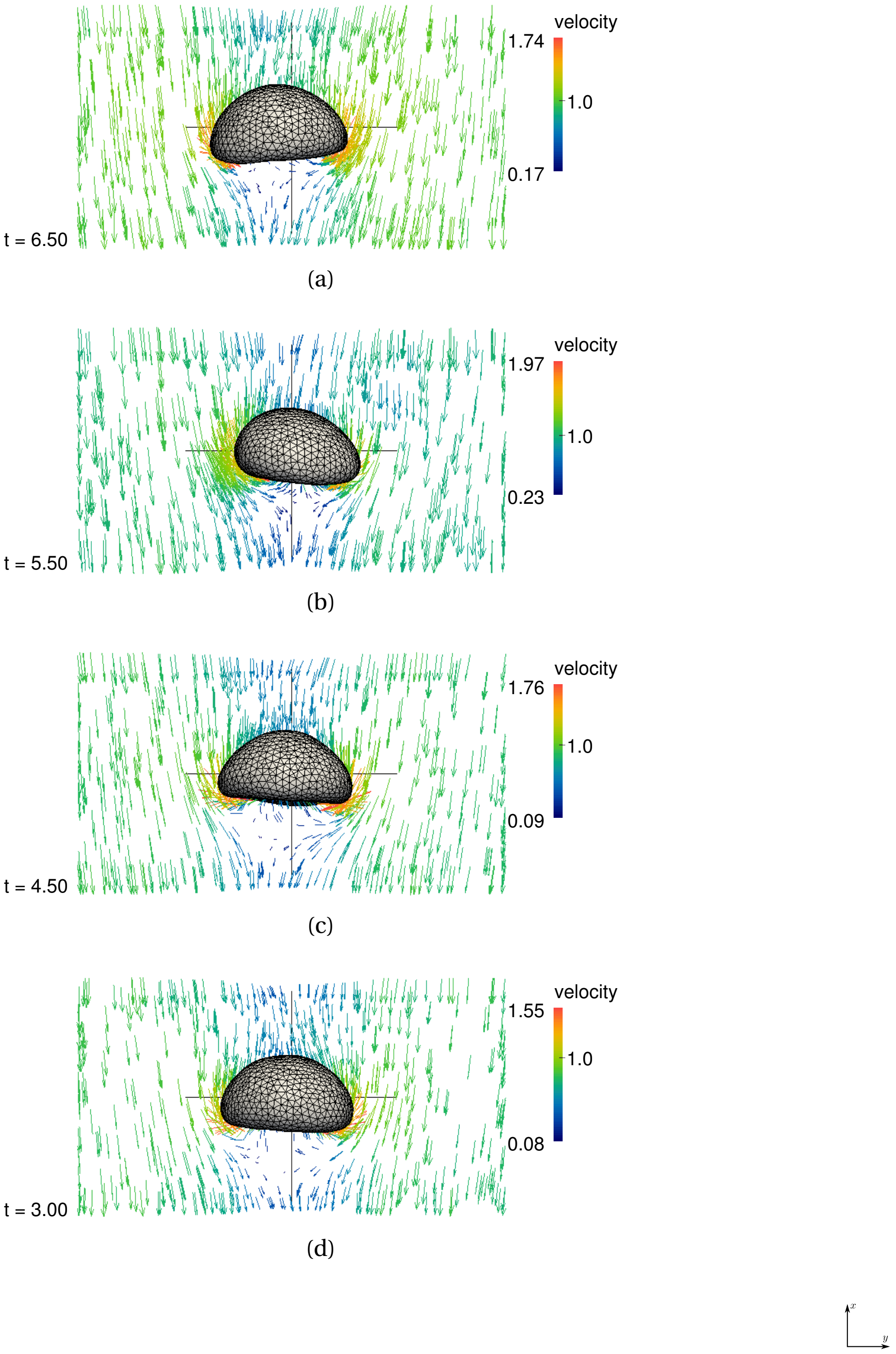

(a)

(b)

(c)

(d)

Figure 49: Velocity field and bubble shape for the case B2: plane yx; (a) $t = 3.00$, (b) $t = 4.50$, (c) $t = 5.50$, (d) $t = 6.50$.

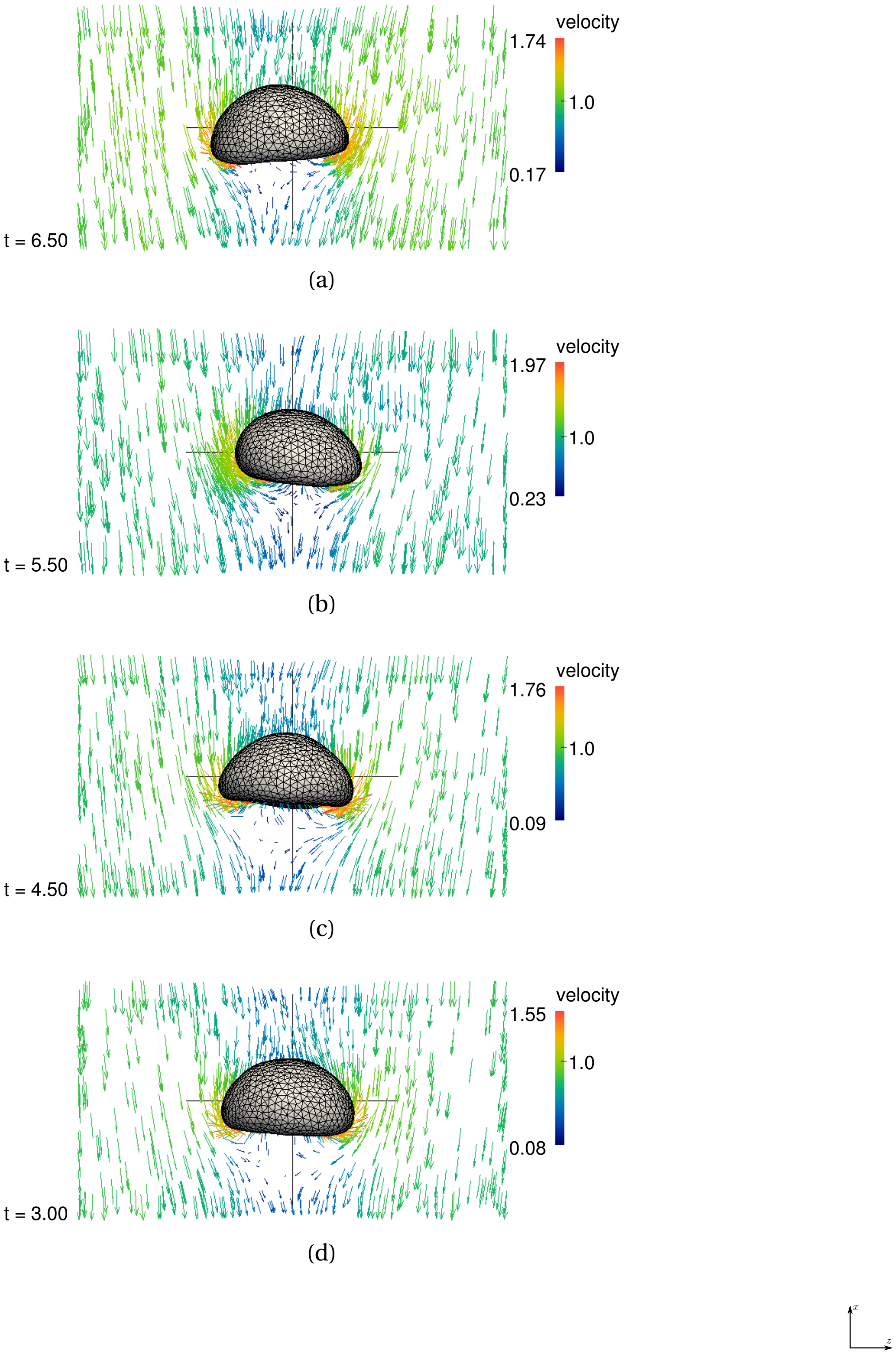

(a)

(b)

(c)

(d)

Figure 50: Velocity field and bubble shape for the case B2: plane zx; (a) $t = 3.00$, (b) $t = 4.50$, (c) $t = 5.50$, (d) $t = 6.50$.

7 THE DROP JET IN CROSSFLOW

7.1 Problem posing

With a physical meaning similar to the cases reviewed in Chapter 1, the flow of a liquid jet issued into another immiscible liquid portion after breaking in drops is analyzed. We focus on the primary breakup zone after the drop detachment and not on the mechanisms leading to the breakup. To give an insight about the whole description of the problem, we refer to the arrangement of the DJICF studied in this thesis as depicted in Figure 51.

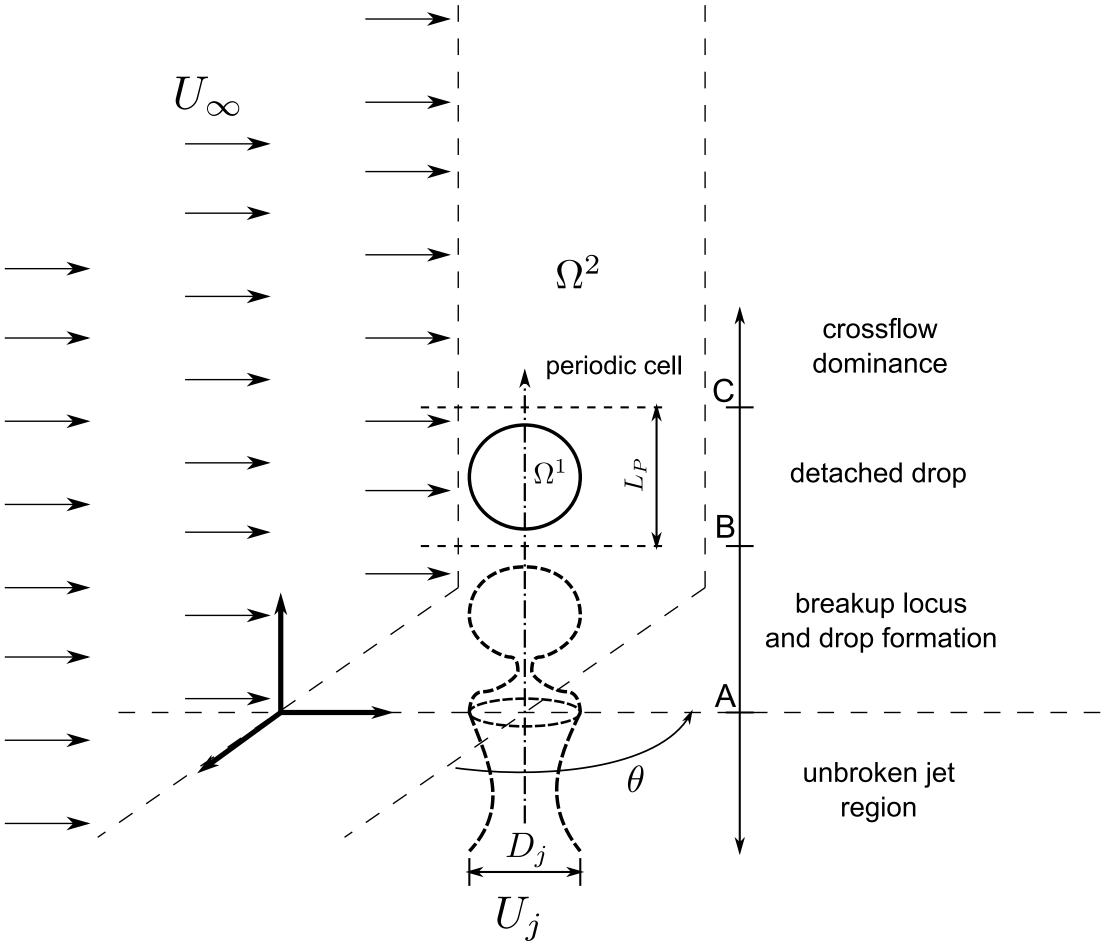

Figure 51: Arrangement of the DJICF.

The cylindrical-shaped jet is considered to expel drops of diameter D_j with velocity U_j in a periodic way and perpendicularly into an unconfined liquid portion Ω^2 whose crossflow velocity is U_∞. The unbroken jet region is below the point A. Between the points A and B, a Rayleigh breakup mode is assumed to occur and form the drop. During the short space between B and C, the drop is completely detached off the jet. Beyond the point C, the crossflow inertia is assumed to dominate over the jet deflecting the drop depending on the crossflow-to-jet velocity ratio λ. As it will be seen forth, the drop is modelled as a spherical body initially which may deform along its trajectory depending on the flow properties, mainly ruled by the We, Oh, Re and Ca numbers, where

$$Ca = \frac{We}{Re}\frac{\mu}{\lambda^{-1}} \tag{7.1}$$

is the *capillary number* here defined according to [**?**] for the viscosity ratio $\mu = \mu_1/\mu_2$. In this preliminary study, gravity effects are not considered, just as the relevance of the Fr number.

To account for the PBC, the periodic cell is placed around the drop by enclosing it inside a certain period length L_P. Since this approach imparts a limited treatment of the flow, a MFR technique is additionally incremented in the modelling in attempting to analyze deflection, topological changes and hydrodynamic effects over and surrounding the drop enclosed by this simulation box. The relation between fixed and moving reference frames as well as the collocation of the periodic cell domain and boundary conditions are elucidated by observing Figure 52. In this idealized diagram, the drop, after detaching off the jet, travels in

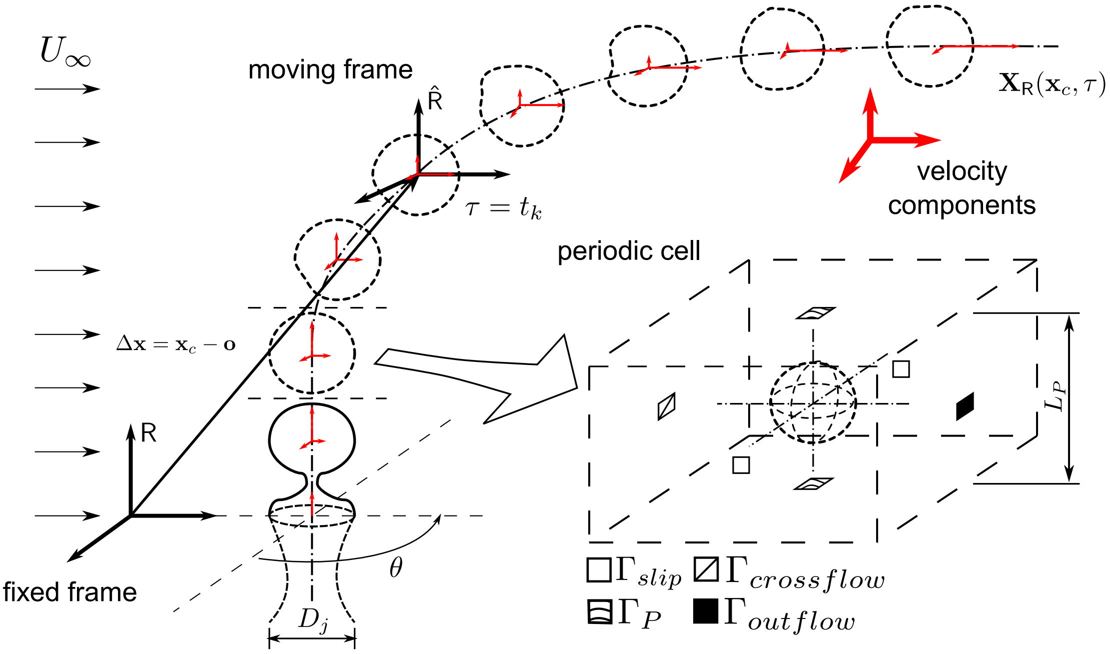

Figure 52: Relation between fixed and moving reference frames in the DJICF flow as well as an overview of the periodic cell domain with the selection of the boundary conditions.

space undergoing the influence of the crossflow. Several configurations of the drop along its trajectory are drawn in dashed lines. The velocity components following the drop's motion are placed at its center of mass $\mathbf{x}_c$, which performs the trajectory described by the curve $\mathbf{X}_{\mathsf{R}}(\mathbf{x}_c, \tau)$. When establishing the relation between the physical reference frames, the called *fixed frame* is firstly defined by R which, in this generalized scheme, is placed at a convenient site in the continuous domain Ω^2. The second referential, defined by $\hat{\mathsf{R}}$, is called the *moving frame* and it is placed at the drop's center of mass so that

$$\Delta\mathbf{x} = \mathbf{x}_c - \mathbf{o} \tag{7.2}$$

represents the displacement of the drop's center of mass in relation to the origin **o** of R. At right, in the same figure, the computational periodic cell is laid out as a cuboid whose boundaries are divided into four groups represented by painted snips, namely, Γ_{slip}, Γ_P, $\Gamma_{crossflow}$ and $\Gamma_{outflow}$. More specifically, aside the PBC and NBC, the DBC obey

$$p = 0 \quad \text{at} \quad \Gamma_{outflow} \tag{7.3}$$

$$\mathbf{v}\cdot\mathbf{n} = V_\infty \quad \text{at} \quad \Gamma_{crossflow} \tag{7.4}$$

$$\mathbf{v}\cdot\mathbf{n} = 0 \quad \text{at} \quad \Gamma_{slip}, \tag{7.5}$$

for **n** normal to its respective wall.

7.2 Moving frame reference technique

The MFR technique resorts to a strategy based on reference frames while creating a relative context of interaction between Eulerian and Lagrangian descriptions. In this thesis, the MFR approach is used together with the enforcement of PBC in order to reduce the computational cost of the simulations when reducing, mainly, mesh size and number of DOFs (see, e.g. Subsection 6.2.1).

Generally, MFR codes are used to simulate dispersed flows in their several configurations in which the dispersed bodies remain stopped with time whilst the boundaries encircling them are placed in relative motion. Although the idea behind this technique can be extended for other cases, examples of such applications with or without PBC are found, mainly, in simulations of bubble or drop flows, as studied in [**?**], [**?**], [**?**], [**?**]. Whereas all of these papers use MFR for unidirectional flows only, this section describes the additional details of implementation of the MFR technique by considering the existence of transverse flows as well. Since this approach is adapted for the DJICF problem, the two-dimensional periodic cell scheme depicted in Figure 53 will be used as an extension of those seen in the previous section. Given that the drop has velocity U_j, if $U_\infty \neq U_j$ a curved trajectory is experienced by the drop even for a minimal displacement. Let us consider, however, $B(\tau = t), B(\tau = t+\delta t)$ two configurations of an arbitrary dispersed body B at two time instants. In relation to a cartesian fixed frame R, the entire body undergoes an infinitesimal displacement of $(\delta x, \delta y)$ from left to right with its center of mass traveling according to the Lagrangian trajectory $\mathbf{X}_{\mathsf{R}}(\mathbf{x}_c;\tau)$. On the other hand, the moving frame $\hat{\mathsf{R}}$ attached to the body's center of mass $\mathbf{x}_c$ which follows the body motion in space and time, at first, should remain fixed for all the time at the position of the center of mass identified in space when $\tau = t$, thus conveying the dynamics to an Eulerian point of view.

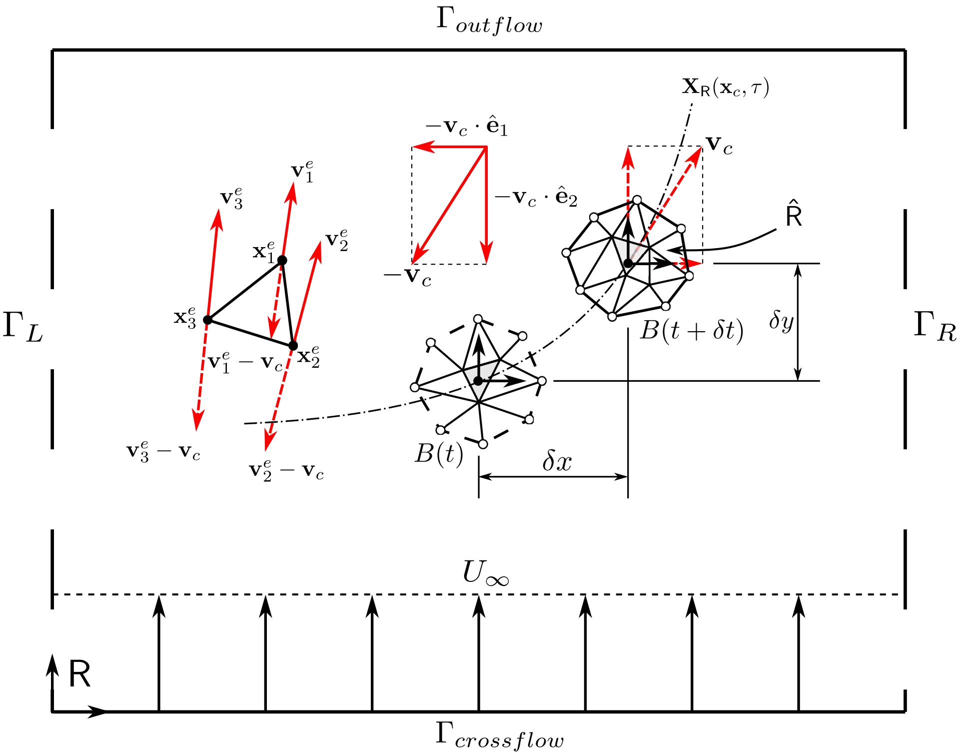

Figure 53: Scheme of the displacement of a drop in crossflow and implementation of the moving frame technique.

Whilst, physically, the instantaneous velocity

$$\mathbf{v}_{inst} = \lim_{\delta t \to 0} \frac{\delta \mathbf{x}}{\delta t} \tag{7.6}$$

is responsible for the infinitesimal displacement of the body within $t \leq \tau \leq t + \delta t$, numerically, the velocity evaluated at the center of mass is the parameter playing the fundamental role in the discrete time step Δt. Therewith, two numerical steps arise: the computation of the velocity and position of the center of mass and the determination of the body's retardment. The former will be discussed in Subsection 7.2.1; the latter, next.

Since the center of mass' velocity $\mathbf{v}_c$ is determined for each time instant, all the flow field should undergo a retardment of velocity given by

$$\mathbf{v}_{rel} = \mathbf{v} - \mathbf{v}_c \tag{7.7}$$

to create a relative field so that the body B, after it has been displaced to $B(\tau = t + \delta t)$, be brought back to its position at $B(\tau = t)$. The effect of such subtraction of the flow's velocity field is drawn in red lines in Figure 53 as much for the body itself as for an arbitrary element e of the continuous phase Ω^2. That is to say, for each triangular element with vertices $\mathbf{x}_j^e$, $j = 1,2,3$, the resulting velocity $\mathbf{v}_c$ is summed to the nodal velocities with opposed sign to give $\mathbf{v}_{rel;e}^j = \mathbf{v}_j^e - \mathbf{v}_c$, $j = 1,2,3$. As explained by [**?**], the interplay between inertial and stationary reference frames works as a correction scheme that may suffer the influence of a wave pressure that eventually dissipates during the simulation since the body is forced to go back and forth each time step, thus requiring some numerical artifice. In this thesis, the numerical steps to implement the MFR technique are represented in the algorithm below:

```
for $t : (0, T]$ do
    $\Delta\mathbf{x}(t) = \mathbf{x}(t) - \mathbf{x}(t = 0)$ ;                    /* displacement */
    $\mathbf{v}_{inst}(t) = \mathbf{v}_c(t) + \frac{\Delta\mathbf{x}}{\Delta t}$ ;    /* accumulating instantaneous velocity */
    $\mathbf{v}_{\mathrm{R}} = \mathbf{v}(t) + \mathbf{v}_{inst}$ ;      /* recovering velocity - relative to FFR */
    $\mathbf{x}_{\mathrm{R}} = \mathbf{x}(t) + \mathbf{v}_{\mathrm{R}}\Delta t$ ;      /* recovering position - relative to FFR */
    $\mathbf{v}(\Omega) = \mathbf{v} - \mathbf{v}_{inst}(t)$ ;  /* corrected relative velocity - flow field */
end
```

It should be pointed out that such retardment operations require an update not only of the DBC to take the changes of the flow field into account, but also of the code variables that store the velocity values, which are reused in the iterative process.

7.2.1 Computation of averaged quantities

As aforementioned, the computation of the velocity and position of the center of mass of a dispersed body is necessary not only for the establishment of the MFR technique, but also for a considerable amount of discrete quantities in the FE ambit. Generally, the center of mass $\mathbf{x}_c$ is an interior point not matching a mesh node as depicted by the dark points inside the shaded triangular elements in Figure 53. Then, under the numerical point of view, every property $\phi(\mathbf{x}_c)$ is computed at element level through a global average of elementary nodal values. For the specific case of determining the position and velocity of the center of mass of a dispersed body, the following approximated version of integrals is computed:

$$\begin{aligned} \phi(\mathbf{x}_c^g) &= \left(\frac{\iiint \phi \, dV}{\iiint \, dV} \right)_{\Omega_g^1}, \quad g = 1,2,\ldots,nb \\ &= \frac{\sum_{e=1}^{E} \phi_{c,e}^g V_e^g}{\sum_{e=1}^{E} V_e^g}; \quad \phi_{c,e}^g = \frac{\sum_{j=1}^{\#J} \phi^g(\mathbf{x}_j^e)}{\#J}, \quad J = m+1, \end{aligned} \tag{7.8}$$

where nb is the number of dispersed bodies, E is the number of simplices making up each dispersed body, J is the number of vertices of the element and V stands for volume. These formulae apply for each component separately in $\mathbb{R}^3$. Note, additionally, that, if $m = 2$, the computations can be performed by replacing the volume integrals by area integrals and doing the necessary modifications.

7.3 Numerical direct simulations

This section presents the main results of this thesis concerning the full 3D simulations of the DJICF configuration. The liquid-liquid pairs chosen relate to well-known experimental tests.

7.3.1 Initial condition

Because of the DJICF problem is based on the MFR technique explained previously, a special initial condition was implemented for the simulations to restrain undesirable overshooting of the velocity field caused by the retardment effect applied to the drop during the first iterative step. For this objective, the imposition of the potential flow around a cylinder was done to wrap the drop region so as to seem a drop encapsulated by a tube extending along the direction normal to the periodic one. Moreover, such flow tends to cause a slight disturbance on the drop due to the circulations that rise up behind the drop in the nearby wake region. Figure 54 depicts at the top three fluid layers passing around the drop on the planes $z = z_c$, $z = z_c + R + \delta z$ and $z = z_c - R - \delta z$, where R is the drop's radius and δz a small distance away from the poles; at the bottom is the top view of the flow on the symmetry plane $z = z_c$. When imposing such initial condition to the flow field, we intend to provoke a smooth transition from the initial departure of the drop toward its subsequent instants when it will experience the crossflow incidence. The periodicity is allotted to x-axis, whereas the crossflow condition is assigned to y-axis.

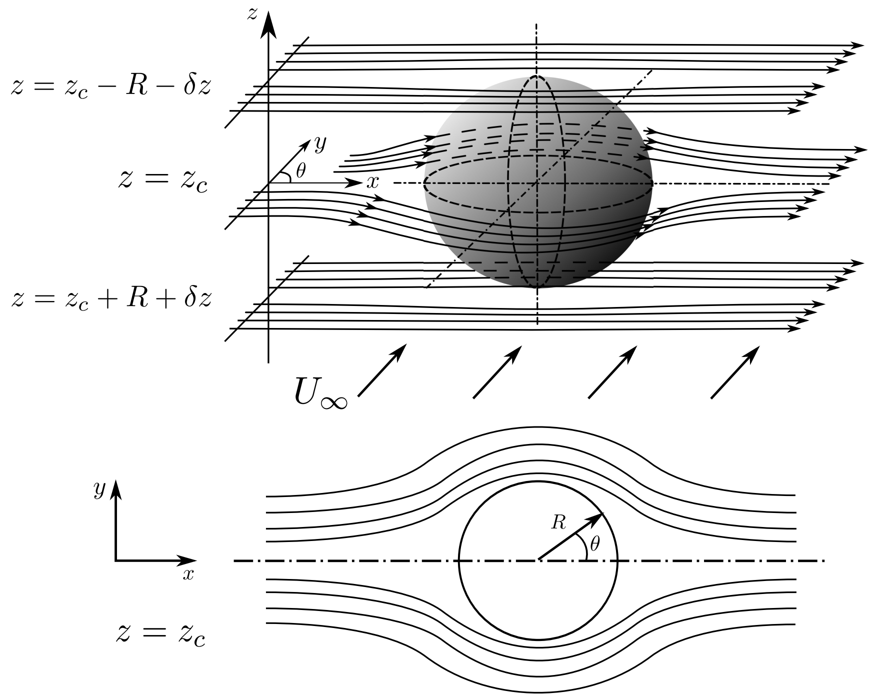

Figure 54: Past cylinder flow velocity profile as initial condition for the DJICF simulation.

The velocity profile of this condition is initialized over the computational mesh and written in cylindrical coordinates as

$$v_r = (U_j \cos(\theta) + U_\infty \sin(\theta)) \left[1 - \left(\frac{R}{r}\right)^2\right] + U_{added} \tag{7.9}$$

$$v_\theta = (-U_j \sin(\theta) + U_\infty \cos(\theta)) \left[1 + \left(\frac{R}{r}\right)^2\right] \tag{7.10}$$

$$v_z = 0, \tag{7.11}$$

thus using U_j and U_∞ as parameters.

At this point, it should be explained that $U_{added} = U_j$ is added to the original profile to compensate the difference which will be deduced of the flow immediately afterwards the simulation begin because of the MFR calculation (see the algorithm in Section 7.2) that retards the drop's motion.

7.3.2 Study of DJICF cases: hydrodynamics and discussion

Two different pairs of immiscible liquids relating to experiments performed, respectively, by Meister and Scheele [**?**] (also reproduced by [**?**]) for a water/n-heptane interface and by Webster and Longmire [**?**] (see p. 226) for a water-glycerin/Dow Corning sylicon-oil interface make up the next simulations, whose physical parameters are presented in Table 5 and Table 6. For convenience, the labels MS and WL will be used as abbreviations of the references cited above to designate the numerical tests. Additionally, two other parameters will determine the simulations, namely the ratio λ and the periodic cell's length L_P. Hence, the different configurations of tests chosen are expressed by a triple of parameters as

$$(Ref, \lambda, L_P), \quad \text{for} \quad Ref = \text{MS, WL}; \;\; \lambda = 1.0, 1.5, 2.0 \;\text{ and }\; L_P = 1.5, 3.0, 5.0. \qquad (7.12)$$

While different values of L_P seek to analyze the effect of the PBC by considering different spacing between drops (in the sense of the imposed periodicity), small values of λ seek to add a weak effect to the crossflow so as to ensure small disturbances in the surroundings of the drop and preserve the periodicity with less tendency to deflection. The cuboid-shaped meshes used in the simulations, which differ one another by the length L_P, are depicted in Figure 55 clipped along the axis of periodicity.

The analysis of the simulations starts from the velocity field $\mathbf{v}_{\mathrm{R}}(t) = (u_c, v_c, w_c)(t)$, whose component profiles are organized for each configuration from Figure 56 to Figure 61 as the ratio λ. By observing the curves of u_c and v_c, it is noticeable that u_c decays monotonically from $U_j = 1.0$ - the dimensionless jet velocity - at the initial instant to zero in the far-field

Data				
μ	ρ	D_j	Re	We
2.43	1.45	0.68	1851	2.20

Table 5: Parameters of simulation according to the experiment no. 5 of Meister and Scheele [**?**].

Data				
μ	ρ	Oh	Re	We^*
0.15	1.18	0.013	50	0.80

Table 6: Parameters of simulation according to the fluid combination no. 1(c) of natural jet of Webster and Longmire [?], p. 226. $^*We = (ReOh)^{0.5}$

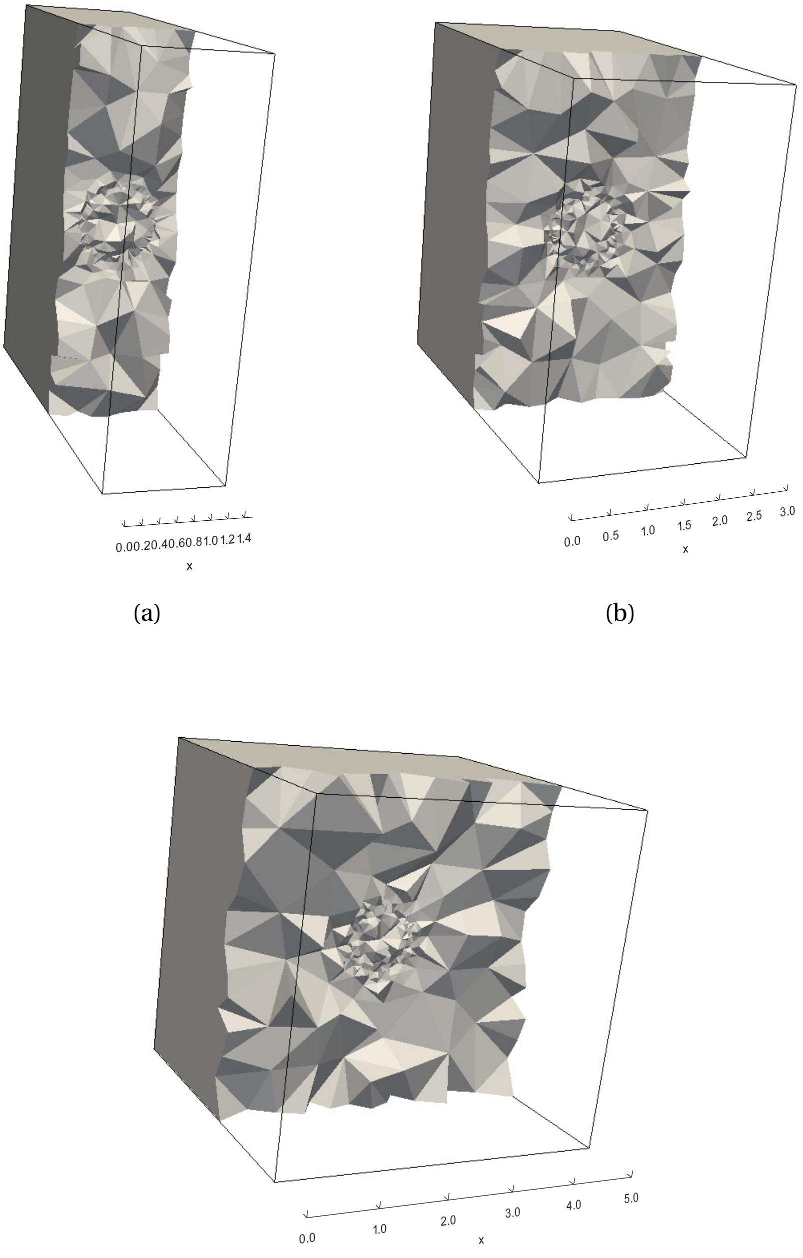

(a)

(b)

(c)

Figure 55: Meshes used for the DJICF simulations: (a) $L_P = 1.5$; (b) $L_P = 3.0$; (c) $L_P = 5.0$.

region, whereas v_c approaches asymptotically of $U_\infty = \lambda U_j$. It should be noted that the initial condition given by Equation (7.9) was essential to produce these profiles under a MFR scheme as aforementioned.

On one hand, the behaviour of w_c shows very small variations in comparison to the other profiles during the interval of simulation studied. Except for the cases with $L_P = 1.5$, w_c describes, at most, a slightly descending motion of the drop downward the crossflow plane, but without following a defined pattern. The highest values of w_c are observed in the cases $(MS,\cdot,\cdot)$, whose upper bounds are of $\mathcal{O}(10^{-2})$. On the other hand, the duration of decay of u_c as well as of rise of v_c up to their respective final values differ from case to case. Note, for example, how u_c and v_c reach their steady state within different times in the $(WL,\cdot,\cdot)$ group. Even more uncommon is the behaviour of u_c for $(WL,\cdot,1.5)$, which suggests an inflection of the drop's trajectory backward. Such a behaviour may be related to the influence of the flow nearby the drop which is more prominent due to the PBC and the smaller value of L_P. The simulations were stopped taking the profile v_c as reference, i.e. when the value of λ was achieved, since it reflects the drop's motion already dominated by the crossflow.

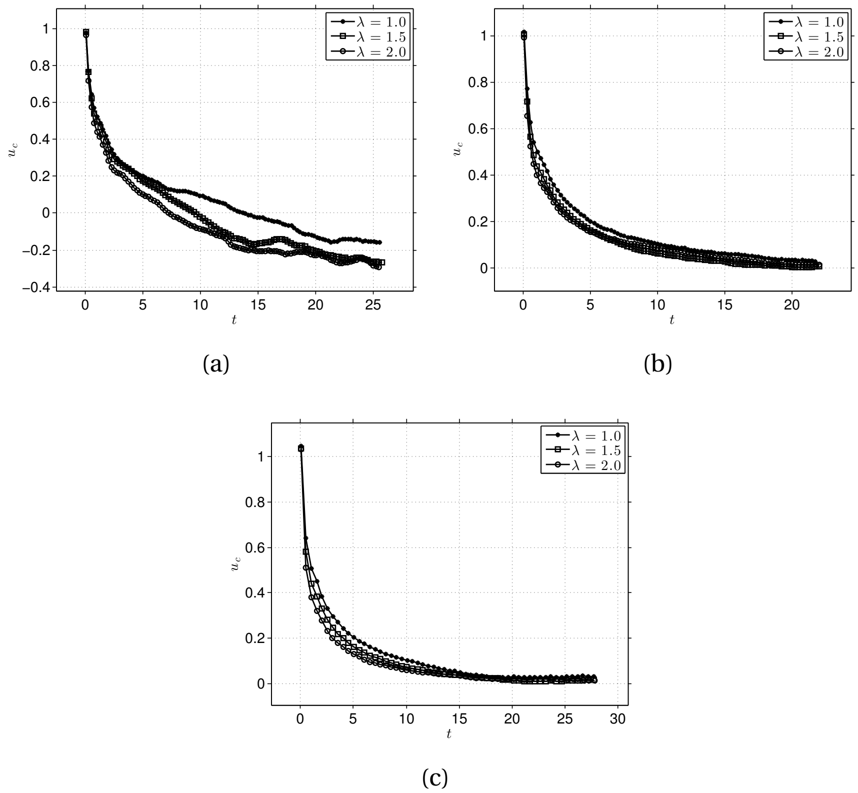

(a)

(b)

(c)

Figure 56: $u_c(t)$ profile - MS: (a) $(MS,\cdot,1.5)$; (b) $(MS,\cdot,3.0)$; (c) $(MS,\cdot,5.0)$.

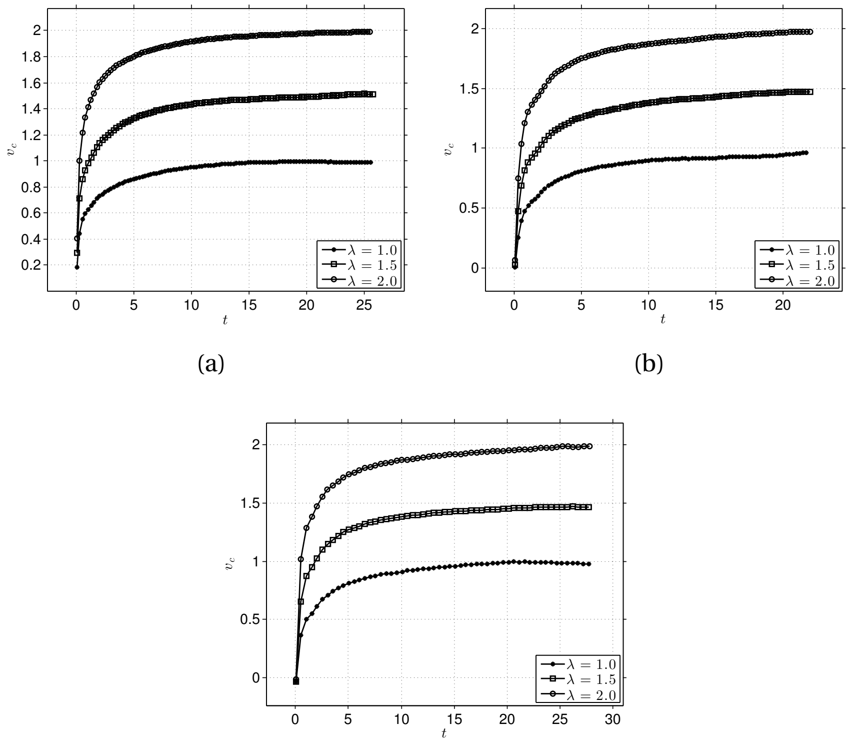

(a)

(b)

(c)

Figure 57: $v_c(t)$ profile - MS: (a) $(MS, \cdot, 1.5)$; (b) $(MS, \cdot, 3.0)$; (c) $(MS, \cdot, 5.0)$.

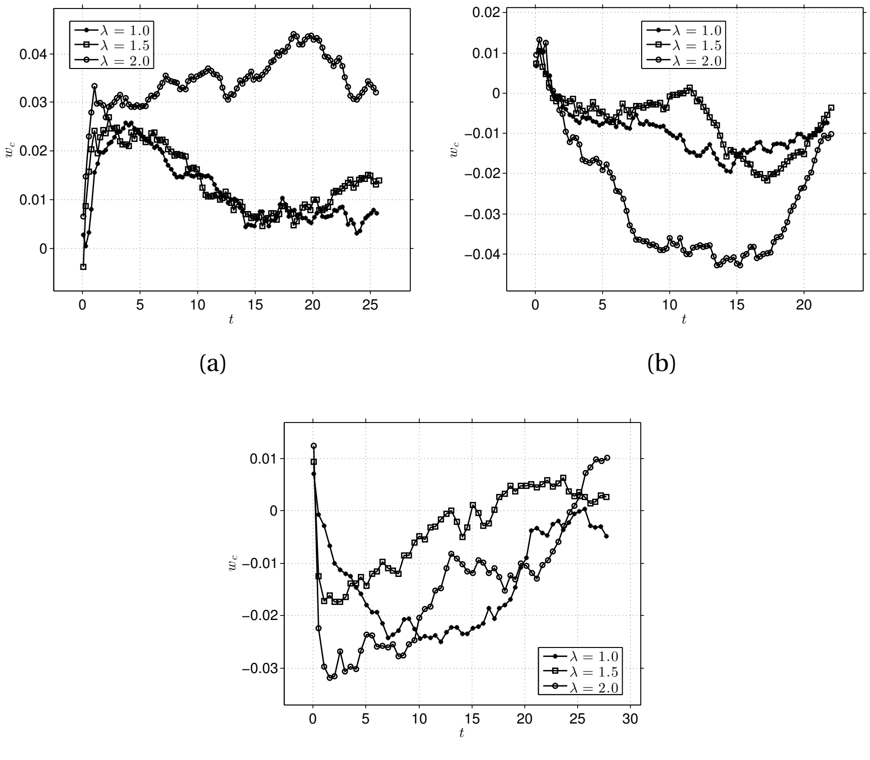

(a)

(b)

(c)

Figure 58: $w_c(t)$ profile - MS: (a) $(MS, \cdot, 1.5)$; (b) $(MS, \cdot, 3.0)$; (c) $(MS, \cdot, 5.0)$.

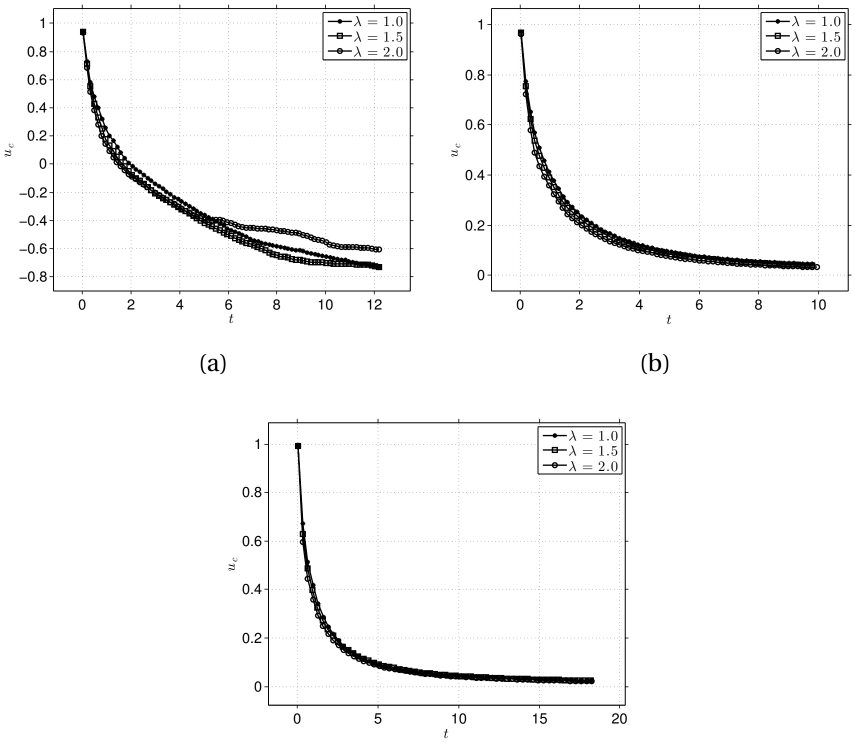

(a) (b)

(c)

Figure 59: $u_c(t)$ profile - WL: (a) $(WL, \cdot, 1.5)$; (b) $(WL, \cdot, 3.0)$; (c) $(WL, \cdot, 5.0)$.

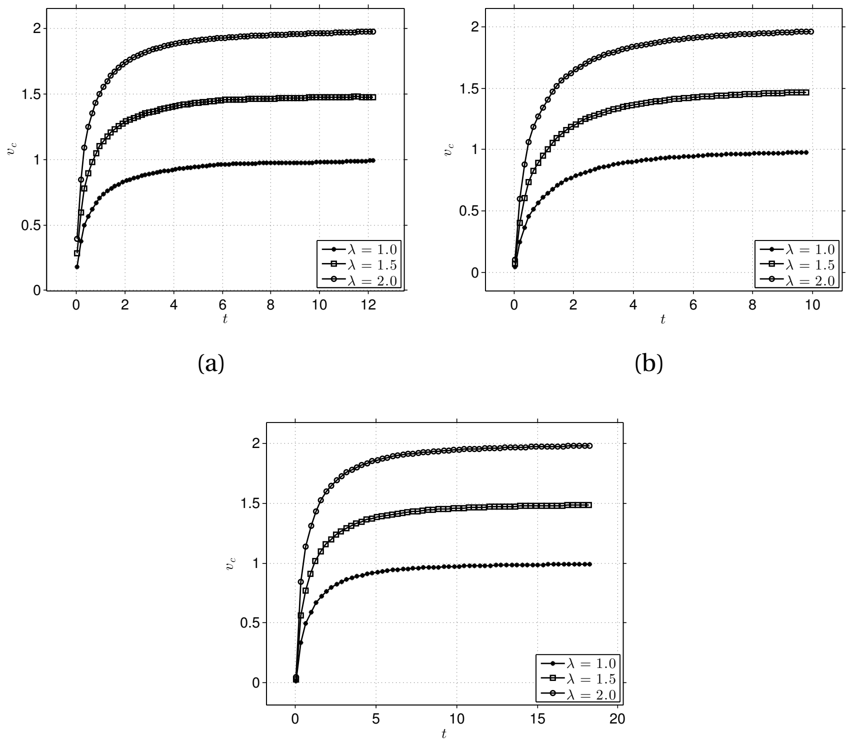

(a) (b)

(c)

Figure 60: $v_c(t)$ profile - WL: (a) $(WL, \cdot, 1.5)$; (b) $(WL, \cdot, 3.0)$; (c) $(WL, \cdot, 5.0)$.

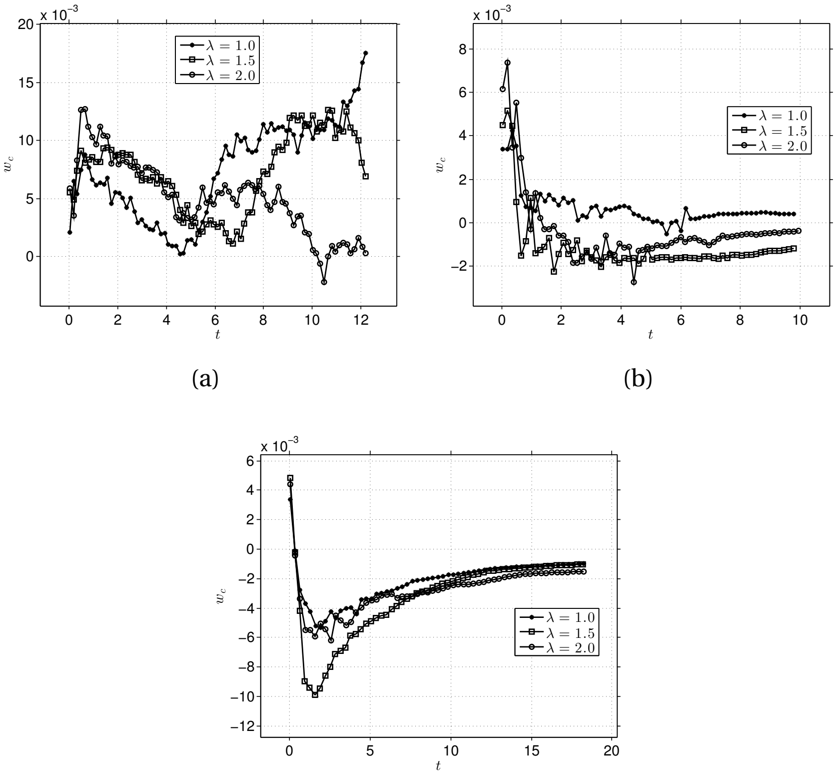

(a)

(b)

(c)

Figure 61: $w_c(t)$ profile - WL: (a) $(WL, \cdot, 1.5)$; (b) $(WL, \cdot, 3.0)$; (c) $(WL, \cdot, 5.0)$.

To illustrate the topological changes undergone by the drop in crossflow, some images containing streamlines and drop shape cuts obtained through the group of simulations $(\cdot, 2.0, \cdot)$ at specific times are depicted below. The streamlines are seen from behind the drop, encompassing it inside a box equivalent to half of the periodic cell cut by the symmetry plane tangent to the periodic direction. For each image of streamline are associated two others of symmetry planes that cross the drop surface along the regions xy and xz so as to characterize the drop's rims. Moreover, vectors of the relative velocity field $\mathbf{v}_{rel}$ were plotted over the rims to highlight its local effect over the drop. Though the family of tests WL showed moderate deformation, their related shapes were included here for completeness.

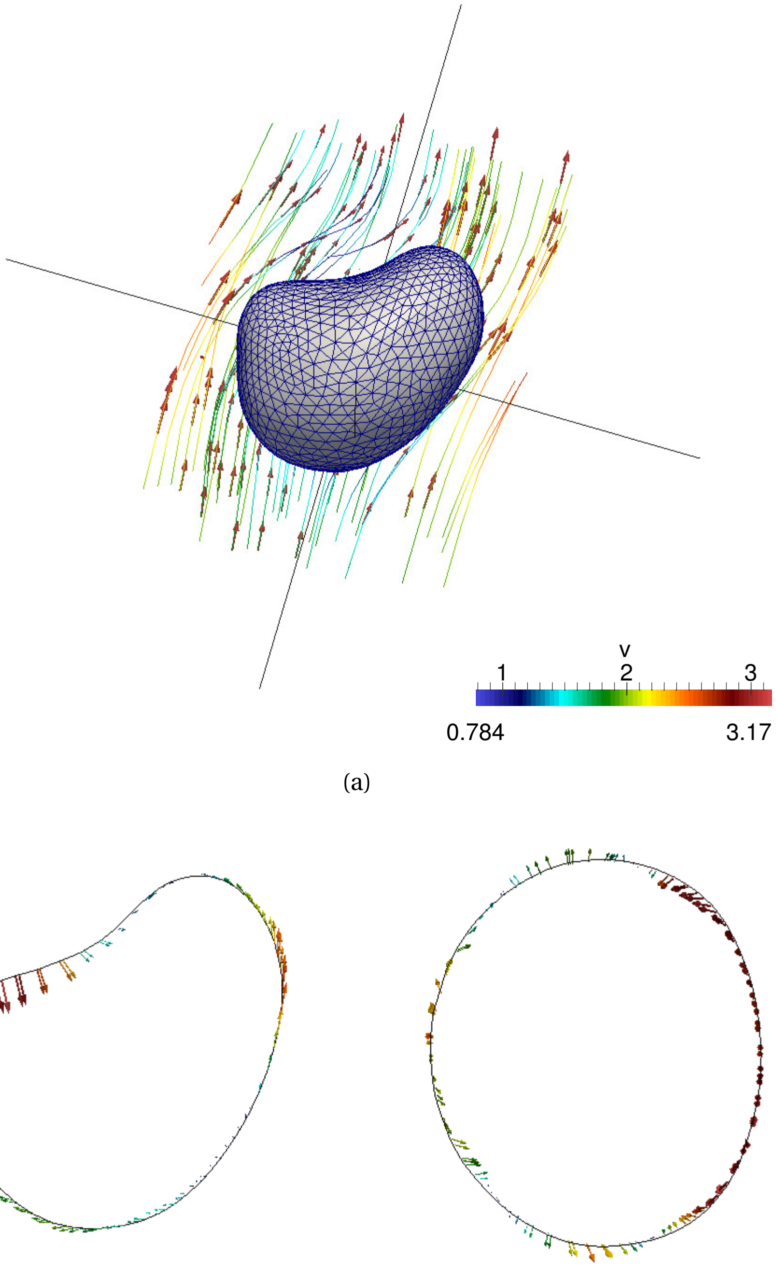

(a)

(b)

(c)

Figure 62: Streamlines and drop's rims at $t \approx 0.30$ - test $(MS, 2.0, 1.5)$: (a) streamlines and velocity field; (b) drop's rim on the plane xy; (c) drop's rim on the plane xz.

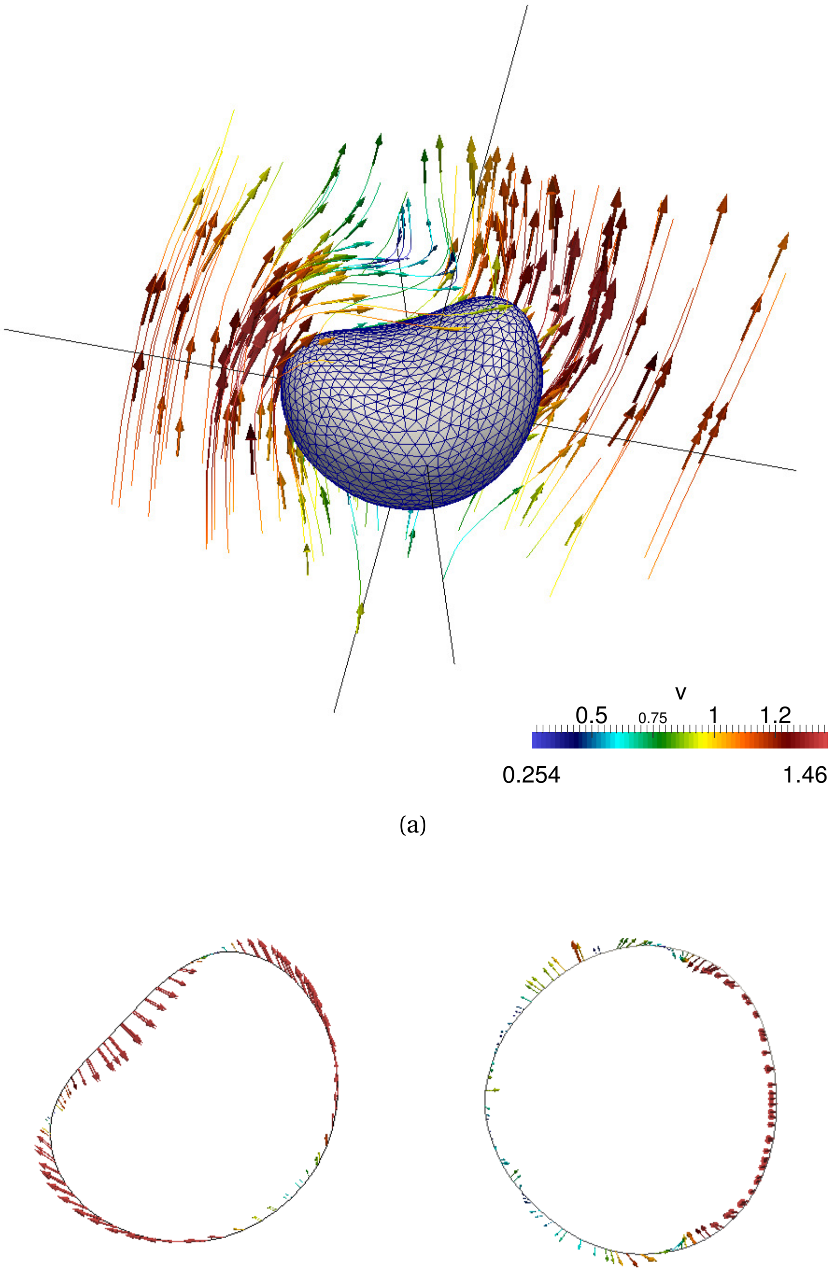

(a)

(b)

(c)

Figure 63: Streamlines and drop's rims at $t \approx 0.25$ - test $(MS, 2.0, 3.0)$: (a) streamlines and velocity field; (b) drop's rim on the plane xy; (c) drop's rim on the plane xz.

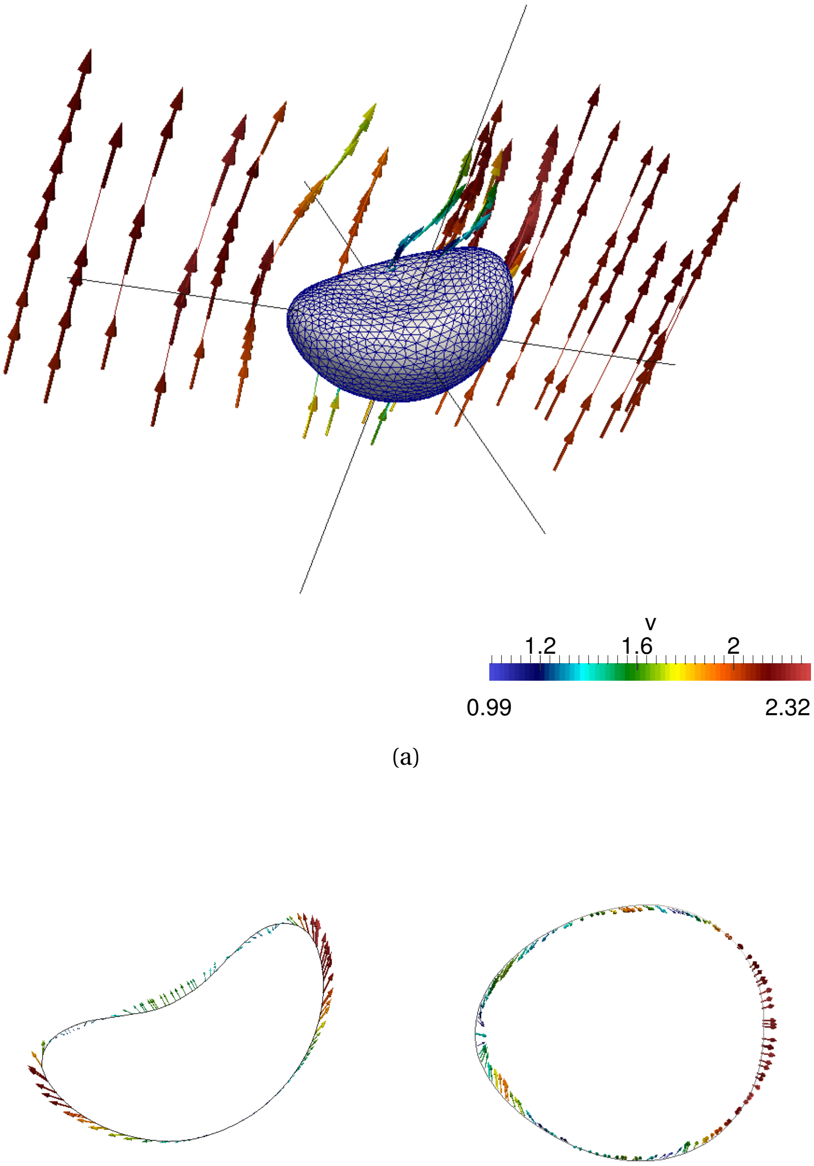

(a)

(b)

(c)

Figure 64: Streamlines and drop's rims at $t \approx 0.50$ - test $(MS, 2.0, 5.0)$: (a) streamlines and velocity field; (b) drop's rim on the plane xy; (c) drop's rim on the plane xz.

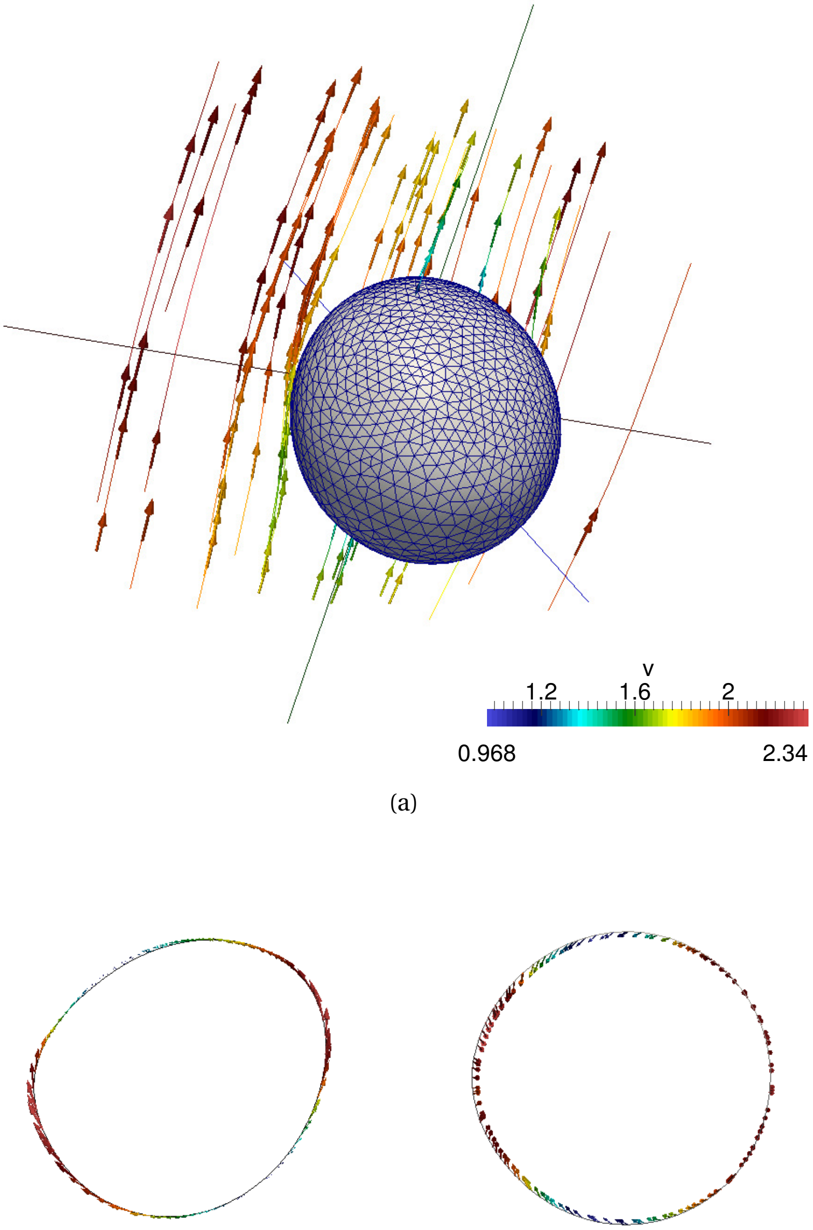

(a)

(b)

(c)

Figure 65: Streamlines and drop's rims at $t \approx 0.37$ - test $(WL, 2.0, 1.5)$: (a) streamlines and velocity field; (b) drop's rim on the plane xy; (c) drop's rim on the plane xz.

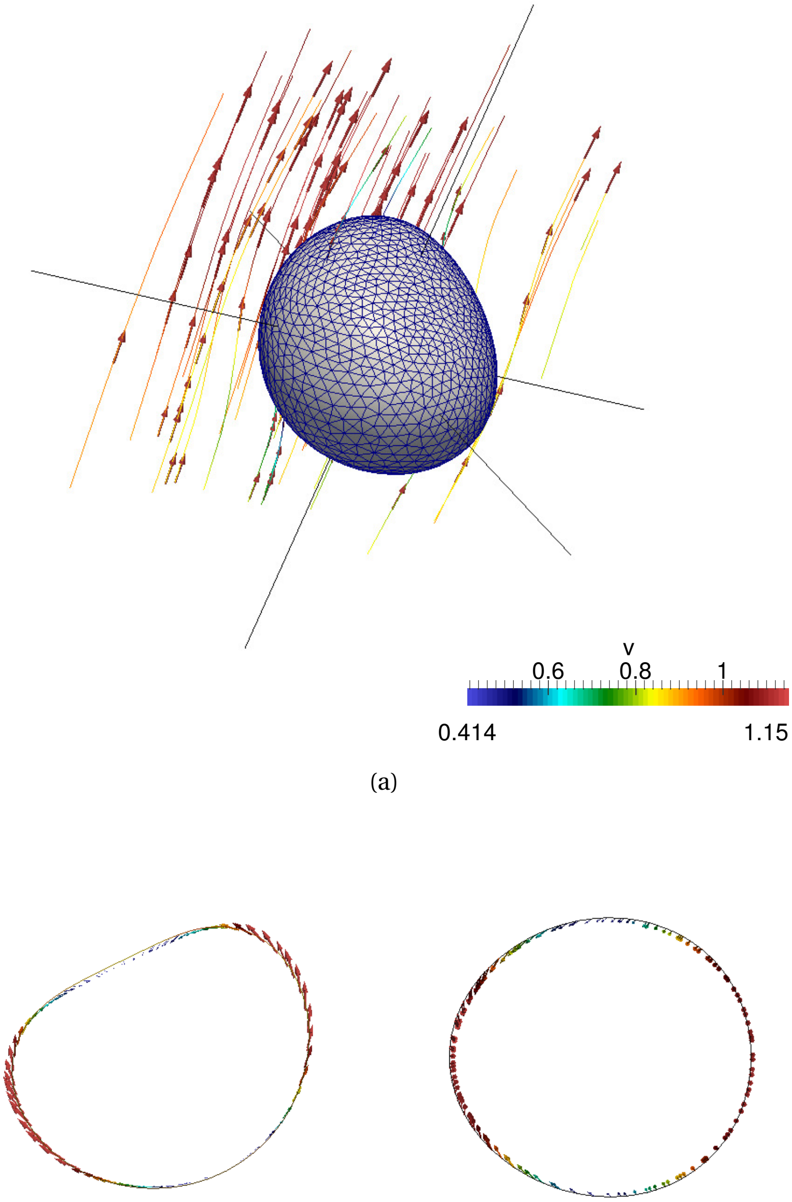

(a)

(b)

(c)

Figure 66: Streamlines and drop's rims at $t \approx 0.25$ - test $(WL, 2.0, 3.0)$: (a) streamlines and velocity field; (b) drop's rim on the plane xy; (c) drop's rim on the plane xz.

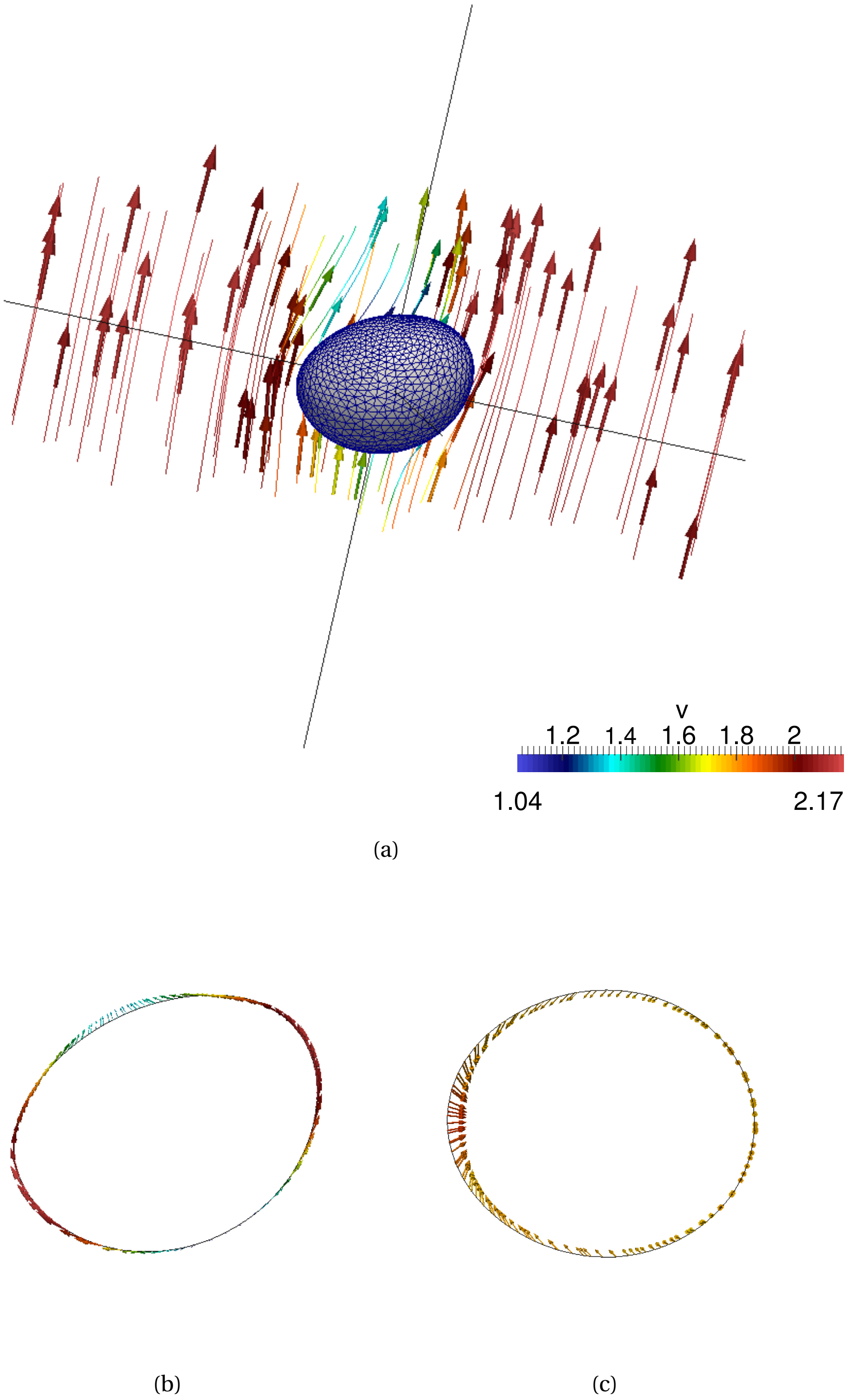

(a)

(b)

(c)

Figure 67: Streamlines and drop's rims at $t \approx 0.47$ - test $(WL, 2.0, 5.0)$: (a) streamlines and velocity field; (b) drop's rim on the plane xy; (c) drop's rim on the plane xz.

7.4 **Trajectory curves, drop shape variations and spectrum analyses**

7.4.1 Trajectory curves

The drop's behaviour concerning the trajectory that it experiences by incidence of the crossflow is represented by curves projected onto the planes xy and xz. The former class of projections display the deflection caused by the transverse flow; the latter class of projections display the deviation of the drop away from its center of mass' trajectory. Although the trajectory is a three-dimensional curve, spatial variations occurring along the direction normal to the uniform crossflow were found to be of a much smaller order than those due to the deflection. Trajectories for the pair labeled as MS are plotted in Figure 68 and Figure 69, while that Figure 70 and Figure 71 concern the pair labeled as WL. Given the small changes taking place on the plane xz, we will focus on analyzing the curves traced on the planes xy.

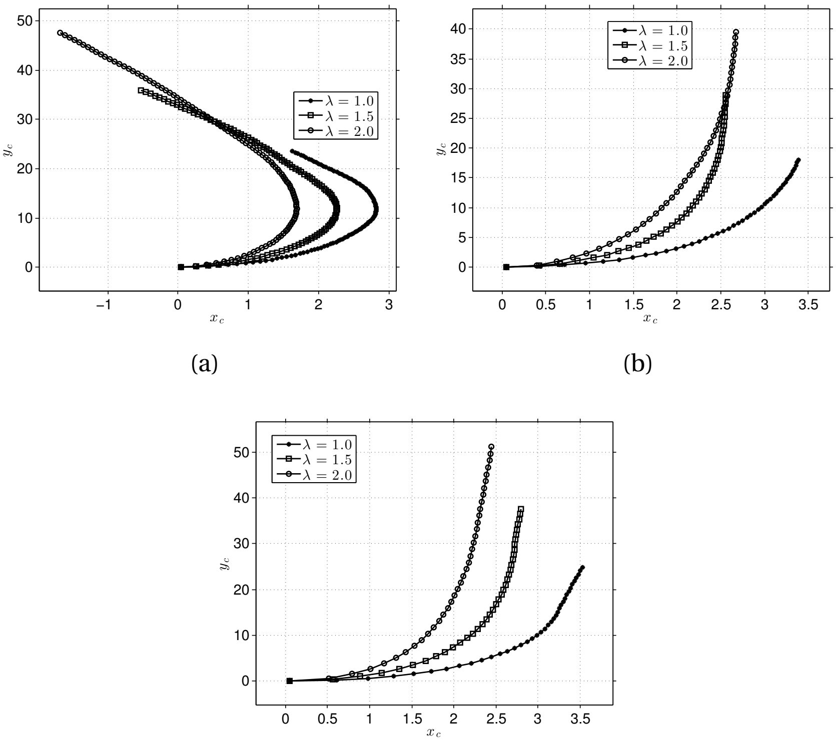

(a)

(b)

(c)

Figure 68: xy-plane drop trajectory - MS: (a) $(MS,\cdot,1.5)$; (b) $(MS,\cdot,3.0)$; (c) $(MS,\cdot,5.0)$.

As expected, the higher is the value of λ the broader is the deflection of the drop jet. This behaviour is consistent for almost all the cases simulated although the scale of displacement between the x and y directions varies from 1::14 to 1::17 in these cases, meaning that the crossflow dominance takes place quickly. The unique exceptions are the curves traced by the drop in the simulations of the group $(\cdot,\cdot,1.5)$ which, as mentioned in the previous subsection, suggest that the drop moves oppositely to its initial direction of launch.

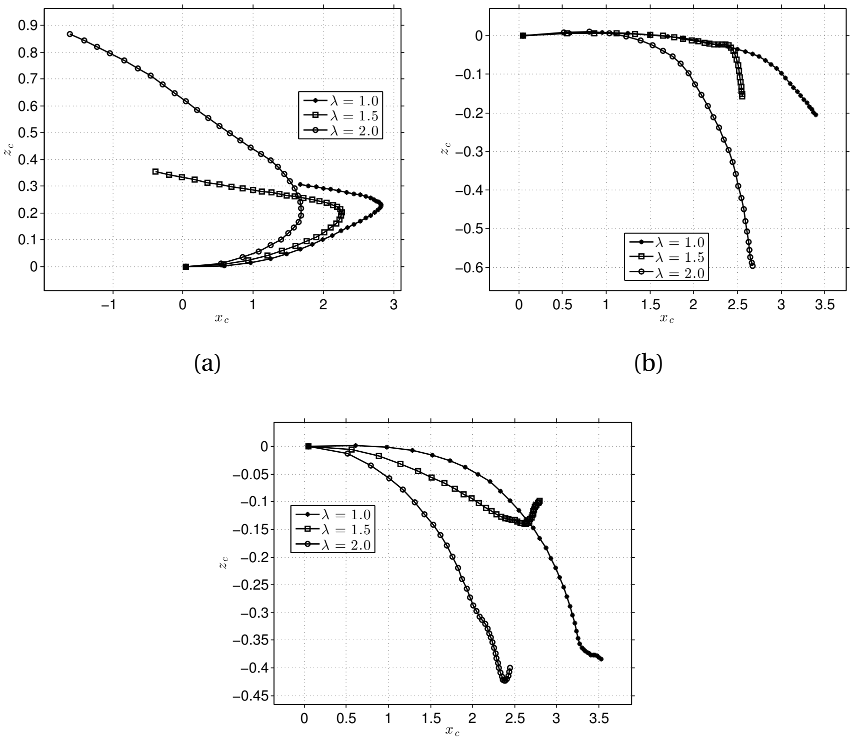

(a)

(b)

(c)

Figure 69: xz-plane drop trajectory - MS: (a) $(MS,\cdot,1.5)$; (b) $(MS,\cdot,3.0)$; (c) $(MS,\cdot,5.0)$.

The cases that describe the most uncommon behaviours are the ones of the family $(WL,\cdot,1.5)$, whose motion backward occurs in a scale 1::4. A possible explanation for this situation may be related to the effect of a L_P reduced and the consequences coming from the periodic gap among drops declared as follows: the drop jet is launched with velocity U_J; due to the constant crossflow, the profile imposed and the momentum exchange, the drop loses velocity and deforms; the drop's deformation at the initial instants is caused by marked flatness that forms a wider surface area which, in turn, eases the crossflow actuation; finally, the crossflow pushes the drop backward. Such a description is coherent with the profile of $\phi(t)$ for $L_P = 1.5$ depicted in Figure 73. It is possible observe that the flatness curve increases to values above 1.0 for $(WL,\cdot,1.5)$, whereas decreases to values below 1.0 for these cases at the initial stages of motion, thus suggesting that a "lift" is produced. Furthermore, when comparing the profiles of elongation and flatness for the families $L_P = 1.5$ to their respective profiles for $L_P = 3.0, 5.0$, we note that similar effects happen.

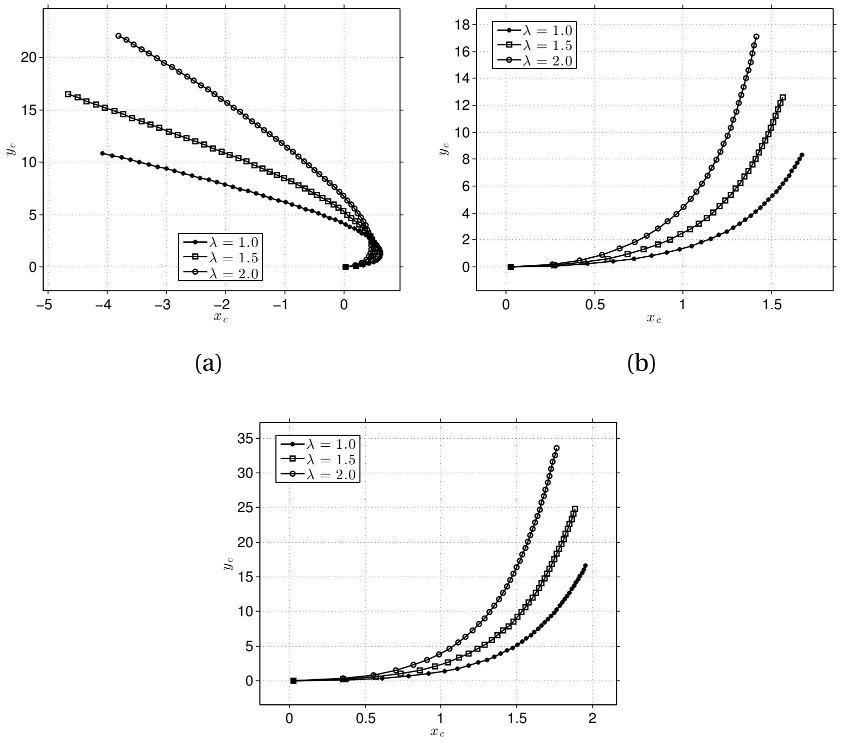

(a) (b)

(c)

Figure 70: xy-plane drop trajectory - WL: (a) $(WL,\cdot,1.5)$; (b) $(WL,\cdot,3.0)$; (c) $(WL,\cdot,5.0)$.

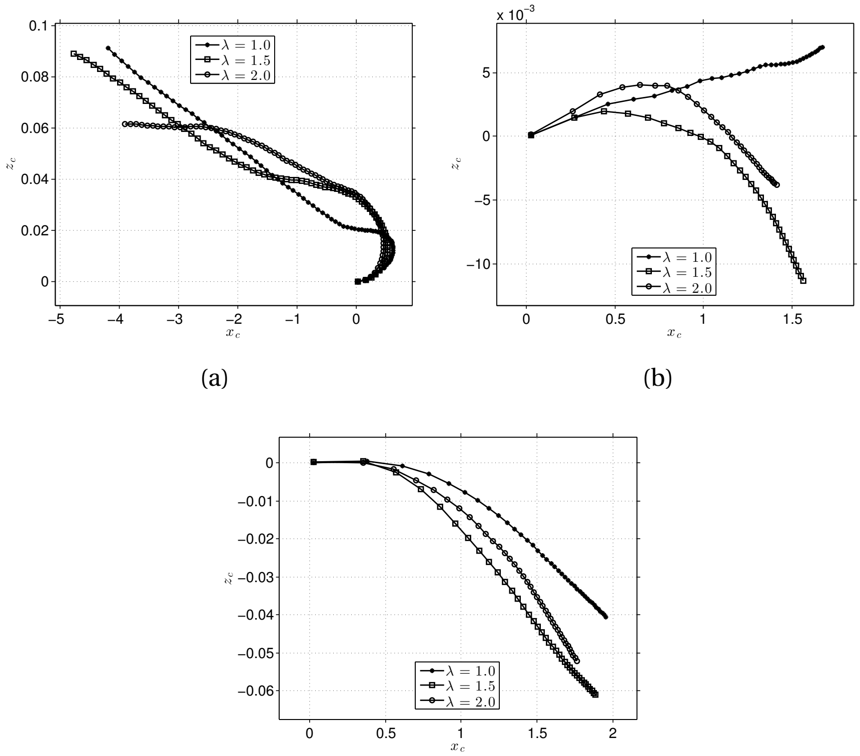

(a) (b)

(c)

Figure 71: xz-plane drop trajectory - WL: (a) $(WL,\cdot,1.5)$; (b) $(WL,\cdot,3.0)$; (c) $(WL,\cdot,5.0)$.

7.4.2 Drop shape variations

To analyze the shape assumed by the drop in the flow considered here, the expressions of aspect ratio for elongation and flatness are revisited from their definition in Equation (6.13), i.e.

$$\phi = \frac{b}{c}; \quad \psi = \frac{c}{a}, \tag{7.13}$$

for the principal axes a, b, c. The curves of $\phi(t)_\lambda$ and $\psi(t)_\lambda$ are sketched below for each simulation, by gathering the three different values of the ratio λ and of the length L_P per plot. The general behaviour for the curves is described by a region of oscillation, when the drop deforms by action of the crossflow, followed by another of damping, when the drop travels steadily. A specific feature that differ the profiles of the family MS from the family WL is the time interval in which some deformation still is evident, which extends up to around $t \approx 4.5$ for WL and up to $t \approx 20.0$ for MS. Arguments for having a much larger interval with predominance of deformation for the MS cases rely on the different physical properties of the flows, mainly on the value of the We number which, being smaller, indicates that the forces due to the surface tension dominate over the inertial forces as well as that the drop is less tolerant to deformation. In this comparison, a caveat should be raised for the cases $L_P = 1.5$, that show some level of noise and out-of-phase oscillation for different values of λ, besides being unclear to describe.

Another point to consider about the curves of $\phi(t)_\lambda$ and $\psi(t)_\lambda$ concern their amplitude. It is seen that, for all the cases simulated, the maximum and minimum values of flatness are, respectively, higher and lower than elongation's, thus suggesting that there are more shapes with wider surface area projected perpendicularly to the crossflow direction. It one concludes, additionally, that the variation of λ causes shape deformations very similar to the drop, with localized discrepancies of phase occurring within the interval $[0.0, t \approx 2.0]$.

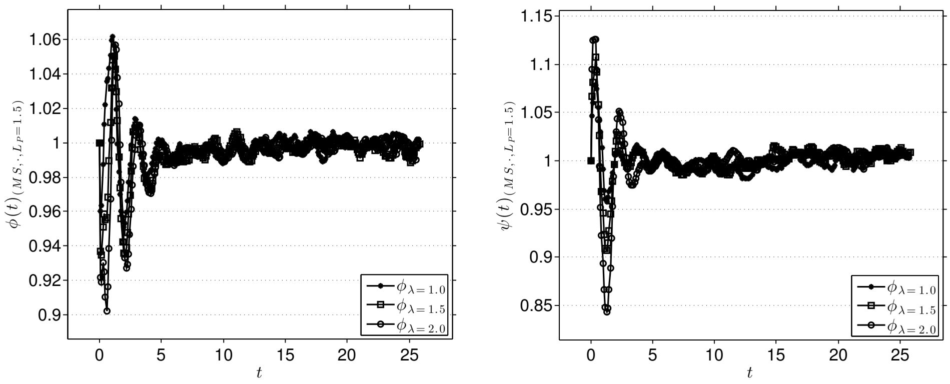

(a)

(b)

Figure 72: Drop shape variation - $(MS,\cdot,1.5)$: (a) $\phi(t)$; (b) $\psi(t)$.

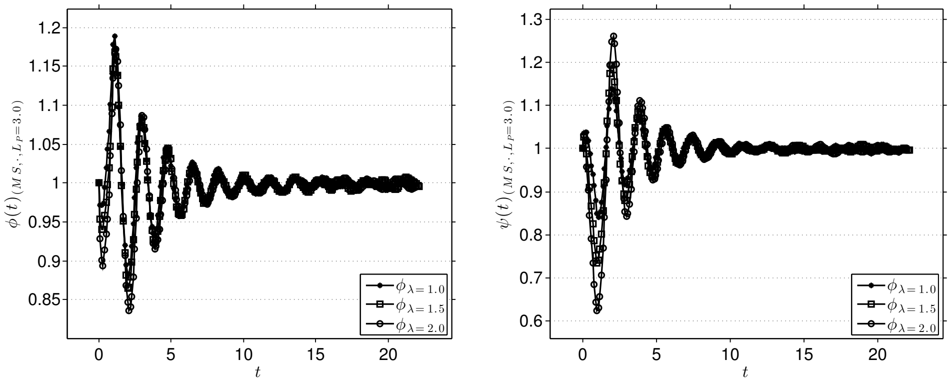

(a)

(b)

Figure 73: Drop shape variation - $(MS,\cdot,3.0)$: (a) $\phi(t)$; (b) $\psi(t)$.

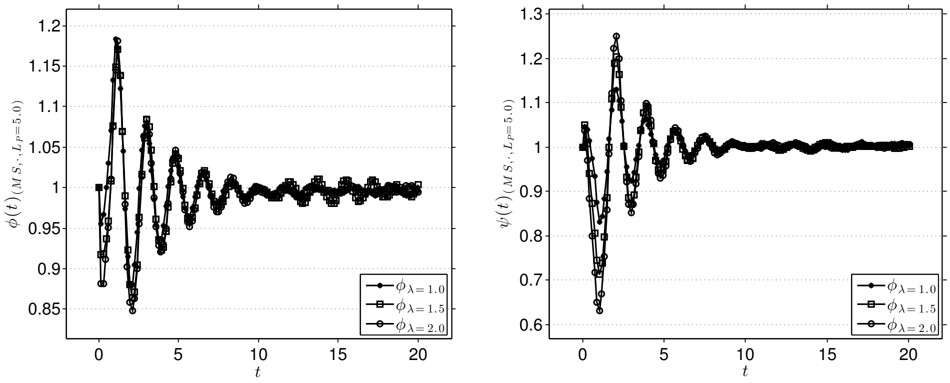

(a)

(b)

Figure 74: Drop shape variation - $(MS,\cdot,5.0)$: (a) $\phi(t)$; (b) $\psi(t)$.

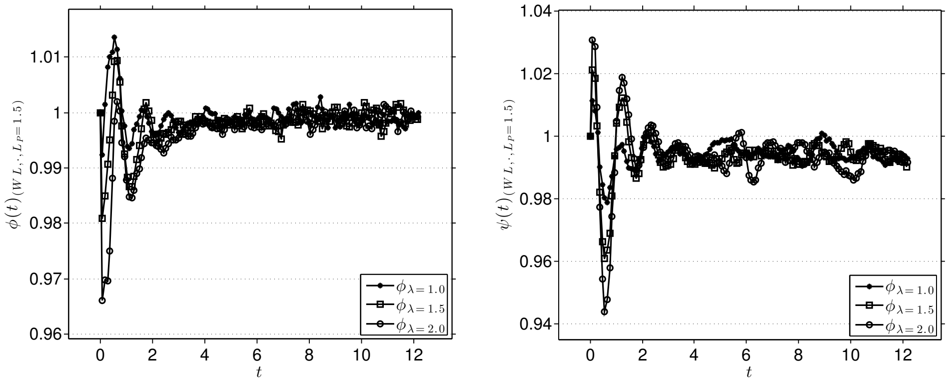

(a)

(b)

Figure 75: Drop shape variation - $(WL, \cdot, 1.5)$: (a) $\phi(t)$; (b) $\psi(t)$.

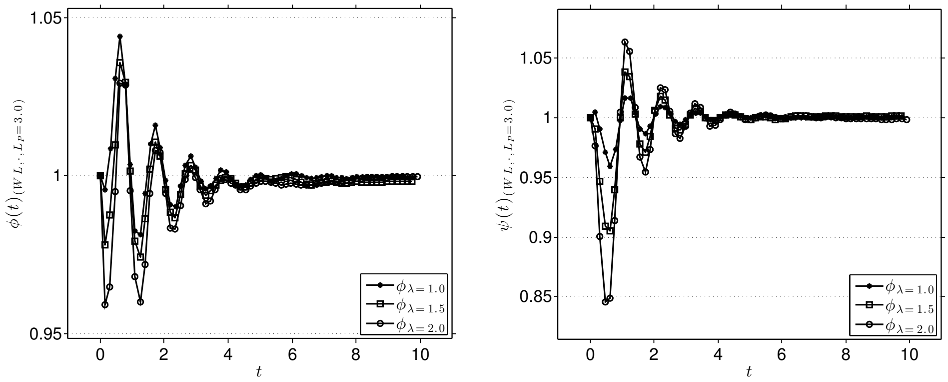

(a)

(b)

Figure 76: Drop shape variation - $(WL, \cdot, 3.0)$: (a) $\phi(t)$; (b) $\psi(t)$.

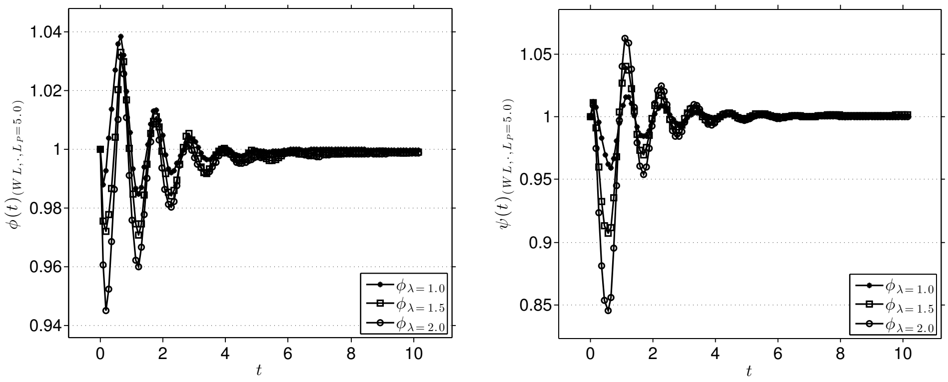

(a)

(b)

Figure 77: Drop shape variation - $(WL, \cdot, 5.0)$: (a) $\phi(t)$; (b) $\psi(t)$.

7.4.3 Spectrum analyses

From this point on, spectrum analyses for the DJICF configurations studied are presented. The input signals for the FFT calculation correspond to the curves $\phi(t)_\lambda$ and $\psi(t)_\lambda$, which evince disturbances affecting the drop. FFT-based spectra for elongation and flatness are plotted in the figures below separated according to the values of λ. Inasmuch as the spectrum of magnitude of such a disturbances is expressed as given by Equation (6.14), it is convenient to introduce in the following discussion the values given by

$$\mathsf{E}_{\phi_\lambda} = \max\{|FFT[\phi(t)_\lambda]|\} \quad \text{and} \quad \mathsf{E}_{\psi_\lambda} = \max\{|FFT[\psi(t)_\lambda]|\}, \tag{7.14}$$

which represent, respectively, the maximum disturbance energy achieved with the slight wobbling of the drop relative to the profiles of elongation and flatness, whereas

$$f^*_\phi \quad \text{and} \quad f^*_\psi \tag{7.15}$$

are dimensionless vibration frequencies (or harmonic modes) associated to each of these profiles within a sampling range t_S. The choice of t_S, however, was done by truncating the whole time of the simulations into the regions where the small disturbances were more active, thus restraining the interval of analysis. Besides, only the 10 first modes are plotted for each simulation. Spectra for the group MS are plotted from Figure 78 followed by spectra for the group WL plotted from Figure 81.

Table 7 lists the maximum energy values along with their respective most amplified modes associated to $\phi(t)_\lambda$ and $\psi(t)_\lambda$ for the testing configurations (Ref, λ, L_P). Furthermore, note that

$$\mathsf{E}_{F(t)} = \max\left\{\left(\Re\{FFT[F(t)]\}^2 + \Im\{FFT[F(t)]\}^2\right)^{0.5}\right\}, \quad F(t) = \phi(t)_\lambda, \psi(t)_\lambda \tag{7.16}$$

evokes the maximum value in modulus of complex modes associated to the shape ratios.

A point to be emphasized is that the output of $FFT[F(t)]$ requires that the sampling time range t_S be uniform. Since the selection of the time step Δt may be different for each simulation and vary after remeshing operations (cf. Sec. 5.1 of [**?**]), t_S must be modified so

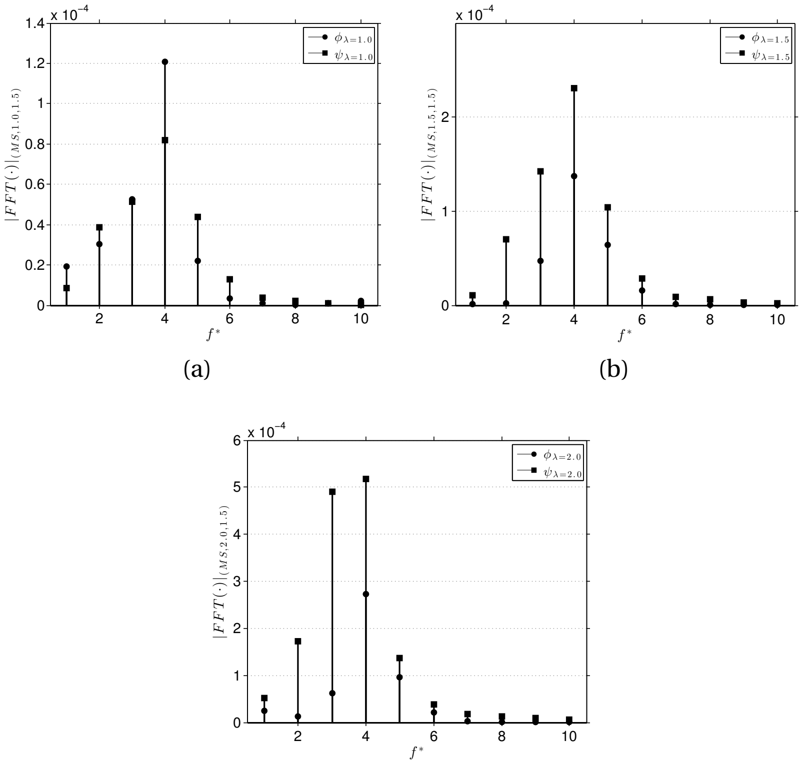

(a) (b)

(c)

Figure 78: FFT-based spectrum: (a) $(MS, 1.0, 1.5)$; (b) $(MS, 1.5, 1.5)$; (c) $(MS, 2.0, 1.5)$.

that this uniformity be ensured. For that objective, the average time step

$$\overline{\Delta t} = \frac{(\Delta t)_n}{N} = \frac{(t^{n+1} - t^n)}{N}; \quad n = 0, 1, \ldots N-1 \tag{7.17}$$

and the function `interp1` from MATLAB® were used to build a new discrete vector t_S equally spaced from the original one. The sampling ranges specified for each case as well as the approximated thresholds from which the disturbances are attenuated are organized in Table 8.

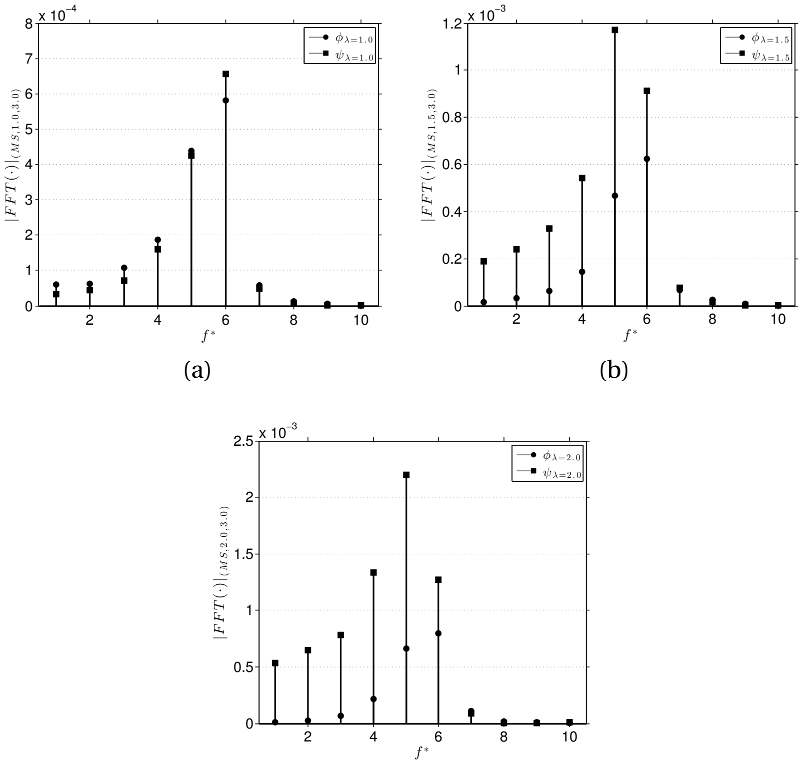

(a)

(b)

(c)

Figure 79: FFT-based spectrum: (a) $(MS, 1.0, 3.0)$; (b) $(MS, 1.5, 3.0)$; (c) $(MS, 2.0, 3.0)$.

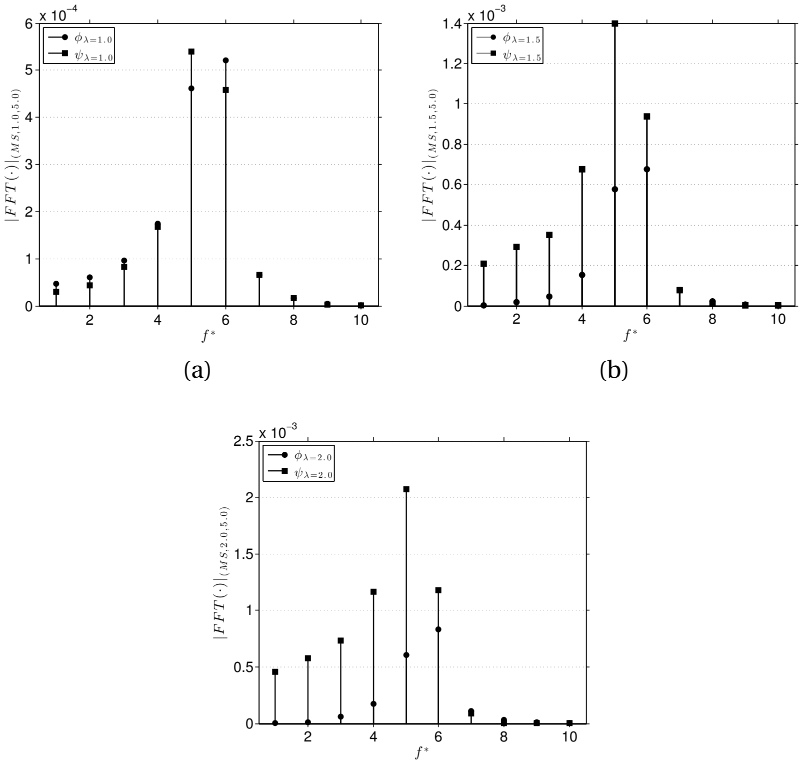

(a)

(b)

(c)

Figure 80: FFT-based spectrum: (a) $(MS, 1.0, 5.0)$; (b) $(MS, 1.5, 5.0)$; (c) $(MS, 2.0, 5.0)$.

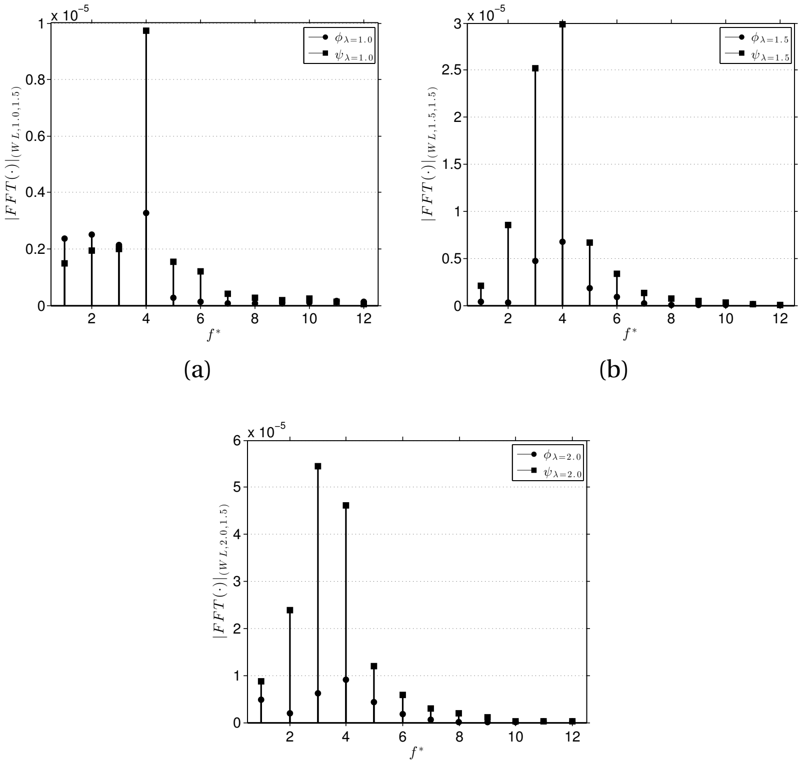

(a)

(b)

(c)

Figure 81: FFT-based spectrum: (a) $(WL, 1.0, 1.5)$; (b) $(WL, 1.5, 1.5)$; (c) $(WL, 2.0, 1.5)$.

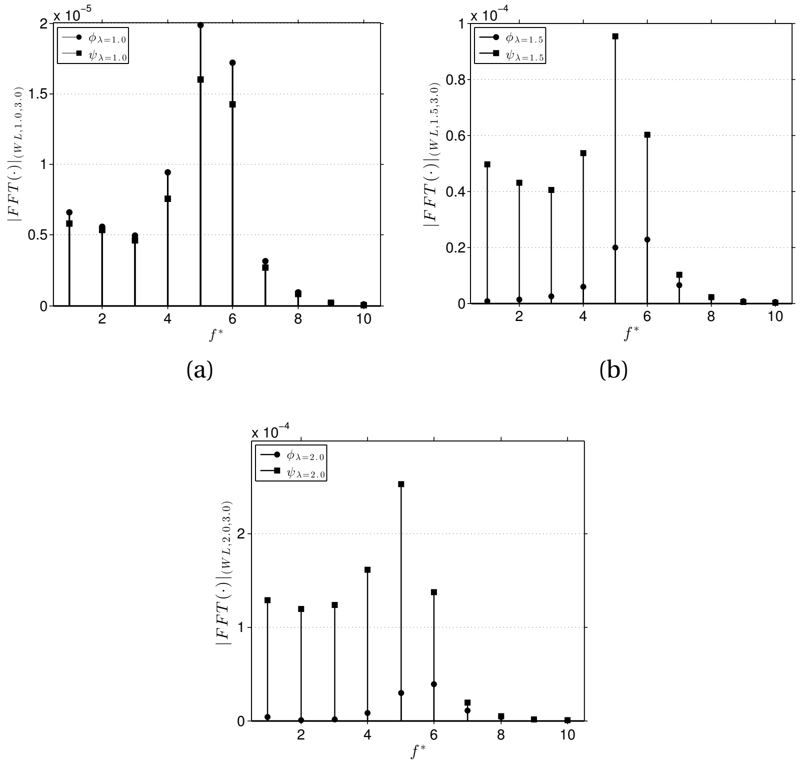

(a)

(b)

(c)

Figure 82: FFT-based spectrum: (a) $(WL, 1.0, 3.0)$; (b) $(WL, 1.5, 3.0)$; (c) $(WL, 2.0, 3.0)$.

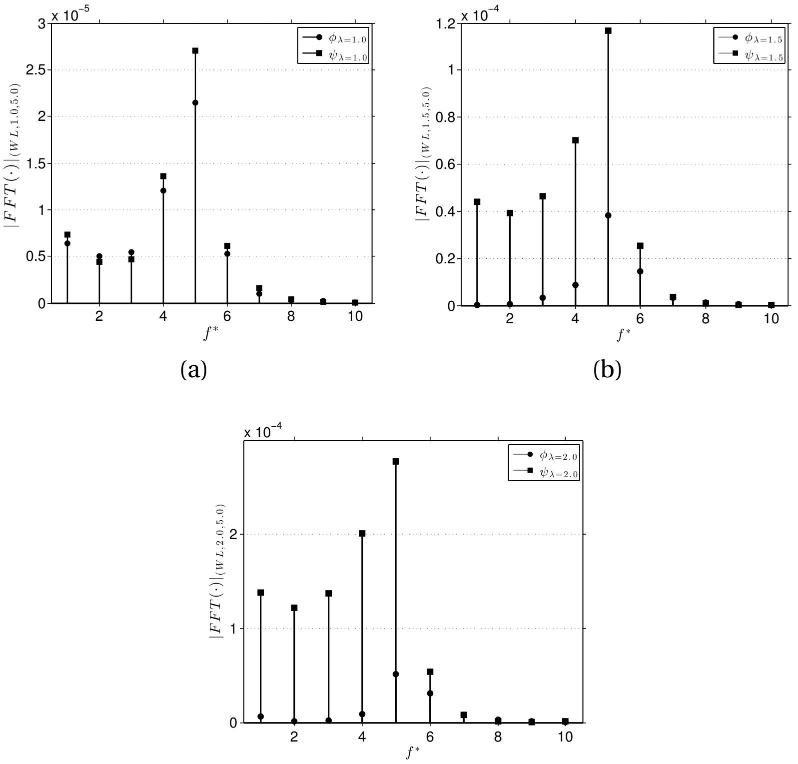

(a)

(b)

(c)

Figure 83: FFT-based spectrum: (a) $(WL, 1.0, 5.0)$; (b) $(WL, 1.5, 5.0)$; (c) $(WL, 2.0, 5.0)$.

Test Configuration	Elongation: ϕ		Flatness: ψ	
(Ref, λ, L_P)	E_{ϕ}	f^*_{ϕ}	E_{ψ}	f^*_{ψ}
$(MS, 1.0, 1.5)$	0.1209e-03	4	0.8209e-04	4
$(MS, 1.5, 1.5)$	0.1371e-03	4	0.2307e-03	4
$(MS, 2.0, 1.5)$	0.2724e-03	4	0.5173e-03	4
$(MS, 1.0, 3.0)$	0.5823e-03	6	0.6555e-03	6
$(MS, 1.5, 3.0)$	0.6240e-03	6	1.2000e-03	5
$(MS, 2.0, 3.0)$	0.7976e-03	6	2.2000e-03	5
$(MS, 1.0, 5.0)$	0.5204e-03	6	0.5398e-03	5
$(MS, 1.5, 5.0)$	0.6744e-03	6	1.4000e-03	5
$(MS, 2.0, 5.0)$	0.8320e-03	6	2.1000e-03	5
$(WL, 1.0, 1.5)$	0.3273e-05	4	0.9720e-05	4
$(WL, 1.5, 1.5)$	0.6780e-05	4	2.9883e-05	4
$(WL, 2.0, 1.5)$	0.9122e-05	4	5.4396e-05	3
$(WL, 1.0, 3.0)$	1.9835e-05	5	1.5984e-05	5
$(WL, 1.5, 3.0)$	0.2279e-04	6	0.9535e-04	5
$(WL, 2.0, 3.0)$	0.3907e-04	6	2.5348e-04	5
$(WL, 1.0, 5.0)$	2.1435e-05	5	2.7042e-05	5
$(WL, 1.5, 5.0)$	0.3822e-04	5	1.1677e-04	5
$(WL, 2.0, 5.0)$	0.5176e-04	5	2.7757e-04	5

Table 7: Maximum disturbance energies and dominant modes of the spectral analyses.

Test Configuration (Ref, λ, L_P)	Sampling Range t_S	Threshold $t \approx$
$(MS, 1.0, 1.5)$	7.5	20.0
$(MS, 1.5, 1.5)$	7.5	20.0
$(MS, 2.0, 1.5)$	7.5	20.0
$(MS, 1.0, 3.0)$	10.0	20.0
$(MS, 1.5, 3.0)$	10.0	20.0
$(MS, 2.0, 3.0)$	10.0	20.0
$(MS, 1.0, 5.0)$	10.0	20.0
$(MS, 1.5, 5.0)$	10.0	20.0
$(MS, 2.0, 5.0)$	10.0	20.0
$(WL, 1.0, 1.5)$	4.0	12.0
$(WL, 1.5, 1.5)$	4.0	12.0
$(WL, 2.0, 1.5)$	4.0	12.0
$(WL, 1.0, 3.0)$	6.0	10.0
$(WL, 1.5, 3.0)$	6.0	10.0
$(WL, 2.0, 3.0)$	6.0	10.0
$(WL, 1.0, 5.0)$	5.5	10.0
$(WL, 1.5, 5.0)$	5.5	10.0
$(WL, 2.0, 5.0)$	5.5	10.0

Table 8: FFT sampling ranges and disturbance attenuation thresholds for the spectral analyses.

7.5 Mesh quality assessment

High-quality meshes are fundamental to produce accurate results. The poorer the mesh elements are generated, the poorer the solution is computed. Bad elements are those whose shape present certain disproportionalities or degeneracies which affect directly the results since they magnify a series of problems regarding conditioning, discretization and interpolation, for example.

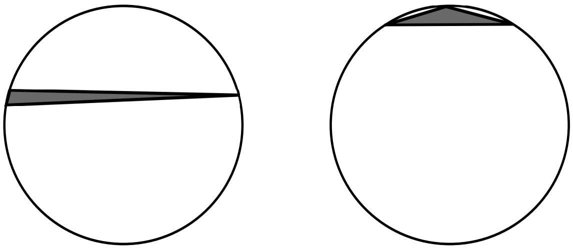

Figure 84: Examples of skinny triangular elements: needle, at left; cap, at right.

According to the literature concerned with mesh generation, such a elements are called *skinny* elements. Some classes of bad-quality triangles and tetrahedra are depicted in Figure 84 and Figure 85, adapted from [**?**]. *Needle* elements have disparate edge lengths; *cap* elements either have an angle near 180° (a triangle) or a large solid angle (tetrahedron); *sliver* tetrahedra have very small circumradius-to-shortest edges ratio, but bad dihedrals. Preventing the existence of these elements while creating a mesh is one of the big challenges of a good mesh generator; so is developing robust dynamic meshing operations.

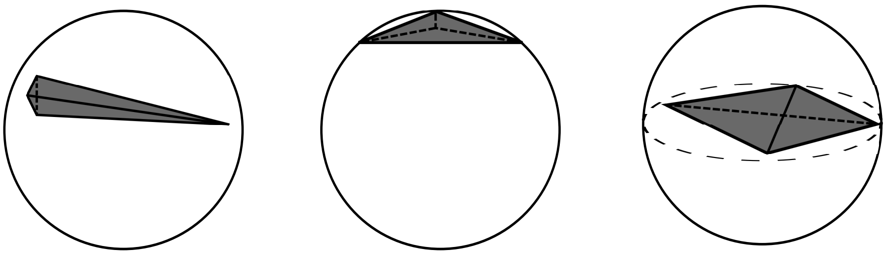

Figure 85: Examples of skinny tetrahedral elements: needle, at left; cap, at center; sliver, at right.

In order to verify the effectiveness of the dynamic meshing provided by the ALE/FE methodology used in this thesis such as reported in Section 4.4, the mesh quality of the simulations was assessed using a quality measure relative to the *ratio radius* of tetrahedra, which reads as

$$\mathscr{I}_{tet}(t) = \left[\frac{R_{out}(t)}{3R_{in}(t)} \right]_{tet}, \tag{7.18}$$

with R_{in} (R_{out}) being the inradius (circumradius) of a tetrahedral element. The data analysis is plotted in the form of histograms ($\mathscr{I}_{tet}(t) \times A$), where A is the number of mesh elements relative to the index $\mathscr{I}_{tet}$. That is to say, the better is the quality of an element the closer is $\mathscr{I}_{tet}$ to 1.0 for this element. Note, furthermore, that $\mathscr{I}_{tet}$ depends on time due to the arbitrary mesh motion and consequent change of the inradius and circumradius. However, provided that the mesh parameters are combined to produce good aspect ratios as well as fair point distributions as Equation (4.38) rules, it is expected that R_{in} and R_{out} do not vary overly with time.

As will be seen through the histograms plotted below, an overall quality measure will be given for the volume mesh. Since higher densities of $\mathscr{I}_{tet}(t)$ are concentrated by far in the major part of the mesh elements, poor elements are almost absent in the simulations. This observation ensures not only the quality of the method itself, but also of the mesh generator. In the next subsections, the histograms of $\mathscr{I}_{tri}(t)$ are displayed before those of $\mathscr{I}_{tet}(t)$ for the MS and WL experimental conditions simulated. The behaviour of the histograms is very similar for all the cases simulated. For this reason, only a few chosen arbitrarily were considered.

The histograms gather data relative to the time instant when the insertion rate due to the dynamical meshing returns the highest amount of elements whose quality is maximum. Besides, the percentage of quality for this specific instant was computed so as to give the maximum order of quality attained in the associated simulation. Table 9 lists the information relative to the mesh quality assessment: t_A is the time when the mesh reaches the maximum number of tetrahedra; $A_{\mathscr{I}}^{max}$ is the number of tetrahedra with the highest quality and $\mathscr{O}_{\%}$ is the percentage of elements whose $\mathscr{I}_{tet}$ is maximum in relation to the total mesh elements at t_A. The latter value emphasizes, additionally, the order of quality of the related test. It turns out, therefore, that the high values presented - above 90 % for all the cases except for $(MS, 1.5, 3.0)$ - in the last column allow us to assert that the ALE/FE methodology applied is enough robust.

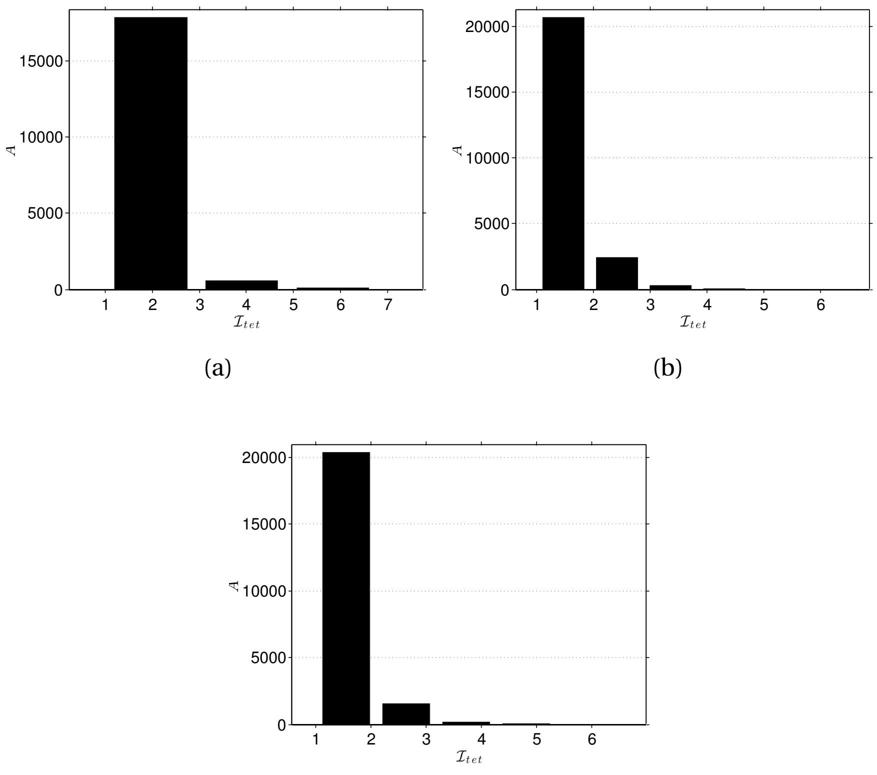

(a)

(b)

(c)

Figure 86: Histograms - group MS: (a) $(MS, 1.0, 1.5)$; (b) $(MS, 1.5, 3.0)$; (c) $(MS, 2.0, 5.0)$.

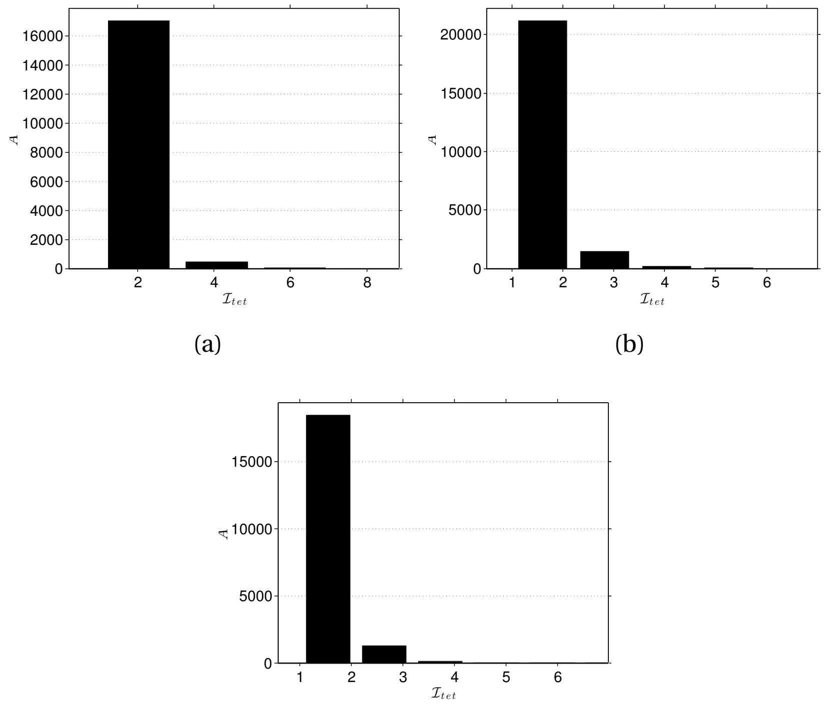

(a)

(b)

(c)

Figure 87: Histograms - group WL: (a) $(WL, 1.0, 1.5)$; (b) $(WL, 1.5, 3.0)$; (c) $(WL, 2.0, 5.0)$.

Test Configuration (Ref, λ, L_P)	Time Instant t_A	Number of Elements $A_{\mathscr{I}}^{max}$	Quality Percentage $\mathscr{O}_{\%}$
$(MS, 1.0, 1.5)$	1.03	17881	95.86
$(MS, 1.5, 3.0)$	8.50	20748	87.42
$(MS, 2.0, 5.0)$	25.47	20421	91.54
$(WL, 1.5, 1.5)$	8.17	17060	96.71
$(WL, 2.0, 3.0)$	9.68	21229	91.88
$(WL, 2.0, 5.0)$	13.22	18479	92.20

Table 9: Quality indicators relative to the statistical histograms $(\mathscr{I}_{tet}(t) \times A; 10)$.

CONCLUSION

This thesis studied the numerical modeling of a particular flow featured by the influence of a crossflow over drops that detach off a continuous jet taking into account a periodic approach. The basis for this research was inspired in the well-known canonical flow of a jet in crossflow, which was dealt with in a nonturbulent scope. Given the large amount of research concerned with strong jet-to-crossflow ratios as well as with vortical structures shedding through gas-liquid mixtures, this study took a different path when investigating weak crossflow ratios in liquid-liquid interfaces. Assumptions were established concerning the focus on the jet's primary breakup zone and the inclusion of periodic boundary conditions into the model. Nevertheless, the computational structure as well as the ideas behind the numerical algorithms demonstrated to be a promising tool in studying other two-phase flow regimes pictured by dispersed bubbles and drops.

In Chapter 2, we addressed the fundamental aspects of the ALE description, introduced a short review on numerical methods available to model two-phase flows, and discussed a few topics of the mechanics with interfaces, such as the jump of properties near an interface and the existence of surface tension. Finally, we established a mathematical description of the meshing structures applied in the computational code used in this thesis to provide organization of the content and resources for better theoretical outlines.

Basic principles used in CFD, governing equations, and the one-fluid formulation were introduced in Chapter 3, by emphasizing the inclusion of the volumetric representation of the surface tension force into the momentum equation and how a marker function is implemented to identify the different fluids or phases making up the flow. Additionally, selected information about the semi-lagrangian method and the projection method were given.

Chapter 4 along with Chapter 5 provided the detailed description of the FE formulation applied to two-phase flows as used in this thesis, by integrating the variational approach to include periodic boundary conditions into this set. Moreover, they explained the peculiarities of the operational tools that make up this methodology, subsequently applied to validation tests in Chapter 6 that certified the implementations.

The drop jet in crossflow investigated with details in Chapter 7, starting from the configuration of a very particular testing setup for studying different fluid-fluid cases. A technique based on a moving-frame reference were extended to deal with transverse flows. Despite of using only two fluid pairs of known experimental applicability, several data could be extracted from combinations of parameters defining the jet-to-crossflow ratio and the periodic cell's length, such as analyses of hydrodynamics, drop shape, spectrum and mesh quality so promoting a handful of computational and statistical information fairly complete as regarding the intended goals of this thesis.

Generally, the ALE/FE methodology employed here gathers many advantages since it provides a generalized form to control the mesh motion, besides aggregating functions that enable versatile dynamic meshing operations, such as node addition, node deletion, mesh smoothing and refinement, which ensure a sophisticated level of adaptivity for different flow behaviours. To enforce the usability of the tools developed with this work, analyses of two-fluid configurations under experimental conditions were performed. Qualitative comparisons about the hydrodynamics of bubble and drops immersed in fluids commonly mentioned in literature as well as some contributions about shape factors and energy spectra were presented.

By considering the overall set of technicalities employed in this thesis, a not exhaustive list of issues can be arranged, of which specific problems may derive. Some directions for future work are the following.

- Development of high-order methods: as issues relating to numerical accuracy, not only the interpolation through the semi-lagrangian method needs an upgrade from its linear capability, but also the projection method applied, which requires better accuracy.

- Algorithm improvement for PBC: although the matrix operations required to enforce the PBC over rows and columns follow a computational approach known as CSR *(Compressed Sparse Row)*, which stores only the nonzero entries of the matrices in order to escape memory allocation due to the sparsity, this methodology lacks of improvement for column operations. The strategy was implemented for square matrices and well applied for symmetric matrices while taking advantage of the symmetry to produce more compact loops. Nonsquare matrices, however, are not optimized as to column loops. Furthermore, the computation time for PBC operations also require additional observation.

- Selection of boundary conditions: the methodology presented here combines PBC, DBC, and NBC set by selection of boundary physical groups tagged at the pre-processing level. While the posing of the problems are well defined in regard to the mathematical point of view, their numerical resolution might be intricate when defining consistent boundary conditions. Running tests showed that the choice among pairs solver-preconditioner may render dependent on the problem. Intersection points, viz. corner points, which share different boundaries worth careful attention and better strategies to select priorities should be achieved.

- Multidimensional periodicity: in this thesis, the periodicity was applied only in one direction. Although this capability enables the simulation of several flows of practical interest, other situations in which multidimensional periodicity occurs need to be covered. The alternative way is to extend the mesh generation for more complex surfaces, obtained by translation or rotation, for instance, and suit the computational code to receive such extra functionality.

- Handling of topological changes: the modelling of physical phenomena associated to the topological changes of dispersed bodies in two-phase configurations, such as acute deformations, breakup and coalescence is not completely solved in the current code. Besides requiring the reordering of the data structures responsible to save the mesh data, such a capability should be assessed so that the physical interactions among the dispersed bodies are respected. Flows whose hydrodynamic effects are complex (e.g. approaching velocity, film thinning and rupture in bubble coalescence) represent a path to be unveiled.

- Coupling of physical mechanisms: diabatic flows inside the scope of heat and mass transfer dynamics together with multidimensional periodicity are a goal to be achieved, since modern applications encompassing two-phase flow regimes, such as bubbly and slug flows, have a big quota of interest in thermo-mechanical applications where ubiquitous temperature variations and heat transfer processes reign.

- Parallel computing: advancing toward data parallelism as well as evaluating the performance of the numerical code across a multi-core stage represents another potential learning curve regarding the current code.

- Curvature and capillary pressure modelling: the curvature computation follows a geometrical idea which is based on the Frenet's relations. Although the results obtained until now are satisfactory for a class of dispersed flows, namely bubbles and drops, other flow regimes, such as annular and jet flows require additional attention because of their prolonged interfaces. Since they may have instabilities, localized high-curvature zones may be generated by peaked nodes that cause unavoidable bad-shaped elements. Therefore, new alternatives for interpolation and capture of numerically uncontrollable curvatures should be developed. Additionally, advancements in the coupling with PBC are necessary as regards the computation of curvature over the periodic faces over which interface points overlap.

- Marangoni effects: flows subject to Marangoni effects generated by surface tension gradients due to the influence of either contaminants or surfactants as well as reactive flows represent another field of study opened to the numerical code used in this thesis.

- Multifluid interaction: all cases dealt with here take a two-fluid/two-phase flow condition. Although the interaction of too many dispersed elements can be studied in these conditions, the codification required to include three or more substances should be implemented. Surely, this further step will open up several opportunities of study.

- Extensions for the drop jet configuration: the inclusion of gravity is an incremental effect to be considered in the future. Another point to be considered sticks to the imposition of the initial condition of the jet. It is known that disturbances emerge from a drop that detaches off a unbroken liquid jet, which may propagate with the drop's motion. Therefore, the survey on an initial condition that considers such a effects is deserves additional study. Concerning the periodic spacing of drops, a condition similar to a "multipole flow" formed by sources and sinks interposed in-line may help to resolve the flow in the gaps between trailing and leading drops whilst also resorts to a disturbed flow around the drops.

To conclude, it should be emphasized that has been arising not only many variants of the classical FEM along the recent decades, but also many opportunities for newer applications. Incompressible two-phase flows, strictly, represent an important portion of this whole and so will be the ongoing tools intended to develop FEM codes. ALE/FEM methods have gained immeasurable proportions in fluid-structure interaction problems, from which other front-end creative solutions may appear and be adapted for different situations. Moreover, with the ascension of FE-based commercial codes, the state-of-art in developing scientific MCFD codes with robust and uncomplicated programming languages in this field will may be able to become a prosper research line.

APPENDIX A - Code Flowcharts

This appendix gathers overview flowcharts of the FE-based in-house code used in this thesis concerning the three basic macro stages of any software turned to Computational Fluid Dynamics as well as a very simple UML partial diagram of the main C++ classes involved in the PBC programming.

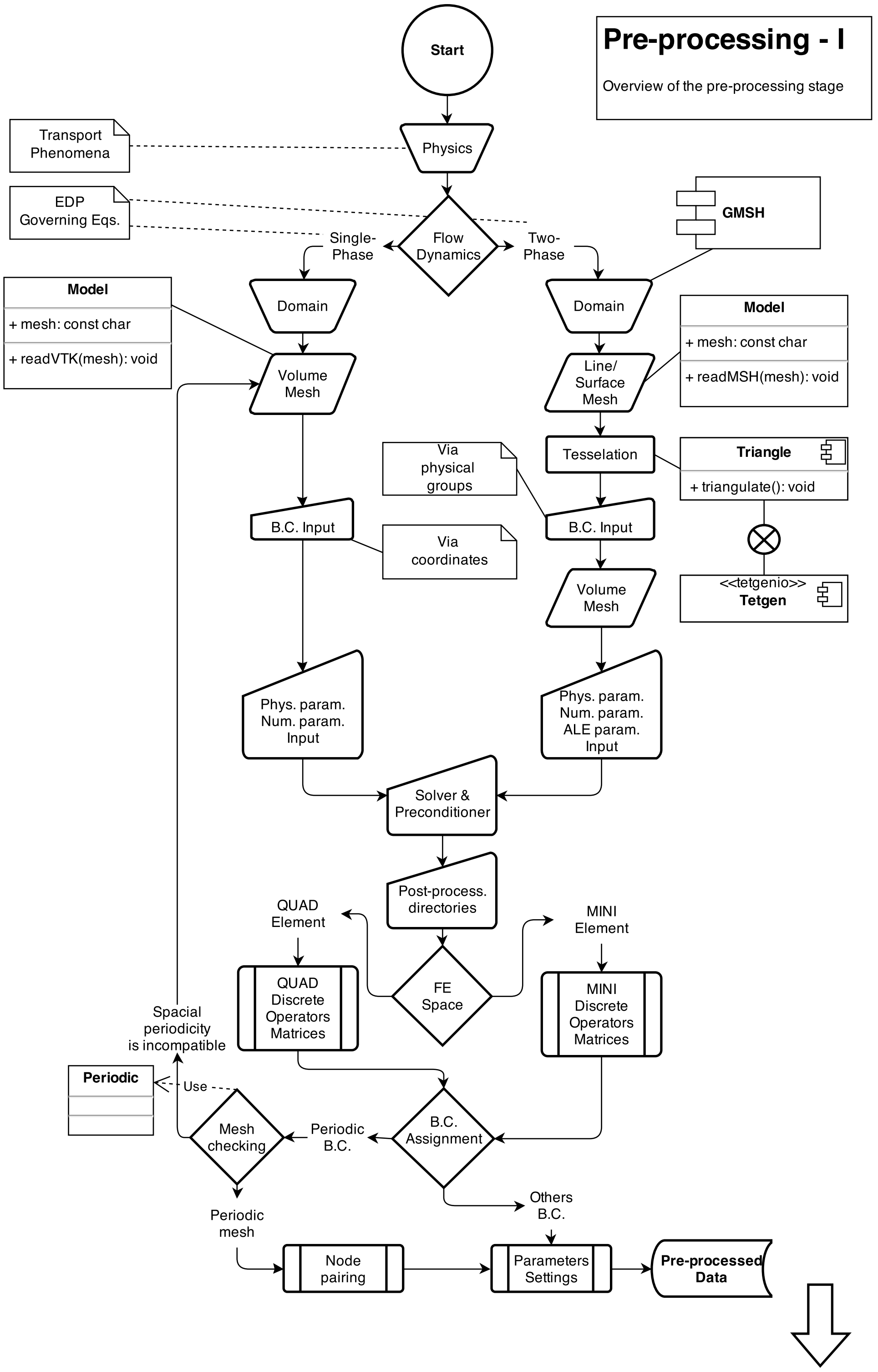

Figure 88: Flowchart I: pre-processing stage.

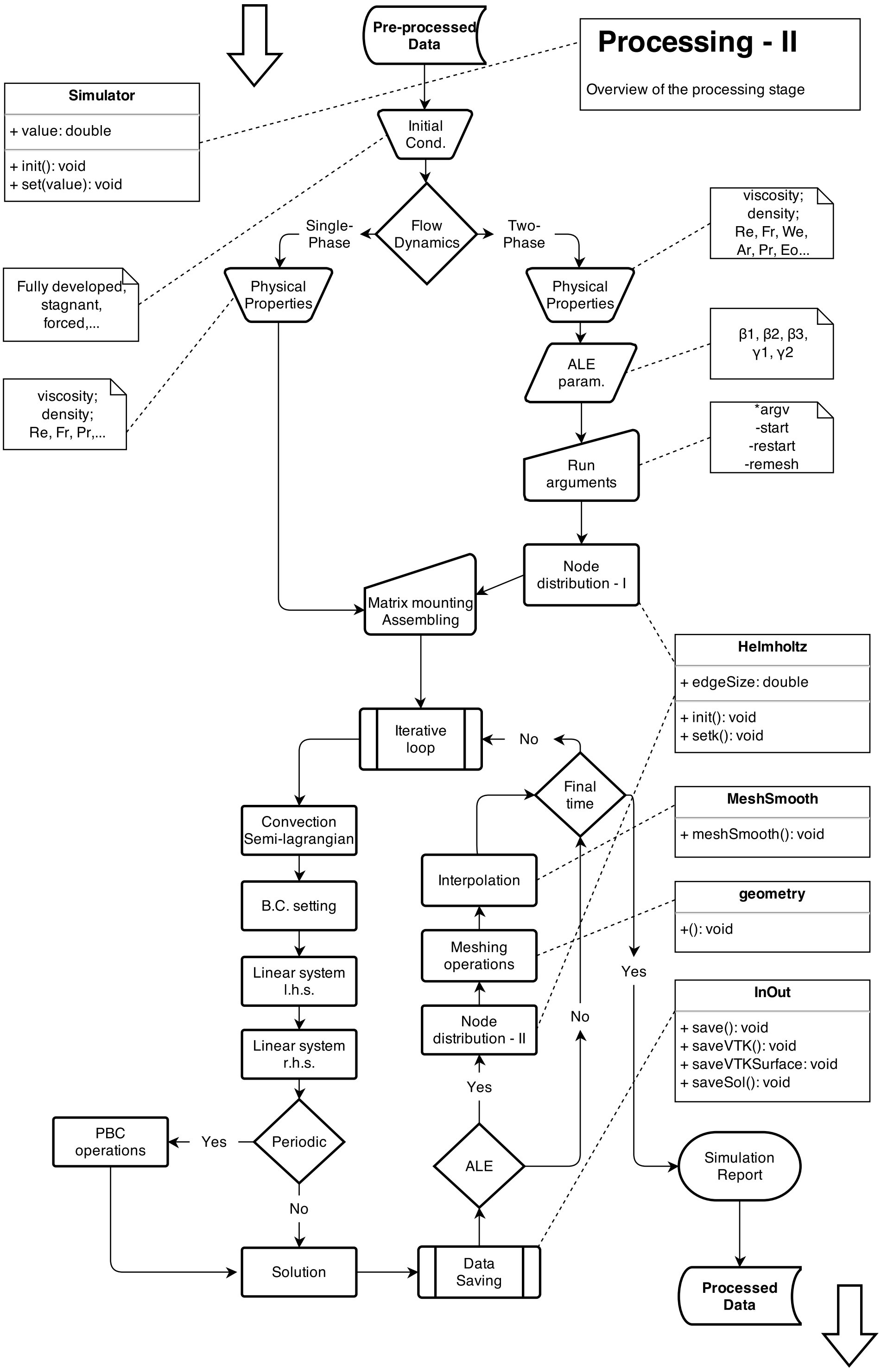

Figure 89: Flowchart II: processing stage.

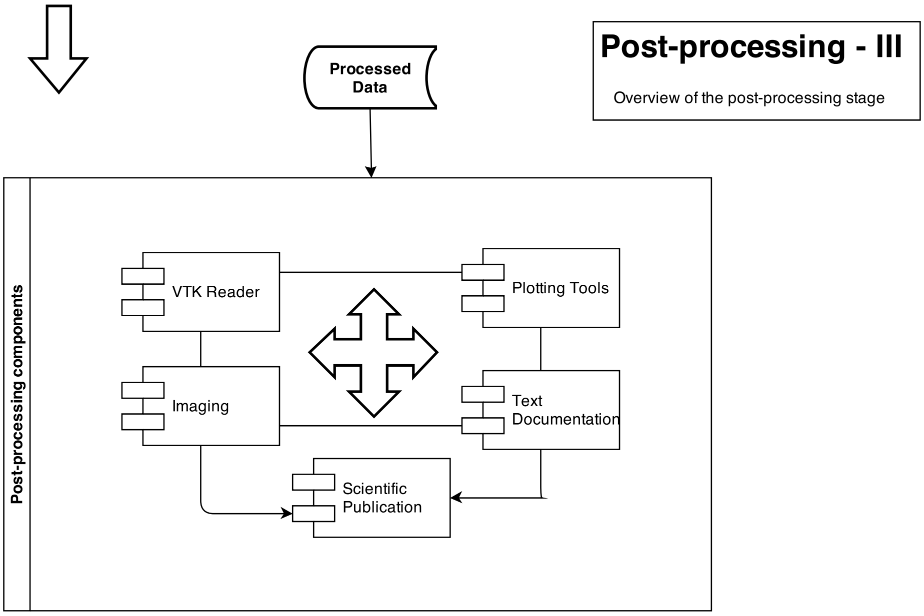

Figure 90: Flowchart III: post-processing stage.

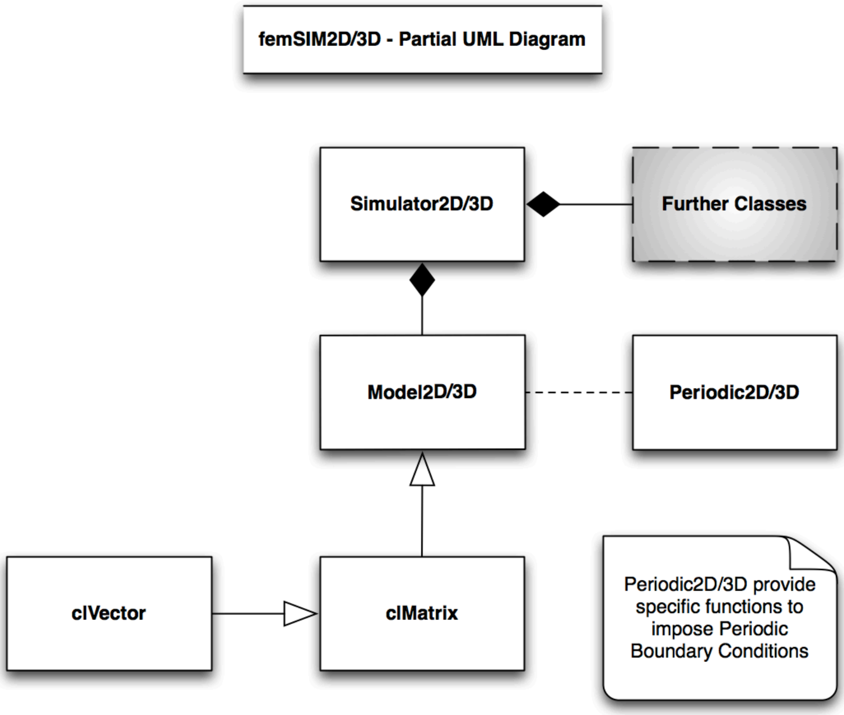

Figure 91: UML partial diagram of the in-house femSIM2D/3D code.

APPENDIX B - GMSH SCRIPT SAMPLE (PERIODIC SURFACE)

```
/* File: sample-periodic-surface-thesis.geo
 * Author: Peixoto de Oliveira, Gustavo
 * Date: December 31st, 2013
 * Description: Generates a 3D channel with periodicity
 *     and array of nb equally-spaced spheres.
 */

// Characteristic Lengths
b = 0.08; // bubbles
wp = 0.2;  // walls

// Boundary Geometry
xMin = 0;
yMin = 0;
zMin = 0;

r1 = 1;   // radius
D = 2*r1; // diameter

// Bubble Parameters
DB = 1;    // bubble diameter
rb = DB/2; // bubble radius

g = rb;  // gap length
s = 2*g; // slug length

nb = 3; // number of bubbles
LM = nb*DB + (nb - 1)*s; // bubble array
L = LM + 2*g; // channel length

// 1. PERIODIC SURFACES

// left end
p1 = newp;
Point(p1) = {xMin,yMin,zMin,wp}; // center
p2 = newp;
Point(p2) = {xMin,yMin,zMin - r1,wp};
p3 = newp;
Point(p3) = {xMin,yMin + r1,zMin,wp};
p4 = newp;
Point(p4) = {xMin,yMin,zMin + r1,wp};
p5 = newp;
Point(p5) = {xMin,yMin - r1,zMin,wp};

// right end
p6 = newp;
Point(p6) = {xMin + L,yMin,zMin,wp}; // center
p7 = newp;
```

```
Point(p7) = {xMin + L,yMin,zMin - r1,wp};
p8 = newp;
Point(p8) = {xMin + L,yMin + r1,zMin,wp};
p9 = newp;
Point(p9) = {xMin + L,yMin,zMin + r1,wp};
p10 = newp;
Point(p10) = {xMin + L,yMin - r1,zMin,wp};

/* --- BUILDING CIRCLES --- */
// left end
c1 = newc;
Circle(c1) = {p2,p1,p3};
c2 = newc;
Circle(c2) = {p3,p1,p4};
c3 = newc;
Circle(c3) = {p4,p1,p5};
c4 = newc;
Circle(c4) = {p5,p1,p2};

// right end
c5 = newc;
Circle(c5) = {p7,p6,p8};
c6 = newc;
Circle(c6) = {p8,p6,p9};
c7 = newc;
Circle(c7) = {p9,p6,p10};
c8 = newc;
Circle(c8) = {p10,p6,p7};

/* --- BUILDING EXTERNAL LINES --- */
l1 = newl;
Line(l1) = {p2,p7};
l2 = newl;
Line(l2) = {p3,p8};
l3 = newl;
Line(l3) = {p4,p9};
l4 = newl;
Line(l4) = {p5,p10};

// 2. INTERNAL DOMAIN - BUBBLES

// Origin
x0 = xMin;
y0 = yMin;
z0 = zMin;

For i In {1:nb} // BEGIN LOOP

// --- spherical bubble points
```

```
pp9 = newp;
Point(pp9) = {x0 + g + rb + (i - 1)*(DB + s), y0, z0, b};
pp10 = newp;
Point(pp10) = {x0 + g + rb + (i - 1)*(DB + s), y0, z0 - rb, b};
pp11 = newp;
Point(pp11) = {x0 + g + rb + (i - 1)*(DB + s), y0 + rb, z0, b};
pp12 = newp;
Point(pp12) = {x0 + g + rb + (i - 1)*(DB + s), y0, z0 + rb, b};
pp13 = newp;
Point(pp13) = {x0 + g + rb + (i - 1)*(DB + s), y0 - rb, z0, b};
pp14 = newp;
Point(pp14) = {x0 + g + (i - 1)*(DB + s), y0, z0, b};
pp15 = newp;
Point(pp15) = {x0 + g + DB + (i - 1)*(DB + s), y0, z0, b};

// --- BUILDING CIRCLES ---

// x-normal meridian
cc11 = newc;
Circle(cc11) = {pp12,pp9,pp11};
cc12 = newc;
Circle(cc12) = {pp11,pp9,pp10};
cc13 = newc;
Circle(cc13) = {pp10,pp9,pp13};
cc14 = newc;
Circle(cc14) = {pp13,pp9,pp12};

// z-normal meridian
cc15 = newc;
Circle(cc15) = {pp11,pp9,pp14};
cc16 = newc;
Circle(cc16) = {pp14,pp9,pp13};
cc17 = newc;
Circle(cc17) = {pp13,pp9,pp15};
cc18 = newc;
Circle(cc18) = {pp15,pp9,pp11};

// --- DISCRETIZATION (THETA) CIRCLES ---
nt2 = 14; // number of theta points per quarter of circle (total around circle is 4*nt)
//Transfinite Line{cc11,cc12,cc13,cc14,cc15,cc16,cc17,cc18} = nt2 Using Bump 1;

// BUBBLES' SURFACES
// reference: central axis is X-positive and theta counterclockwise

// 0:Pi/2
lb21 = newl;
Line Loop(lb21) = {cc12,cc13,-cc16,-cc15};
sb21 = news;
```

```
Ruled Surface(sb21) = {lb21};

// Pi/2:Pi
lb22 = newl;
Line Loop(lb22) = {-cc18,-cc17,-cc13,-cc12};
sb22 = news;
Ruled Surface(sb22) = {lb22};

// Pi:3*Pi/2
lb23 = newl;
Line Loop(lb23) = {-cc11,-cc14,cc17,cc18};
sb23 = news;
Ruled Surface(sb23) = {lb23};

// 3*Pi/2:2*Pi
lb24 = newl;
Line Loop(lb24) = {cc15,cc16,cc14,cc11};
sb24 = news;
Ruled Surface(sb24) = {lb24};

Printf("Generating dispersed body %g...",i);
Printf("Data bubble: %g",i);
Printf("Bubble's ruled surface - 0:Pi/2 = %g",sb21);
Printf("Bubble's ruled surface - Pi/2:Pi = %g",sb22);
Printf("Bubble's ruled surface - Pi:1.5*Pi = %g",sb23);
Printf("Bubble's ruled surface - 1.5*Pi:2*Pi = %g",sb24);

// DISPERSED PHYSICAL SURFACES
Physical Surface(Sprintf("Dispersed%g",i)) = {sb21,sb22,sb23,sb24};

EndFor

// 4. BUILDING EXTERNAL SURFACES

// left end
ll15 = newl;
Line Loop(ll15) = {-c4,-c3,-c2,-c1};
s1 = news;
Plane Surface(s1) = {ll15};

// right end
ll16 = newl;
Line Loop(ll16) = {c5,c6,c7,c8};
s2 = news;
Plane Surface(s2) = {ll16};

// channel's surfaces

ll17 = newl;
```

```
Line Loop(ll17) = {-l1,c1,l2,-c5};
s3 = news;
Ruled Surface(s3) = {ll17};

ll18 = newl;
Line Loop(ll18) = {-l2,c2,l3,-c6};
s4 = news;
Ruled Surface(s4) = {ll18};

ll19 = newl;
Line Loop(ll19) = {-l3,c3,l4,-c7};
s5 = news;
Ruled Surface(s5) = {ll19};

ll20 = newl;
Line Loop(ll20) = {-l4,c4,l1,-c8};
s6 = news;
Ruled Surface(s6) = {ll20};

// --- PERIODIC SURFACES MESHING s1 - Master :: s2 - Slave

Periodic Surface s1 {c1,c2,c3,c4} = s2 {c5,c6,c7,c8};

// 5. BOUNDARY PHYSICAL SURFACES

Physical Surface("PeriodicLeftBoundary") = {s1};
Physical Surface("PeriodicRightBoundary") = {s2};
Physical Surface("NoSlipBoundary") = {s3,s4,s5,s6};

/* End of script */
```

APPENDIX C - EQUATIONS OF THE PBC FORMULATION

Enforcement of PBC: mathematical aspects

Let

$$\begin{aligned}\int_\Omega \rho \left[\frac{\partial \mathbf{v}_P}{\partial t} + (\mathbf{v}_P - \hat{\mathbf{v}}) \cdot \nabla \mathbf{v}_P\right] \cdot \mathbf{w}_P \, d\Omega - Eu_\beta \int_\Omega \mathbf{e}_P \cdot \mathbf{w}_P \, d\Omega + \int_\Omega \nabla \tilde{p} \cdot \mathbf{w}_P \, d\Omega \\ -\frac{1}{Re} \int_\Omega \nabla \cdot \left[\mu \left(\nabla \mathbf{v}_P + \nabla \mathbf{v}_P{}^T\right)\right] \cdot \mathbf{w}_P \, d\Omega - \frac{1}{Fr^2} \int_\Omega \rho \mathbf{g} \cdot \mathbf{w}_P \, d\Omega \\ -\frac{1}{We} \int_\Omega \mathbf{f} \cdot \mathbf{w}_P \, d\Omega = \mathbf{0}, \quad \mathbf{v}_P, \mathbf{w}_P \in \mathcal{V}_P\end{aligned}$$

be the expanded form of

$$\int_\Omega \mathsf{B}_{1,P}(\mathbf{v}_P, \tilde{p}, \mathbf{f}; \hat{\mathbf{v}}, \rho, \mu, \mathbf{g}) \cdot \mathbf{w}_P \, d\Omega = 0,$$

which is included in Equation (5.17). By using integration by parts in the viscous term and periodic pressure term,

$$\begin{aligned}\int_\Omega \nabla \cdot \left[\mu \left(\nabla \mathbf{v}_P + \nabla \mathbf{v}_P{}^T\right)\right] \cdot \mathbf{w}_P \, d\Omega = -\int_\Omega \mu \left[\left(\nabla \mathbf{v}_P + \nabla \mathbf{v}_P{}^T\right) : \nabla \mathbf{w}_P^T\right] d\Omega + \\ + \int_\Gamma \mathbf{n} \cdot \left[\mu \left(\nabla \mathbf{v}_P + \nabla \mathbf{v}_P{}^T\right) \cdot \mathbf{w}_P\right] d\Gamma \\ \int_\Omega \nabla \tilde{p} \cdot \mathbf{w}_P \, d\Omega = -\int_\Omega \tilde{p} \nabla \cdot \mathbf{w}_P \, d\Omega + \int_\Gamma \tilde{p} \mathbf{w}_P \cdot \mathbf{n} \, d\Gamma.\end{aligned}$$

Now, since $\Gamma = \Gamma_P \cup \Gamma_D$, the Γ-integrals can be decomposed into

$$\begin{aligned}\int_\Gamma \mathbf{n} \cdot \left[\mu \left(\nabla \mathbf{v}_P + \nabla \mathbf{v}_P{}^T\right) \cdot \mathbf{w}_P\right] d\Gamma = \int_{\Gamma_D} \mathbf{n} \cdot \left[\mu \left(\nabla \mathbf{v}_P + \nabla \mathbf{v}_P{}^T\right) \cdot \mathbf{w}_P\right] d\Gamma + \\ + \int_{\Gamma_P} \mathbf{n} \cdot \left[\mu \left(\nabla \mathbf{v}_P + \nabla \mathbf{v}_P{}^T\right) \cdot \mathbf{w}_P\right] d\Gamma \\ \int_\Gamma \tilde{p} \mathbf{w}_P \cdot \mathbf{n} \, d\Gamma = \int_{\Gamma_D} \tilde{p} \mathbf{w}_P \cdot \mathbf{n} \, d\Gamma + \int_{\Gamma_P} \tilde{p} \mathbf{w}_P \cdot \mathbf{n} \, d\Gamma.\end{aligned}$$

However, given that

$$\mathbf{w}_P|_{\Gamma_D} = \mathbf{0},$$

the integrals relate to the Dirichlet boundary vanish, thus remaining

$$\int_{\Gamma} \mathbf{n} \cdot \left[\mu\left(\nabla \mathbf{v}_P + \nabla \mathbf{v}_P{}^T\right) \cdot \mathbf{w}_P\right] \, d\Gamma = \int_{\Gamma_P} \mathbf{n} \cdot \left[\mu\left(\nabla \mathbf{v}_P + \nabla \mathbf{v}_P{}^T\right) \cdot \mathbf{w}_P\right] \, d\Gamma$$

$$\int_{\Gamma} \tilde{p} \mathbf{w}_P \cdot \mathbf{n} \, d\Gamma = \int_{\Gamma_P} \tilde{p} \mathbf{w}_P \cdot \mathbf{n} \, d\Gamma.$$

The periodic boundary, in turn, is decomposed by $\Gamma_P = \Gamma_L \cup \Gamma_R$, where $\Gamma_R = \Gamma_L \oplus L_P \mathbf{e}_P$ to give

$$\int_{\Gamma_P} \mathbf{n} \cdot \left[\mu\left(\nabla \mathbf{v}_P + \nabla \mathbf{v}_P{}^T\right) \cdot \mathbf{w}_P\right] \, d\Gamma = \int_{\Gamma_L} \mathbf{n} \cdot \left[\mu\left(\nabla \mathbf{v}_P + \nabla \mathbf{v}_P{}^T\right) \cdot \mathbf{w}_P\right] \, d\Gamma + \\ + \int_{\Gamma_R} \mathbf{n} \cdot \left[\mu\left(\nabla \mathbf{v}_P + \nabla \mathbf{v}_P{}^T\right) \cdot \mathbf{w}_P\right] \, d\Gamma$$

$$\int_{\Gamma_P} \tilde{p} \mathbf{w}_P \cdot \mathbf{n} \, d\Gamma = \int_{\Gamma_L} \tilde{p} \mathbf{w}_P \cdot \mathbf{n} \, d\Gamma + \int_{\Gamma_R} \tilde{p} \mathbf{w}_P \cdot \mathbf{n} \, d\Gamma.$$

Now, the enforcement of the PBC require that

$$\begin{aligned} \mathbf{v}|_{\Gamma_L} &= \mathbf{v}|_{\Gamma_R} \\ \mathbf{n} \cdot \nabla \mathbf{v}|_{\Gamma_L} &= -\mathbf{n} \cdot \nabla \mathbf{v}|_{\Gamma_R} \\ \tilde{p}|_{\Gamma_L} &= \tilde{p}|_{\Gamma_R} \\ \mathbf{n} \cdot \nabla \tilde{p}|_{\Gamma_L} &= -\mathbf{n} \cdot \nabla \tilde{p}|_{\Gamma_R}, \end{aligned}$$

so that

$$\int_{\Gamma_L} \mathbf{n} \cdot \left[\mu\left(\nabla \mathbf{v}_P + \nabla \mathbf{v}_P{}^T\right) \cdot \mathbf{w}_P\right] \, d\Gamma + \int_{\Gamma_R} (-\mathbf{n}) \cdot \left[\mu\left(\nabla \mathbf{v}_P + \nabla \mathbf{v}_P{}^T\right) \cdot \mathbf{w}_P\right] \, d\Gamma$$

$$\int_{\Gamma_L} \tilde{p} \mathbf{w}_P \cdot \mathbf{n} \, d\Gamma + \int_{\Gamma_R} \tilde{p} \mathbf{w}_P \cdot (-\mathbf{n}) \, d\Gamma.$$

cancel out in the formulation because of the opposite sign of the normal vector over Γ_R. Finally, the periodic mesh nodes in the discrete equations are manipulated via rows/columns operations.

APPENDIX E - CURVATURE AND FRENET'S FRAME

Curvature

Curvature is a scalar function $\kappa(s)$ that associates a real number to each point of a parametrized curve in s by a real interval like $a \leq s \leq b$. From the Differential Geometry [**?**], one ascertains that the curvature measures "how much the curve is bending at the parametrized point". This quantity is well understood by comparing it to the role played by a derivative of the velocity vector at a point of a trajectory. However, the concept of curvature extends to smooth surfaces where it turns into a much more intricate matter. For a general surface ζ, $\kappa(s)$ should satisfy some properties. The most intuitive are:

- k is a smooth map;
- a point with an open neighbourhood contained in a plane has zero curvature;
- if $\mathbf{p}, \mathbf{q} \in \zeta$ are points such that $\mathbf{p}$ has a neighbourhood that forms a sharp peak higher than a neighbourhood of $\mathbf{q}$, then $\kappa(\mathbf{p}) > \kappa(\mathbf{q})$.

Frenet Frame

When we consider a curve in $\mathbb{R}^3$ parameterized in s by a real interval like $a \leq s \leq b$, three vectors are essential to give information about the curve, namely, the normal vector $\mathbf{n}(s)$, the tangent vector $\mathbf{t}(s)$ and the *binormal vector* $\mathbf{b}(s)$. This latter vector only makes sense in $\mathbb{R}^3$, since is defined by

$$\mathbf{b} = \mathbf{t} \times \mathbf{n}. \tag{7.19}$$

$\{\mathbf{t}, \mathbf{n}, \mathbf{b}\}$ form an orthonormal basis to $\mathbb{R}^3$, which, indeed, is called the *Frenet frame.*

Calculation of curvature for one-dimensional interfaces

Another relevant characteristic of the method used here concerns to the computation of the curvature κ, which depends on geometrical operations performed over interface elements. With the insertion of the CSF model [**?**] to estimate the interfacial force that goes along with the Equation (3.39), an accurate retrieval of the curvature is needed. In order to spare painstaking reproductions of all the geometrical apparatus, we will refer to [**?**], [**?**] for further ascertainments.

The discrete process to calculate the unit normal vector in two-dimensional domains takes two properties into account. Firstly, the interface is a curve represented by a set of linear elements and structured. Secondly, the normal vectors for each neighbour element can be obtained by orthogonalizing the unit tangent vectors to each element, which, in fact, are obtained by normalizing the element length itself. In turn, the normal vector for the shared node is evaluated by summing the contributions of the normal elemental vectors. This scheme is depicted in Figure 92. Mathematically, if $\mathbf{n}(e_{L,i}), \mathbf{n}(e_{R,i})$ are the unit normal vectors evaluated over the neighbour elements respectively at left and at right of the interface node $\mathbf{x}_i$, then,

$$\mathbf{n}(e_{L,i}) = \mathbf{R}_{\pi/2}\left[\mathbf{t}(e_{L,i})\right], \quad \mathbf{n}(e_{R,i}) = \mathbf{R}_{\pi/2}\left[\mathbf{t}(e_{R,i})\right], \tag{7.20}$$

where

$$\mathbf{t}(e_{L,i}) = \frac{\mathbf{x}_{L,i} - \mathbf{x}_i}{||\mathbf{x}_{L,i} - \mathbf{x}_i||}, \quad \mathbf{t}(e_{R,i}) = \frac{\mathbf{x}_{R,i} - \mathbf{x}_i}{||\mathbf{x}_{R,i} - \mathbf{x}_i||}. \tag{7.21}$$

Above, $\mathbf{x}_{L,i}, \mathbf{x}_{R,i}$ are the vertices of the neighbour elements not matching the interface node and $\mathbf{t}(e_{L,i}), \mathbf{t}(e_{R,i})$ their respective unit tangent vectors generated by the rotation matrix $\mathbf{R}_{\pi/2}$. Directly from Equations (7.20) and (7.21), one gets

$$\mathbf{n}(\mathbf{x}_i) = \mathbf{n}(e_{L,i}) + \mathbf{n}(e_{R,i}) = \mathbf{R}_{\pi/2}\left[\mathbf{t}(e_{L,i}) + \mathbf{t}(e_{R,i})\right]. \tag{7.22}$$

Meanwhile, the curvature $\kappa(\mathbf{x}_i)$ is evaluated for each interface node by an approximation adapted from a formulae set of the Frenet's frame, or, even more formally, *Frenet-Serret Theorem* - see [**?**] - for curvature and torsion. 7.23 is the continuous version of one among the Frenet's formulae relating κ and the unit vector tangent $\mathbf{t}$ to the interface.

$$\kappa\mathbf{n} = \frac{\partial \mathbf{t}}{\partial s} \approx \frac{\mathbf{t}(e_{L,i}) - \mathbf{t}(e_{R,i})}{\bar{h}}. \tag{7.23}$$

Since the elements $e_{L,i}, e_{R,i}$ do not necessarily have the same size, the evaluation of $\kappa(\mathbf{x}_i)$ is undertaken as an average distribution over the mean length $\bar{h}$ of the neighbour elements

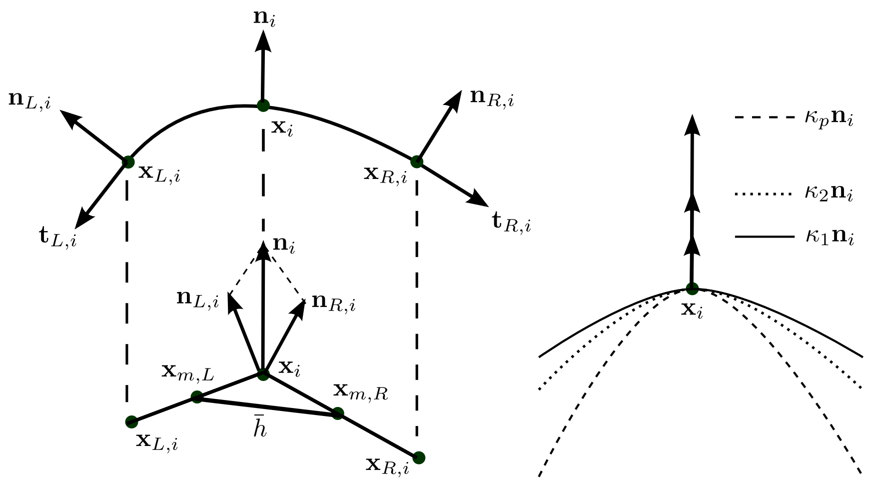

(a) (b)

Figure 92: Scheme for the calculation of the curvature: (a) continuous and discrete versions; (b) effect of the curvature upon the normal vector at $\mathbf{x}_i$.

given by

$$\bar{h} = \frac{1}{2}(h_L + h_R), \tag{7.24}$$

where h_L, h_R are the lengths of the neighbour elements. Also depicted in Figure 92 at left, it is seen that $\bar{h}$ binds the two midpoints $\mathbf{x}_{m,L}, \mathbf{x}_{m,R}$. At right, a sketch was added only to illustrate how κ affects the normal vector $\mathbf{n}_i$ by stretching it. From Equation (7.23), it is inferred that the higher the tangential derivative along the interface, the higher the norm of the vector $\kappa \mathbf{n}_i$, because if, for instance, we choose a sequence (κ_p) such that $\kappa_1 < \kappa_2 < \ldots < \kappa_p$, then

$$||\kappa_1 \mathbf{n}_i|| < ||\kappa_2 \mathbf{n}_i|| < \ldots < ||\kappa_p \mathbf{n}_i||. \tag{7.25}$$

In other words, high curvatures tend to magnify the normal vector at $\mathbf{x}_i$.

APPENDIX E - VERIFICATION & VALIDATION

The following text contains clippings about the meaning of verification and validation in terms of the CFD's vogue. Such terminologies, sometimes used interchangeably, are discussed here in order to elucidate presumable ambiguities. For a long and detailed review about the topic, refer to [**?**] and references therein.

The concept of V&V

Definition 7.5.1 (Verification) *The process of determining that a model implementation accurately represents the developer's conceptual description of the model and the solution to the model.*

Definition 7.5.2 (Validation) *The process of determining the degree to which a model is an accurate representation of the real world from the perspective of the intended uses of the model.*

Verification provides evidence, or substantiation, that the mathematical model, which is derived from the conceptual model, is solved correctly by the computer code that is being assessed. Verification does not address the issue of whether the mathematical model - defined by a set of partial differential or integro-differential equations along with the required initial and boundary conditions - has any relationship to the real world, e.g., physics. Validation, on the other hand, provides evidence, or substantiation, of how accurately the computational model simulates the real world for system responses of interest. Validation activities presume that the computational model result is an accurate solution of the mathematical model.

Code verification procedures

Considering the numerical solution of PDEs, code verification comprises the activities of:

1. defining appropriate benchmarks for the evaluation of solution accuracy and
2. determining what constitutes satisfactory performance of the algorithms on the benchmarks.

Code verification relies on the comparison of computational solutions to the "correct answer". The correct answer is provided by highly accurate solutions for a set of well-chosen

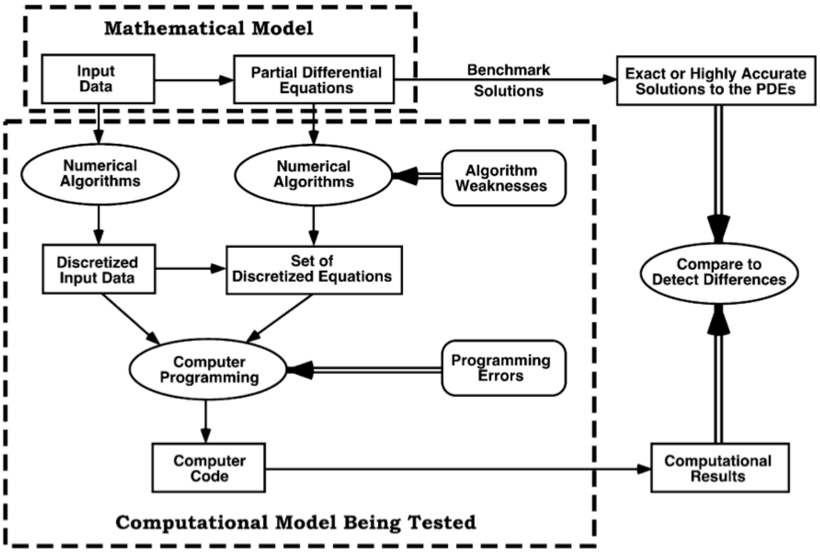

Figure 93: Example of a process of verification to detect errors in codes. Extracted from [**?**].

benchmarks, and this answer can only be known in a relatively small number of isolated cases. These cases therefore assume a very important role in code verification and should be carefully formalized in test plans that describe how the code will be verified. In code verification, the key feature to determine is the observed, or demonstrated, order of convergence using multiple numerical solutions. An exampled of method that uses exact or highly accurate solutions to the PDEs to detect numerical algorithm deficiencies and programming errors is illustrated in Figure 93.

The mathematical model is the general model for the application of interest, whereas the exact and highly accurate solutions to the PDEs are special-case solutions of the mathematical model. For these special cases, benchmark solutions can be computed. Four types of highly accurate solutions (from highest to lowest) are recognized:

1. manufactured solutions;

2. analytical solutions;

3. highly accurate numerical solutions to the ODEs and

4. highly accurate numerical solutions to the PDEs.

More specifically, analytical solutions are closed-form solutions to special cases of the PDEs defined in the mathematical model, commonly represented by infinite series, complex integrals, and asymptotic expansions. However, the most significant practical shortcoming of classical analytical solutions is that they exist only for very simplified physics, material properties, and geometries. Therefore, it is indispensable to use the same modelling assumptions for both the benchmark solution and the code being tested.

APPENDIX F - VITA

Gustavo Charles Peixoto de Oliveira was born March 31st, 1987 in Barra do Piraí, Rio de Janeiro, Brazil. He received his Licentiate degree in Mathematics from Federal Fluminense University/CECIERJ in 2008. Decided to pursuit an academic career more inclined to applied contexts, moved to the Engineering's atrium, whereby received his M.Sc. degree in Metallurgy and Materials Engineering from Federal University of Rio de Janeiro in 2011 with a two-years grant provided by the governmental Brazilian funding agency CNPq. Meanwhile, he began to work with CFD tools to investigate the hydrodynamic stability of rotating flows occurring in electrochemical cells. He started his Ph.D. trail still in 2011, was a one-year internship Ph.D. visitor at Ecole Polytechnique Fédérale de Lausanne, Switzerland, during 2013, specifically at LTCM - Laboratoire de Transfert de Chaleur et de Masse, supported by the Science Without Borders Program (CNPq/Brazil). There, he worked with gas-liquid two-phase flow dynamics. Back to Brazil, he received the degree of D.Sc. in Mechanical Engineering in 2015 from State University of Rio de Janeiro, also sponsored by the Brazilian agency CAPES with a four-years integral scholarship.

APPENDIX G - PUBLICATIONS

- ⋆ OLIVEIRA, G. P., ANJOS, G. R., PONTES, J., MANGIAVACCHI, N., THOME, J.R. *ALE/finite element modeling of an unconfined bubble plume in periodic domain: bubble shape and oscillation analysis*, accepted for publication in the Journal of the Brazilian Society of Mechanical Sciences and Engineering, 2015.

- ⋆ PONTES, J., MANGIAVACCHI, N., ANJOS, G. R., LUCENA, R., GAONA, C. M., OLIVEIRA, G. P., FERREIRA, D. *A Survey of Results Concerning Steady Solutions and the Stability of a Class of Rotating Flows.* Proceedings of the 3rd Conference of Computational interdisciplinary Sciences, Asunción, Paraguay, 2014.

- ⋆ OLIVEIRA, G.P., MANGIAVACCHI, N., ANJOS, G., PONTES, J., THOME, J.R. *Comparative CFD Simulations of Gas Transport in Slug Flow from Periodic Arrays with Single or Multiple Bubbles.* Proceedings of the 3rd Conference of Computational interdisciplinary Sciences, Asunción, Paraguay, 2014.

- ⋆ OLIVEIRA, G.C.P., ANJOS, G., PONTES, J., MANGIAVACCHI, N. *Finite Element Analysis of Pressure-Driven Laminar Flow Inside Periodically Staggered Arrays.* Proceedings of the VII Brazilian National Congress of Mechanical Engineering, Belém, Brazil, 2014.

- ⋆ OLIVEIRA, G.C.P., MANGIAVACCHI, N., ANJOS, G., THOME, J.R. *Numerical Simulation of a Periodic Array of Bubbles*, MecÃ¡nica Computacional, v. XXXII, 1813-1824, 2013.

- ⋆ OLIVEIRA, G.C.P., MANGIAVACCHI, N., ANJOS, G., THOME, J.R. *Topological Remeshing and Locally Supported Smoothing for Bubble Coalescence in Two-Phase Flows.* Proceedings of the 22nd International Congress of Mechanical Engineering, Ribeirão Preto, Brazil, 2013.

- ⋆ MORAES, E.L.S., OLIVEIRA, G.C.P., ANJOS, G., MANGIAVACCHI, N., PONTES, J. *Semi-Lagrangian Algorithms for Second Order for the Study of Hydrodynamics of Electrochemical Cells.* Proceedings of the 14th Brazilian Congress of Thermal Sciences and Engineering, Rio de Janeiro, Brazil, 2012.

- ⋆ OLIVEIRA, G.C.P., MANGIAVACCHI, N., PONTES, J. *Semi-Lagrangian High-Order 3D Interpolation: Survey on a Finite Element Z-Type Operator.* Proceedings of the 14th Brazilian Congress of Thermal Sciences and Engineering, Rio de Janeiro, Brazil, 2012.

- ⋆ OLIVEIRA, G.C.P., MANGIAVACCHI, N., PONTES, J. *High-Order Interpolation Applied to the Modeling of Advective Transport for Incompressible Flows.* Congress of Computational and Applied Mathematics- CMAC/NE, Natal, Brazil, 2012.
- ⋆ OLIVEIRA, G.C.P, *Hydrodynamic Stability in Electrochemical Cells Through the Finite Element Method*, M.Sc. dissertation, Federal University of Rio de Janeiro, Brazil, 2011.
- ⋆ OLIVEIRA, G.C.P., MANGIAVACCHI, N., PONTES, J. *A Semi-Lagrangian Scheme for Fluid Flow Simulations with a Zienkiewicz-Type Finite Element Interpolation.* Proceedings of the 21st International Congress of Mechanical Engineering, Natal, Brazil, 2011.